

2010

Renormalization and Damping of Dipole Exchange Spin Waves in Ultrathin Ferromagnetic Nanowires

Arash Akbari-Sharbaf

Follow this and additional works at: <https://ir.lib.uwo.ca/digitizedtheses>

Recommended Citation

Akbari-Sharbaf, Arash, "Renormalization and Damping of Dipole Exchange Spin Waves in Ultrathin Ferromagnetic Nanowires" (2010). *Digitized Theses*. 4847.
<https://ir.lib.uwo.ca/digitizedtheses/4847>

This Thesis is brought to you for free and open access by the Digitized Special Collections at Scholarship@Western. It has been accepted for inclusion in Digitized Theses by an authorized administrator of Scholarship@Western. For more information, please contact wlsadmin@uwo.ca.

Renormalization and Damping of Dipole-Exchange Spin Waves in Ultrathin Ferromagnetic Nanowires

(Spine title: Spin Waves in Ferromagnetic Nanowires)

(Thesis format: Monograph)

by

Arash Akbari-Sharbat

Graduate Program in Physics

A thesis submitted in partial fulfillment
of the requirements for the degree of
Master of Science

School of Graduate and Postdoctoral Studies
The University of Western Ontario
London, Ontario, Canada

© Arash Akbari-Sharbat 2010

THE UNIVERSITY OF WESTERN ONTARIO
SCHOOL OF GRADUATE AND POSTDOCTORAL STUDIES

CERTIFICATE OF EXAMINATION

Supervisor

Dr. M. G. Cottam

Supervisory Committee

Dr. Shantanu Basu

Dr. Mahi Singh

Examiners

Martin Houde

Heng-Yong Nie

Jayshri Sabarinathan

The thesis by

Arash Akbari-Sharbaf

entitled:

**Renormalization and Damping of Dipole-Exchange Spin Waves in
Ultrathin Ferromagnetic Nanowires**

is accepted in partial fulfillment of the
requirements for the degree of
Master of Science

Date _____

Pauline Barmby
Chair of the Thesis Examination Board

ABSTRACT

Motivated by recent experiments, a theoretical study of the nonlinear properties of the spin waves in ferromagnetic nanowires is presented. An ultrathin nanowire is represented by a single line of interacting spins placed in an oblique external applied magnetic field. A Hamiltonian-based approach is followed including terms for the short-range exchange interactions and the long-range magnetic dipole-dipole interactions. Using a perturbation theory based on a Green's function formalism and Feynman diagrammatic techniques, the roles of the three-magnon and four-magnon processes are studied. Detailed analytical expressions for the energy shift and damping for three-magnon process are deduced, along with an expression for the four-magnon energy shift in the special case of a longitudinal field. Numerical examples of the theory are made for the spin-wave renormalization effects for various external field orientations, taking parameters typical of a ferromagnetic metal. Some extensions of the theory to thicker nanowires are outlined.

Keywords: Spin waves (or magnons); nanowires; dipole-exchange modes; ferromagnets; nonlinear processes; diagrammatic perturbation theory.

ACKNOWLEDGEMENTS

It is impossible to overstate my gratitude to my Supervisor Michael Cottam. His enthusiasm, dedication, patience, and kind nature have made my experience as a graduate student memorable and enlightening. It is a remarkable privilege to have someone as knowledgeable and passionate as Michael willing to help unconditionally and full-heartedly with research, the process of writing this thesis and over all other academic matters. He has made a difficult endeavour smooth and as pleasant as possible.

My sincere thanks to the advisory committee members, Dr. Mahi Singh and Dr. Shantanu Basu for giving their valuable time and suggestions during the advisory committee meetings.

I'd like to give thanks to all members and secretarial staff in the Physics and Astronomy Department, University of Western Ontario.

I wish to extend thanks to my colleagues Tushar Das, Maher Ahmed, for their support, company and the great conversations and guidance they have provided me.

A very special thanks to my colleague Dr. Hoa Nguyen for her invaluable help revising this thesis.

I would also like to thank Dr. Raimundo Costa Filho for his guidance and support.

Finally, I would like to thank my wonderful family and friends for the constant encouragement and support during my graduate studies.

CONTENTS

CERTIFICATE OF EXAMINATION.....	ii
ABSTRACT.....	iii
ACKNOWLEDGMENTS.....	iv
LIST OF FIGURES.....	vii
1. Introduction.....	1
1.1 Ordered magnetic materials.....	1
1.2 Spin waves in ferromagnets.....	5
1.3 Experimental techniques for studying spin waves.....	10
1.4 Outline of thesis.....	12
2. Linear and Nonlinear Spin Wave Processes for a Nanowire.....	15
2.1 Spin Hamiltonian for a nanowire.....	15
2.2 Hamiltonian in terms of boson operators.....	16
2.2.1 Equilibrium spin orientation and boson operator expansion.....	16
2.2.2 Transformation to wavenumber space.....	18
2.3 Linear spin waves and the Bogoliubov transformation.....	21
2.4 The three-magnon and Four-magnon interaction terms.....	23
3. The Diagrammatic Perturbation Formalism.....	26
3.1 Outline of standard diagrammatic perturbation theory.....	27
3.1.1 Diagrammatic representation.....	29
3.1.2 The interacting Green's function.....	31
3.2 Extension of the diagrammatic method to the magnetic nanowire.....	35
3.2.1 Proper self energy for the three-magnon interactions.....	36
3.2.2 Proper self energy for the four-magnon interactions.....	41

4. Results for Longitudinal and Transverse Applied Magnetic Field.....	44
4.1 Longitudinal applied magnetic field.....	44
4.1.1 Linear SW behaviour for a longitudinal field.....	45
4.1.2 SW renormalization for a longitudinal field.....	46
4.2 Transverse applied magnetic field.....	51
4.2.1 Linear SW behaviour for a transverse field.....	51
4.2.2 SW renormalization for a transverse field.....	43
5. Results for Oblique Applied Magnetic Field.....	58
5.1 Applied magnetic field at $\alpha = \pi/4$	58
5.1.1 Linear SW behaviour for $\alpha = \pi/4$	59
5.1.2 SW renormalization for $\alpha = \pi/4$	61
5.2 Applied magnetic field at $\alpha = 4\pi/9$	62
5.2.1 Linear SW behaviour for $\alpha = 4\pi/9$	63
5.2.2 SW renormalization for $\alpha = 4\pi/9$	64
6. Conclusions.....	66
6.1 Review of the thesis.....	66
6.2 Possible extensions.....	69
APPENDIX A.....	72
APPENDIX B.....	73
REFERENCES.....	75
CURRICULUM VITAE.....	78

LIST OF FIGURES

1.1	Simple schematic representation of (a) ferromagnet, (b) ferrimagnet, and (c) antiferromagnet.....	2
1.2	Schematic representation of spins in a ferromagnet: (a) for the ground state, and (b) an excited state corresponding to a spin wave (SW) or magnon.....	6
2.1	(a) Schematic diagram of a line of spins canted at angle in the presence of an oblique external magnetic field; (b) Transformation to a new set of coordinates y' and z' defined such that the direction of magnetization is aligned with the z' -axis.	16
3.1	An interaction vertex $v(q)$ represented by the dashed line, carrying wavenumber q and the label τ	30
3.2	The two first order diagrams with no external lines.....	30
3.3	Examples of second order diagrams with no external lines that are (a) linked and (b) unlinked (i.e., that separate into parts).....	31
3.4	Diagrammatic representation of a Green's function. The shaded region represents any allowed diagrammatic structure of lines and interaction vertices.....	32
3.5	(a) A diagrammatic structure that is not a proper self energy diagram. (b) An example of a proper self energy diagram.....	33
3.6	A series of diagrams for the interacting Green's function in terms of the non-interacting Green's function and proper self energy Σ	34
3.7	The vertices of the 3 rd order Hamiltonian represented diagrammatically. The dots represent the interaction vertices.....	36
3.8	All distinct linked diagrams with no external lines for each conjugate pair of vertices.....	37
3.9	Proper self energy diagrams corresponding to the first diagram in Fig. 3.8.....	38
3.10	Proper self energy diagrams corresponding to the second diagram in Fig. 3.8.....	38
3.11	Proper self energy diagram corresponding to the third diagram in Fig. 3.8.....	38
3.12	Diagrammatic representation of the vertices for the four-magnon processes.....	41

3.13	First order proper self energy diagrams due to the Λ_1 vertex.....	42
3.14	Second order proper self energy diagrams due to the Λ_2 and Λ_3 vertices.....	43
3.15	Second order proper self energy diagram due to a pair of vertices.....	43
4.1	Linear SW dispersion relation for varying dipole-exchange ratio R_{DE} and external field b	47
4.2	SW energy shift vs. wavenumber ka at reduced temperature $T_R = 0.1$, dipole-exchange ratio $R_{DE} = 0.1$ and two values of the longitudinal field b	49
4.3	SW energy shift vs. wavenumber ka at longitudinal field $b = 0.01$, dipole-exchange ratio $R_{DE} = 0.05$, and temperature $T_R = 0.1$	50
4.4	SW energy shift vs. wavenumber ka at longitudinal field $b = 0.01$, dipole-exchange ratio $R_{DE} = 0.1$, and temperature $T_R = 0.3$	50
4.5	Plot of E_k vs. B_0/B_C for dipole-exchange ratio of $R_{DE} = 0.1$ and several values of ka	52
4.6	Plot of the SW dispersion relation for various B_0/B_C and $R_{DE} = 0.1$	53
4.7	SW damping vs. wavenumber at $R_{DE} = 0.1$ and $T_R = 0.3$: (a) $B_0/B_C = 0.1$, (b) $B_0/B_C = 0.7$, (c) $B_0/B_C = 0.95$, and (d) $B_0/B_C = 0.99$. Contributions from the splitting (black) and confluence (red) processes are shown.....	55
4.8	Damping vs. wavenumber at $T_R = 0.3$, $B_0/B_C = 0.7$, $R_{DE} = 0.05$	57
4.9	Damping vs. wavenumber at $T_R = 0.1$, $B_0/B_C = 0.7$, $R_{DE} = 0.1$	57
5.1	Plot of θ (in radians) vs. B_0/B_C for a field orientation $\alpha = \pi/4$. The horizontal dashed line is at the asymptotic value corresponding to $\alpha = \pi/4 \approx 0.785$	59
5.2	Plot of fixed wavenumber energy vs. B_0/B_C at $R_{DE} = 0.1$	60
5.3	Plot of the SW dispersion relation for various B_0/B_C at $\alpha = \pi/4$ and $R_{DE} = 0.1$	60

5.4	Damping vs. Wavenumber at $R_{DE} = 0.1$, $T_R = 0.3$, (a) $B_0/B_C = 0.1$, (b) $B_0/B_C = 0.7$, (c) $B_0/B_C = 1.0$, and (d) $B_0/B_C = 2.0$	62
5.5	Plot of zero $E_{k=0}$ vs. B_0/B_C at $R_{DE} = 0.1$ for different field orientations.....	63
5.6	Plot of the SW dispersion relation for various B_0/B_C at $\alpha = 4\pi/9$ and $R_{DE} = 0.1$	64
5.7	Damping vs. Wavenumber at $R_{DE} = 0.1$, $T_R = 0.3$, (a) $B_0/B_C = 0.1$, (b) $B_0/B_C = 0.7$, (c) $B_0/B_C = 1.0$, and (d) $B_0/B_C = 2.0$	65
6.1	Schematic representations of two wire-like geometries with (a) $N_0 = 3$ and (b) $N_0 = 7$. The applied field is taken to be along the symmetry axis (z-direction).....	70
6.2	Dispersion relation for three lines of spin for $b = 0.1$ and $R_{DE} = 0.1$. The dots and arrow indicate some possible splitting processes.....	71
B.1	Some ways of connecting vertices to obtain the same proper self energy diagrams. Each colour (red, green, purple) corresponds to a different possible permutation.....	73

CHAPTER 1

Introduction

There are many classes of magnetic material. In fact all materials can exhibit magnetic properties under the right condition (i.e., if a “nonmagnetic” material is placed inside a sufficiently large magnetic field a magnetic moment may be induced). The most common classification has five categories: diamagnetism, paramagnetism, ferromagnetism, antiferromagnetism, and ferrimagnetism [1, 2]. Diamagnetism and paramagnetism are weak effects that differ by the sign of the magnetic susceptibility χ , which is the proportionality constant between the external field and the magnetization produced in the material. For diamagnetic materials χ is a negative quantity, indicating an induced magnetic moment opposite to the external field, and positive for paramagnetic materials. These materials are considered weak magnetic materials since the magnitude of χ is typically of order 10^{-3} or less. The materials of interest for the work to be presented here are ordered magnetic materials, where χ may be several orders of magnitude larger. Specifically we shall be concerned with ferromagnetic materials, but we begin with a brief discussion of the various classes of ordered magnetic materials and some of their properties.

1.1 Ordered magnetic materials

Ordered magnetic solids typically have magnetic ions localized at lattice sites, and there are interactions between the ions that give rise to the magnetic order. The ordering of these magnetic ions either may or may not produce a net magnetization M for the

solid as a whole. If $M \neq 0$, which is the case for ferromagnets and ferrimagnets, the solid exhibits a macroscopic bulk magnetization even in a zero external field, i.e., there is a *spontaneous magnetization*. However, there is another important class of materials called antiferromagnets for which $M = 0$ and yet they have a magnetically ordered structure.

Some simple schematic illustrations for the various magnetically ordered structures [1, 2] are given in Fig. 1.1, where the arrows represent the direction and magnitude of the net spin angular momentum at any lattice site. In the case of ferromagnets the spins preferentially align in the same direction, while in the case of ferrimagnets and antiferromagnets the adjacent spins preferentially align antiparallel with respect to one another. For ferrimagnets and antiferromagnets there are two sublattices, each having a net magnetization, but in the opposite directions. For antiferromagnets the sublattice magnetizations are of equal magnitudes and therefore $M = 0$ for the solid as a whole. For ferrimagnets the sublattice magnetizations do not fully cancel, which leads to $M \neq 0$.

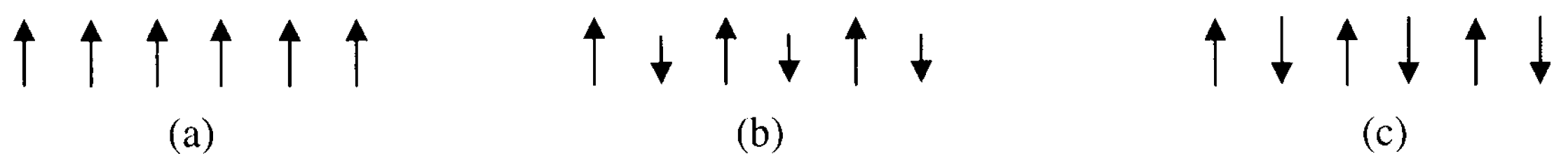


Fig. 1.1: Simple schematic representation of (a) ferromagnet, (b) ferrimagnet, and (c) antiferromagnet.

The ordering of magnetic materials only exists below a critical temperature, which varies from material to material. This critical temperature is called the Curie temperature T_C for ferromagnets and ferrimagnets and the Néel temperature T_N for antiferromagnets.

Some ferromagnetic materials are: iron (Fe), Cobalt (Co) and Nickel (Ni) with corresponding T_C values of 700 C, 1130 C, and 358 C, respectively.

The strongest type of interaction, which gives rise to the magnetic ordering, is called the Heisenberg exchange interaction (see, e.g., [1, 3, 4, 5]). It is strictly a quantum mechanical phenomenon arising as a consequence of the Pauli Exclusion Principle, which requires that the total wave function of a pair of electrons at neighbouring ions must be antisymmetric with respect to the interchange of the electrons. It means that the energy of the state in which the spins are parallel is generally different from that in which the electrons spins are antiparallel. The Heisenberg Hamiltonian which describes this interaction between all pairs of spins (at sites labelled i and j) is

$$H_H = -\frac{1}{2} \sum_{i,j} J_{i,j} \vec{S}_i \cdot \vec{S}_j, \quad (1.1)$$

where $J_{i,j}$ is called the exchange integral and is related to the overlapping of the wave functions centred at i and j , \vec{S}_i is the spin angular momentum vector at site i , and the $1/2$ is to avoid double counting. Typically $J_{i,j}$ is appreciable only between nearest neighbours, and will be denoted by J . For ferromagnets J is a positive quantity, since the minimum energy corresponds to a parallel alignment of spins as depicted in Fig. 1.1(a). For antiferromagnets and ferrimagnets J is a negative quantity indicating a preference for antiparallel alignment between nearest neighbour spins.

The other form of interaction in magnetic systems is electromagnetic and is due to the magnetic dipole-dipole interactions described by Maxwell's equations [6, 7]. This form of interaction is significantly weaker than the exchange, but it is long range in nature. Since each spin interacts with all other spins in the lattice, the contribution due to

dipolar interactions can add up to be significant in certain regimes, as will be discussed later. The contribution to the spin Hamiltonian is

$$H_{Dipole} = \frac{1}{2} g^2 \mu_B^2 \sum_{i,j} \sum_{\alpha,\beta} D_{i,j}^{\alpha,\beta} S_i^\alpha S_j^\beta, \quad (1.2)$$

where g is the Landé g -factor, μ_B is the Bohr magneton, α and β are the Cartesian coordinate x, y, z , and $D_{i,j}^{\alpha,\beta}$ is given by

$$D_{i,j}^{\alpha,\beta} = \frac{|\vec{r}_{i,j}|^2 \delta_{\alpha,\beta} - 3r_{i,j}^\alpha r_{i,j}^\beta}{|\vec{r}_{i,j}|^5}. \quad (1.3)$$

Here $\vec{r}_{i,j} = \vec{r}_j - \vec{r}_i$ is the vector displacement between spins i and j .

Finally, if we place a ferromagnetic sample in an external applied magnetic field \vec{B}_0 there is an additional potential energy term in the Hamiltonian given by

$$H_{Field} = -g\mu_B \vec{B}_0 \cdot \sum_i \vec{S}_i. \quad (1.4)$$

We now consider the thermal average $\langle S^z \rangle$, which is proportional to the magnetization M . Its temperature dependence can be approximated using mean-field theory originally proposed by Weiss in 1907 (see, e.g., [1, 2]). If we take the applied field and magnetization to be along the z -direction and ignore spin fluctuations, the Hamiltonian in Eq. (1.1), together with the applied field term in Eq. (1.4), can be re-expressed as

$$H_{MF} = -g\mu_B \sum_i [B_0 + B_E(i)] S_i^z, \quad (1.5)$$

where $B_E(i)$ is the effective field acting on spin \vec{S}_i due to the exchange interactions:

$$g\mu_B B_E(i) = \sum_j J_{i,j} \langle S_j^z \rangle. \quad (1.6)$$

For a system with spin $S=1/2$, for which the eigenvalues of S^z are $\pm 1/2$, it is straightforward to find $\langle S^z \rangle$. Using the general definition of thermal average [8]

$$\langle A \rangle = \frac{1}{Q} \text{Tr}(A e^{-H/k_B T}), \quad (1.7)$$

for any operator A , where Tr denotes the trace and $Q = \text{Tr}(e^{-H/k_B T})$ is the partition function, we find

$$\langle S^z \rangle = \frac{1}{2} \tanh[g\mu_B (B_0 + B_E) / 2k_B T]. \quad (1.8)$$

Since B_E is proportional to $\langle S^z \rangle$, Eq. (1.8) can be solved self-consistently to find $\langle S^z \rangle$ for any given value of B_0 and T . For other values of S , Eq. (1.8) has a more complicated form, involving Brillouin functions [1, 9]. In the general case it is found that $\langle S^z \rangle \rightarrow 0$ for $T \rightarrow T_C = S(S+1)J(0)/3k_B$ when $B_0 = 0$. This mean-field estimate for T_C applies for the Heisenberg exchange case only.

1.2 Spin waves in ferromagnets

The focus of this thesis is on the dynamical properties of ferromagnetic materials, i.e., on the fluctuations in the magnetization that can be analyzed in terms of spin waves (SWs). The SWs can either be described semi-classically [2] or using a quantum mechanical approach [10]. We will begin with a simple semi-classical description of SWs, assuming for simplicity an array of spins with only nearest-neighbour exchange

interactions (a Heisenberg ferromagnet). The ground state corresponds to all the spins lined up, as depicted in Fig. 1.2(a). We might suppose that the first excited state of this system would correspond to reversing one of the spins anti-parallel to the rest. From Eq. (1.1) it follows that the difference between the ground state energy and this presumed excited state is $2JS^2$, which is a significant increase in the total energy. We now show that there are excited states with much lower energy if we allow the spin reversal to be shared amongst all the spins. Since the nearest-neighbour exchange energy involving the j^{th} spin is $-J\vec{S}_j \cdot (\vec{S}_{j+1} + \vec{S}_{j-1})/2$ and the magnetic moment of the j^{th} spin is $\vec{\mu}_j = g\mu_B\vec{S}_j$, we can rewrite this exchange energy for the j^{th} spin as $-\vec{\mu}_j \cdot \vec{B}_j^{\text{eff}}$, where

$$\vec{B}_j^{\text{eff}} = (J/2g\mu_B)(\vec{S}_{j+1} + \vec{S}_{j-1}) \quad (1.9)$$

is the effective magnetic field at site j . From classical mechanics we know that the rate of change of the angular momentum $\hbar d\vec{S}_j/dt$ is equal to the torque on the magnetic moment due to the effective field [11]:

$$\hbar d\vec{S}_j/dt = \vec{\mu}_j \times \vec{B}_j^{\text{eff}} = \frac{1}{2}J\vec{S}_j \times (\vec{S}_{j+1} + \vec{S}_{j-1}). \quad (1.10)$$

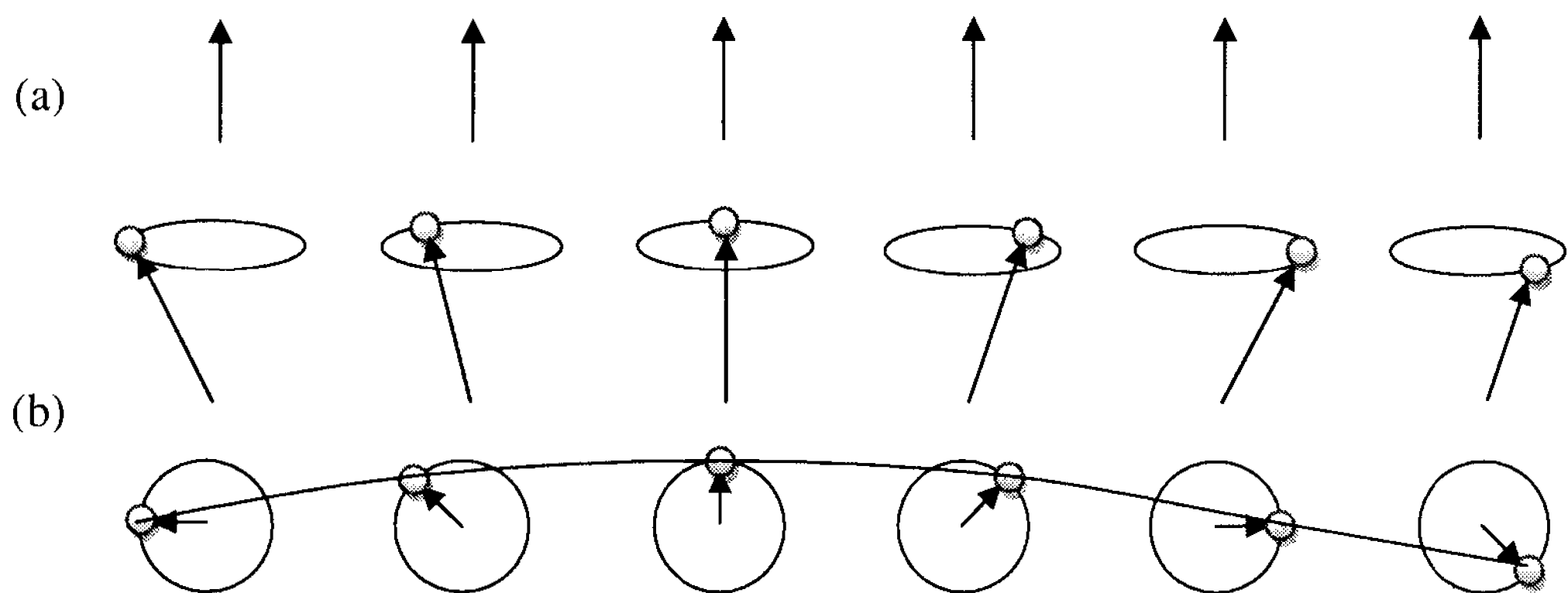


Fig. 1.2: Schematic representation of spins in a ferromagnet: (a) for the ground state, and (b) an excited state corresponding to a spin wave (SW) or magnon.

When Eq. (1.10) is written in component form, each equation involves products of spin components making the differential equations nonlinear. These equations can be linearized by considering small spin deviations such that $S^z \approx S$, or equivalently $|S^x|, |S^y| \ll S$. Neglecting small terms involving the product of S^x and S^y we can write

$$dS_j^x / dt = (SJ / 2\hbar)(2S_j^y - S_{j+1}^y - S_{j-1}^y) \quad , \quad dS_j^y / dt = -(SJ / 2\hbar)(2S_j^x - S_{j+1}^x - S_{j-1}^x) \quad (1.11)$$

and $dS_j^z / dt = 0$. We expect solutions for the spin components that are traveling waves, and so as a trial solution we choose

$$S_j^x = u \exp[i(jka - \omega t)] \quad \text{and} \quad S_j^y = v \exp[i(jka - \omega t)], \quad (1.12)$$

where u and v are constants, j is an integer label, and a is the spacing between spins.

By substituting Eq. (1.12) into Eq. (1.11) we find the expressions

$$-i\omega\hbar u = SJ[1 - \cos(ka)]v \quad \text{and} \quad -i\omega\hbar v = -SJ[1 - \cos(ka)]u. \quad (1.13)$$

From these expressions we find $u = iv$ and the SW dispersion relation

$$\hbar\omega = SJ[1 - \cos(ka)]. \quad (1.14)$$

Also it follows that the real part of the traveling waves in Eq. (1.12) correspond to $S_j^x = u \cos(jka - \omega t)$ and $S_j^y = u \sin(jka - \omega t)$, which describe a circular precession of each spin about the z -axis. Also, by inspection, we see that the phase shift between adjacent spins is ka . The quanta for these SW excitations in magnetically ordered materials are called magnons (by analogy with phonons as the quanta for lattice vibrations), and they are schematically depicted in Fig. 1.2.

Now we will adopt a quantum-mechanical approach to verify the semi-classical result for the SW dispersion relation. In order to gain more insight we will consider a slightly more general system, composing of a Heisenberg ferromagnet in three dimensions placed in an external applied magnetic field in the direction of magnetization (taken as the z -direction). The Hamiltonian is just the sum of Eqs. (1.1) and (1.4), which can be re-expressed in terms of the usual spin operators S^+ , S^- , and S^z , where we define $S^\pm = S^x \pm iS^y$. These operators satisfy the following commutation relations [12]:

$$[S_i^+, S_j^-] = 2\hbar S_i^z \delta_{i,j} \quad \text{and} \quad [S_i^z, S_j^\pm] = \pm \hbar S_i^\pm \delta_{i,j}, \quad (1.15)$$

where we employ the notation $[A, B] = AB - BA$. The re-expressed Hamiltonian is

$$H = -\frac{1}{2} \sum_{i,j} J_{i,j} \left[\frac{1}{2} (S_i^+ S_j^- + S_i^- S_j^+) + S_i^z S_j^z \right] - g\mu_B B_0 \sum_i S_i^z. \quad (1.16)$$

From Eq. (1.16) and the quantum-mechanical equation of motion [12] for any operator A :

$$i\hbar dA/dt = [A, H], \quad (1.17)$$

we can find the time variation of the operator S_i^+ as

$$i\hbar dS_i^+ / dt = g\mu_B B_0 S_i^+ + \sum_j J_{i,j} (S_j^z S_i^+ - S_i^z S_j^+). \quad (1.18)$$

If we assume that the spins are well aligned in the z -direction we can simplify Eq. (1.20) by using the so-called *random-phase approximation* [13]:

$$(S_j^z S_i^+ - S_i^z S_j^+) \rightarrow \langle S_j^z \rangle S_i^+ - \langle S_i^z \rangle S_j^+. \quad (1.19)$$

Essentially, we are decoupling the spin operators so that each S_i^z is replaced by its nonzero thermal average $\langle S^z \rangle = \langle S_i^z \rangle = \langle S_j^z \rangle$. Next we Fourier transform to wavevector space using

$$S_j^+ = \frac{1}{N} \sum_k S_k^+ \exp(i\vec{k} \cdot \vec{r}_j) \quad , \quad J_{i,j} = \frac{1}{N} \sum_k J(\vec{k}) \exp[i\vec{k} \cdot (\vec{r}_i - \vec{r}_j)]. \quad (1.20)$$

From Eqs. (1.18), (1.19), and (1.20) the equation of motion can be expressed in the form

$$i\hbar dS_k^+ / dt = \omega_B(\vec{k}) S_k^+, \quad (1.21)$$

Where the SW dispersion relation is

$$\hbar \omega_B(\vec{k}) = g\mu_B B_0 + \langle S^z \rangle [J(0) - J(\vec{k})]. \quad (1.22)$$

This corresponds to a simple harmonic oscillator with angular frequency $\omega_B(\vec{k})$. The minimum SW frequency is at $\vec{k} = 0$, where $\omega_B(0) = g\mu_B B_0$. This limit is called *ferromagnetic resonance frequency* and it corresponds to the classical picture of all spins precessing in phase around the applied field B_0 . It is easy to see that Eq. (1.22) is equivalent to Eq. (1.14). In the simple cubic lattice it can be verified that

$$J(\vec{k}) = 2J[\cos(k_x a) + \cos(k_y a) + \cos(k_z a)]. \quad (1.23)$$

Here we have a three-dimensional wavevector \vec{k} replacing the single component k . The additional term $g\mu_B B_0$ in Eq. (1.22) is due to the external field. For a film-like geometry involving planes of spin we would expect a dispersion relation described by a two-dimensional wavevector [14, 15].

It is evident from both our classical and quantum-mechanical calculations that the SWs are not exact eigenstates of the Hamiltonian. In each case there was a “linearizing” approximation, corresponding to the neglect of small terms when evaluating the cross product in Eq. (1.10) or using the random-phase approximation in Eq. (1.18). This means that there are SW interaction processes that have so far been ignored. The theory of SW interactions in Heisenberg ferromagnets was first developed rigorously by Dyson [16] in terms of four-magnon processes. Later other authors developed more practical methods and also extended the analysis to include the dipole-dipole interactions by showing that three-magnon processes also occur. Reviews of SW interactions in bulk ferromagnets can be found in Refs. [4, 9, 15, 17], while calculations for thin films are given in Refs. [15, 18, 19].

1.3 Experimental techniques for studying spin waves

There are three main experimental techniques for studying SWs: inelastic neutron scattering, inelastic light scattering, and spin wave resonance (see, e.g., [1, 2, 10]). Here we will give a brief discussion of these techniques.

We begin with inelastic neutron scattering. A neutron “sees” two aspects of a crystal: the distribution of nuclei and the distribution of electronic magnetization. The magnetic moment of a neutron interacts with the magnetic moment of the electron. A neutron can be inelastically scattered by the magnetic structure creating or annihilating a SW. From the conservation of energy and momentum the scattered neutron can be used to deduce the dispersion relation of the SW across the full Brillouin zone. Furthermore

diffraction of neutrons enables the determination of the magnetic structure of the crystal. The cross section for the neutron-electron interaction is of the same order of magnitude as the neutron-nuclear interaction. This cross section is relatively small in comparison to other magnon interactions (e.g., magnon-photon scattering). Neutron scattering is so weak that it is only appropriate for studying SWs in bulk materials.

There are two main types of inelastic light scattering, namely, Brillouin light scattering (BLS) and Raman light scattering (RLS). In terms of the magnetic excitations BLS is in effect an inelastic scattering of a photon that creates or annihilates a SW. This inelastic interaction induces a shift in the frequency of the incident light by a small amount that corresponds to the frequency of the SWs involved, much as in the neutron scattering phenomenon. The shift is commonly measured by using a spectrometer based on a Fabry-Pérot interferometer. RLS is conceptually similar to BLS, but the detected frequency shift and type of information extracted for the two cases are quite different. For RLS the photons typically interact with vibrational and rotational transitions in single molecules or the higher-frequency SWs in antiferromagnets, while BLS involves lower-frequency excitations such as acoustic phonons or SWs in ferromagnets. For RLS the typical range of frequency shifts measured is $\sim 1.5 \times 10^{11}$ Hz to $\sim 10^{14}$ Hz, while for the Brillouin scattering the frequency shifts are typically up to about $\sim 1.5 \times 10^{11}$ Hz.

Another common experimental technique used for the study of SWs at small wavevectors is ferromagnetic resonance (FMR). Referring to Eq. (1.22) we see that in the limit $\vec{k} \rightarrow 0$ the frequency corresponds to the *FMR frequency* given simply by $g\mu_B B_0$, but more generally there may be additional anisotropy terms. Typically the external field values used in these experiments are in the order of up to a few Tesla,

which may correspond to resonance frequencies in the microwave range or higher. The basic setup for a FMR experiment involves placing a ferromagnetic sample between the poles of an electromagnet inside a microwave cavity, and a RF field is applied. When the frequency of the RF field matches the frequency of the SW at $\vec{k} = 0$, there is a resonant absorption of microwave energy as measured by a photodiode.

Also it has recently been shown that spin-polarized electrons can be used to excite surface magnons [20]. This promising technique allows experimentalist to study the dispersion relation for ultrathin magnetic materials, where surface effects dominate.

In the above methods it is usually possible to measure linewidth associated with the SWs, as well as their frequencies. For example, in FMR the intensity of the incident microwave is measured as a function of the sweeping magnetic field, and so the linewidth has units corresponding to the magnetic field. This linewidth is directly connected to the SW relaxation time or damping (essentially the reciprocal of the lifetime), a part of which comes from SW interactions. Some of the experiments techniques described above (especially BLS and FMR that have high resolution) can be used to deduce damping effects due to SW interactions.

1.4 Outline of the thesis

The focus of this thesis is on the nonlinear properties of the dipole-exchange SWs in ultrathin ferromagnetic nanowires, as modeled by a single line of spin placed in an oblique magnetic field. In recent years it has become possible to fabricate high-quality samples of ferromagnetic nanowires (e.g., of Ni and Permalloy) and to study the SW modes in these nanowires experimentally by BLS (see, e.g., [21, 22]) and FMR (see, e.g.,

[23, 24]). The first detailed experimental study of SW damping [23] in a ferromagnetic nanowire of Permalloy is particularly significant in motivating the work in this thesis. Much of the interest in magnetic nanowires, as well as in other magnetic nanostructures, arises due to technological applications being developed as magnetic sensors, magnetic storage devices, and high-frequency (microwave and above) magnetic devices (see, e.g., [25, 26]). On the theoretical side, there have been several detailed studies of the linear SW properties in nanowires (see, e.g., [27, 28]), but none (until now) of the nonlinear SW processes. We will now give a brief outline of the thesis.

In Chapter 2 a spin Hamiltonian is presented for the system. Using a standard transformation the Hamiltonian is first re-expressed in terms of boson creation and annihilation operators to study the SW properties. In a low-temperature regime $T \ll T_c$ the Hamiltonian is expanded in terms of products of these boson operators, accounting for all terms up to and including the fourth order. The terms that are of first and second order in products of operators are used to find an expression for the equilibrium orientation of the spins (i.e., the canting of the spins due to the external magnetic field) and a dispersion relation for the non-interacting (or linearized) SWs, respectively. The third and fourth order terms are used to find the renormalization effects (namely, the energy shift and damping) due to three-magnon and four-magnon interactions, respectively.

In Chapter 3 an interacting Green's function formalism is used, in combination with diagrammatic perturbation techniques, in order to find explicit expressions from which the SW energy shift and damping can be deduced. The energy shift and damping for the three-magnon processes are analyzed in detail. The four-magnon processes are discussed more briefly, except for the leading order expression for the SW energy shift in

the case of a longitudinal external magnetic field.

In Chapter 4 the numerical results deduced from the expressions in the previous chapter are presented for two special cases, where the applied external field is in the longitudinal and transverse directions with respect to the symmetry axis of the wire. In the special case of a longitudinal field the three-magnon processes are shown to vanish, and so the focus is on the four-magnon energy renormalization. Plots of energy shift vs. wavenumber are presented along with the linear SW dispersion curves so that an overall interpretation of the results can be given. In the transverse field case it is shown that there is a critical value of the field above which the magnetization switches into alignment with the field. The focus of discussion is then on the three-magnon damping. Plots of damping vs. wavenumber are presented along with the corresponding linear SW dispersion curves.

In Chapter 5 we move on to investigate numerically oblique field directions that are intermediate between those considered in Chapter 4. This is done in order to generalize the three-magnon damping dependence on the external applied field. A difference is that there is no analogous critical field behaviour. Plots of damping vs. wavenumber are again presented for two different oblique field orientations.

Chapter 6 contains the conclusions along with some suggested extensions of this work.

CHAPTER 2

Linear and Nonlinear Spin Wave Processes for a Nanowire

2.1 Spin Hamiltonian for a nanowire

In the simplest case an ultrathin nanowire can be modeled by a single line of spins, which are at fixed locations along the z -axis and placed in an oblique external magnetic field (at variable angle α relative to the z -axis). The spin Hamiltonian for this system is represented by the sum of the terms as in Eqs. (1.1), (1.2) and (1.4):

$$\begin{aligned}
 H = & -\frac{1}{2} \sum_{i,j} J_{i,j} \vec{S}_i \cdot \vec{S}_j + \frac{1}{2} g^2 \mu_B^2 \sum_{i,j} \sum_{\alpha,\beta} D_{i,j}^{\alpha,\beta} S_i^\alpha S_j^\beta \\
 & - g \mu_B B_0 \left(\cos \alpha \sum_i S_i^z + \sin \alpha \sum_i S_i^y \right)
 \end{aligned} \tag{2.1}$$

The first term in the Hamiltonian is the short range exchange interaction [1, 2], where \vec{S}_i is the spin operator at the site i , and $J_{i,j}$ is the exchange energy between the i^{th} and the j^{th} spin in the array. For a ferromagnetic wire $J_{i,j}$ is positive as discussed in Chapter 1. Furthermore $J_{i,j}$ is assumed to be non-vanishing only for nearest neighbours ($J_{i,j} = J \delta_{i,j \pm 1}$). The second term in the Hamiltonian is the long-range dipole-dipole interaction [6] with $D_{i,j}^{\alpha,\beta}$ defined in Eq. (1.3). The dipole energy is minimized when the equilibrium alignments of the spins is along the z -axis. The third term in the Hamiltonian is the Zeeman energy due to the external magnetic field B_0 in the yz -plane. For $\alpha \neq 0$ the applied field leads to a canting of the equilibrium spin orientation away from the z -axis in order to minimize the total free energy of the system. The geometry for the nanowire of equally spaced spins (each separated by distance a) is shown schematically

in Fig. 2.1(a), where θ is the canting angle of each spin and α is the orientation of the external field in the yz -plane relative to the z -axis.

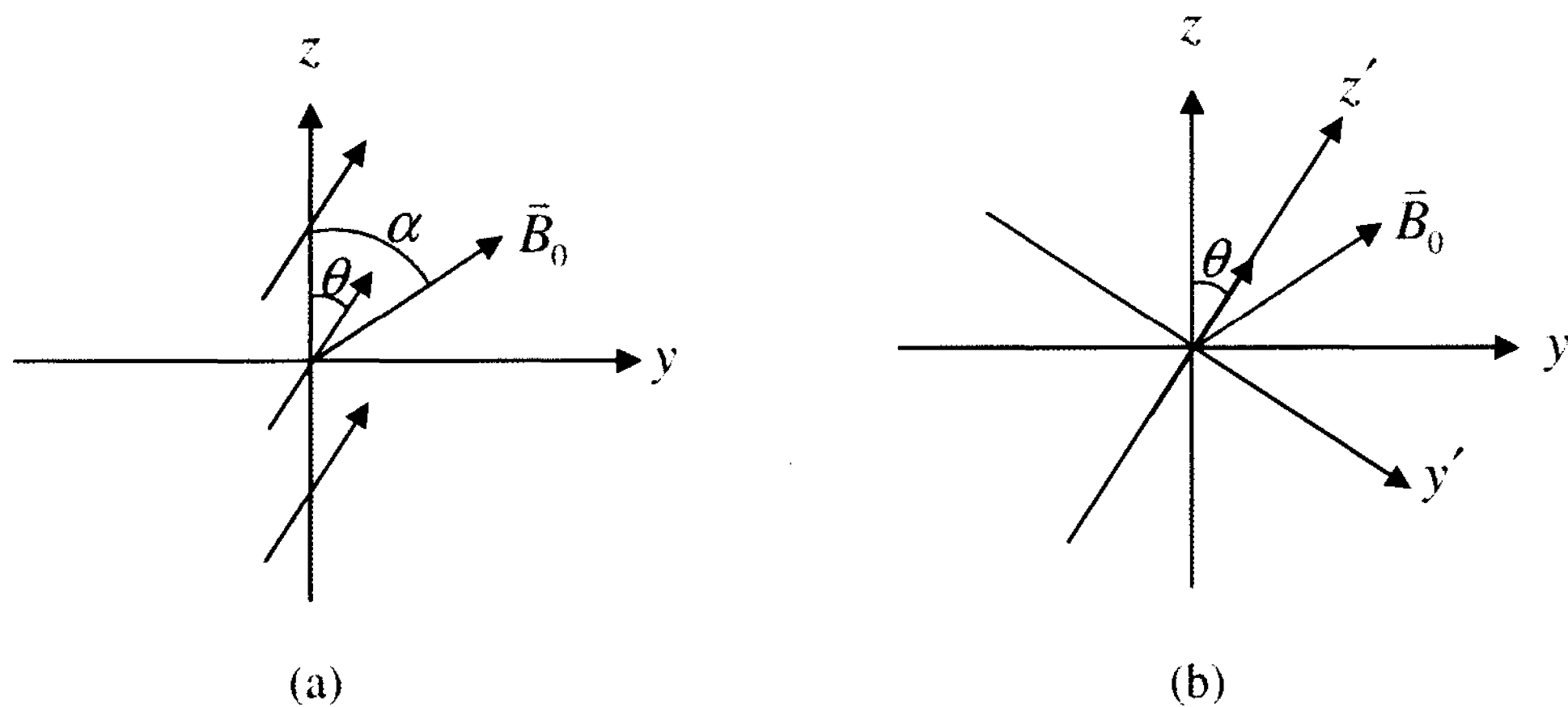


Figure 2.1: (a) Schematic diagram of a line of spins canted at angle θ in the presence of an oblique external magnetic field; (b) Transformation to a new set of coordinates y' and z' defined such that the direction of magnetization is aligned with the z' -axis.

2.2 Hamiltonian in terms of boson operators

Next, applying appropriate transformations, the spin Hamiltonian will be re-expressed in terms of a set of boson operators in wavenumber space from which the linear spin-wave (SW) dispersion relation can be deduced. Also the nonlinear interaction terms will be systematically evaluated for later use in a perturbation analysis.

2.2.1 Equilibrium spin orientation and boson operator expansion

As mentioned, when an oblique field with a component in the transverse direction is applied, the spins cant away from the z -axis by some angle $0 \leq \theta \leq \pi/2$ to be determined. It will become clear later that the spins do not necessarily align parallel to the external field, because of the competing interaction terms in the Hamiltonian. To simplify the subsequent analysis a new coordinate system (x', y', z') is selected such that

the equilibrium spin orientation is along the z' -axis as illustrated in Fig. 2.1(b). The transformation is done by applying a rotation matrix [11] to the components of the spin operators in the yz -plane:

$$\begin{pmatrix} S^y \\ S^z \end{pmatrix} = \begin{pmatrix} \cos \theta & \sin \theta \\ -\sin \theta & \cos \theta \end{pmatrix} \begin{pmatrix} S^{y'} \\ S^{z'} \end{pmatrix}. \quad (2.2)$$

The x -component of the spin is unaffected ($S^x = S^{x'}$). The $D_{i,j}^{\alpha,\beta}$ coefficients, which are geometric sums, are not transformed because they are simplest in the original symmetry-related coordinates (x, y, z) . In fact it is easy to show from Eq. (1.3) that in the original coordinates only the diagonal components are nonzero and are related by

$$-2D_{i,j}^{x,x} = -2D_{i,j}^{y,y} = D_{i,j}^{z,z} = -2/|z_{i,j}|^3. \quad (2.3)$$

The canting angle θ for any choice of the external-field angle α will be determined self-consistently later.

In order to utilize the diagrammatic perturbation method (see Chapter 3) the spin operators in the Hamiltonian Eq. (2.1) will be replaced by boson creation and annihilation operators. This is done by applying the standard Holstein-Primakoff transformation [5, 17] defined relative to the *transformed* coordinate system (x', y', z') :

$$S_i^+ = \sqrt{2S} \left(1 - \frac{a_i^+ a_i}{2S}\right)^{1/2} a_i, \quad S_i^- = \sqrt{2S} a_i^+ \left(1 - \frac{a_i^+ a_i}{2S}\right)^{1/2},$$

$$S_i^{z'} = S - a_i^+ a_i, \quad (2.4)$$

where S_i^+ , and S_i^- are the usual raising and lowering spin angular momentum operators [12, 29] defined here by $S^\pm = S^x \pm iS^y$. The boson operators satisfy the simple commutation relations [29, 30]

$$[a_i, a_j^+] = \delta_{i,j}, \quad [a_i, a_j] = [a_i^+, a_j^+] = 0, \quad (2.5)$$

following the notation in Section 1.2. It is straightforward to verify that the definitions in Eq. (2.4) reproduce the known spin commutation relations in Eq. (1.15).

The spin operators in the Holstein-Primakoff transformation can now be approximated in the low temperature regime $T \ll T_C$, where T_C is the Curie temperature. At low temperatures the spins are well aligned along the z' -axis, so that $S_i^{z'} \approx S$ for each spin. From Eq. (2.4) it follows that $a_i^+ a_i / 2S \ll 1$, and so using the binomial expansion the operators S_i^+ and S_i^- can be written as

$$S_i^+ = \sqrt{2S} \left(a_i - \frac{1}{4S} a_i^+ a_i a_i + \dots \right), \quad S_i^- = \sqrt{2S} \left(a_i^+ - \frac{1}{4S} a_i^+ a_i^+ a_i + \dots \right). \quad (2.6)$$

Hence the transformed Hamiltonian in the new coordinate system can be expanded in terms of products of boson creation and annihilation operators.

2.2.2 Transformation to wavenumber space

As a final step before restating the Hamiltonian in the desired form, we take advantage of the translational symmetry of the wire along its length (the original z -axis) to convert all spatial labels (i and j) to wavenumber-space by applying a Fourier transform [29]. The dipolar $D_{i,j}^{\alpha,\beta}$ and the exchange $J_{i,j}$ terms can be replaced by

$$D_{i,j}^{\alpha,\beta} = \frac{1}{N} \sum_k D^{\alpha,\beta}(k) e^{-ik(z_i - z_j)}, \quad J_{i,j} = \frac{1}{N} \sum_k J(k) e^{-ik(z_i - z_j)}, \quad (2.7)$$

where N is the (macroscopically large) number of spins along the chain, and $z_i - z_j$ is the displacement between the i^{th} and the j^{th} spin. Here k is the longitudinal wavenumber along the symmetry direction z . Similarly, the boson operators can be

transformed as

$$a_i = \frac{1}{\sqrt{N}} \sum_k a_k e^{-ikz_i} \quad , \quad a_i^+ = \frac{1}{\sqrt{N}} \sum_k a_k^+ e^{ikz_i} \quad . \quad (2.8)$$

After applying these transformations and utilizing the identity [29, 31] that

$$\delta_{k,k'} = \frac{1}{N} \sum_i e^{i(k-k')z_i} \quad , \quad (2.9)$$

the Hamiltonian can be expressed as a series

$$H = H^{(0)} + H^{(1)} + H^{(2)} + H^{(3)} + H^{(4)} + \dots \quad , \quad (2.10)$$

where the superscript m of the Hamiltonian term $H^{(m)}$ refers to the number of boson operators in any product. There are several nice features when the Hamiltonian is expanded in this manner. For one, by including all terms up to a desired value of m (and neglecting higher orders), the degree of accuracy can be carefully controlled. Also each term in the expansion of the Hamiltonian can be associated with a specific physical process, as we will now discuss.

The zeroth-order ($m = 0$) Hamiltonian contains no operators and therefore it is just a contribution to the total energy of the system. Thus it does not directly provide any information about the dynamics of the system. The expression is

$$H^{(0)} = -\frac{1}{2} NS^2 J(0) - g\mu_B SNB_0 \cos(\alpha - \theta) - \frac{1}{16} g^2 \mu_B^2 4NS^2 (1 - 3\cos^2 \theta) D^{z,z}(0) \quad . \quad (2.11)$$

A first-order ($m = 1$) Hamiltonian would correspond to a process in which a single SW (at $k = 0$) is created or destroyed. Because the Holstein-Primakoff transformation was defined relative to the equilibrium spin axes (x', y', z') , $H^{(1)}$ should be identically zero. Formally, it is given by the expression

$$H^{(1)} = i\sqrt{\frac{NS}{2}}g\mu_B \left[\frac{3}{4}g\mu_B SD^{z,z}(0)\sin(2\theta) - B_0\sin(\theta - \alpha) \right] (a_0 - a_0^+), \quad (2.12)$$

and so, in order for the above expression to vanish identically, the following condition must be satisfied

$$\sin(2\theta) = \frac{4B_0}{3g\mu_B SD^{z,z}(0)} \sin(\theta - \alpha). \quad (2.13)$$

This is a stability condition from which the equilibrium canting angle θ may be deduced, which will be discussed later using examples.

The second-order ($m = 2$) Hamiltonian is related to the dispersion relation of the non-interacting (or linear) SWs propagating along the length of the wire. The expression for $H^{(2)}$ is

$$H^{(2)} = \sum_k X(k) a_k^+ a_k + \frac{1}{2} \sum_k Y(k) (a_k a_{-k} + a_k^+ a_{-k}^+), \quad (2.14)$$

where

$$X(k) = S(J(0) - J(k)) + g\mu_B B_0 \cos(\alpha - \theta) + \frac{1}{4} g^2 \mu_B^2 S (2D^{z,z}(0) + D^{z,z}(k)) (3\sin^2 \theta - 2),$$

$$Y(k) = -\frac{3}{4} g^2 \mu_B^2 SD^{z,z}(k) \sin^2 \theta. \quad (2.15)$$

All the higher-order terms in the Hamiltonian correspond to nonlinear SW effects (i.e., they describe the scattering of one or more SW into other SW states). The leading contributions arise from the third-order ($m = 3$) and fourth-order ($m = 4$) Hamiltonians, which correspond to the three-magnon and four-magnon processes, respectively. When considering the leading-order corrections to the linear dispersion relation one might be tempted to include effects due to $H^{(3)}$ but neglect the effects of $H^{(4)}$ and higher-order terms in the Hamiltonian. However, depending on the material under consideration, the

four-magnon process can often be of significance and should not automatically be neglected. For certain materials, at very small wave numbers where the dipole-dipole effects tend to dominate (the “dipolar” regime) the three-magnon process is typically predominant, while for larger wave numbers where exchange tends to be more important (the “exchange” regime) the four-magnon process might be significant. The expressions for the third-order and fourth-order Hamiltonians are

$$H^{(3)} = \frac{1}{2\sqrt{N}} \sum_{k_1, k_2, k_3} i\gamma \left\{ [D^{z,z}(k_1) + D^{z,z}(k_2)] a_{k_1}^+ a_{k_2}^+ a_{-k_3} - [D^{z,z}(k_2) + D^{z,z}(-k_3)] a_{k_1}^+ a_{-k_2} a_{-k_3} \right\} \delta_{\vec{k}_1 + \vec{k}_2 + \vec{k}_3, 0}, \quad (2.16)$$

$$H^{(4)} = \frac{1}{2N} \sum_{k_1, k_2, k_3, k_4} (\mu_1 a_{k_1}^+ a_{k_2}^+ a_{-k_3} a_{-k_4} + \mu_2 a_{k_1}^+ a_{k_2}^+ a_{k_3}^+ a_{-k_4} + \mu_3 a_{k_1}^+ a_{-k_2} a_{-k_3} a_{-k_4}) \delta_{k_1 + k_2 + k_3 + k_4, 0}. \quad (2.17)$$

Here γ , μ_1 , μ_2 , and μ_3 are angular and wavenumber-dependent functions given by

$$\gamma = \frac{3}{8} \sqrt{2S} g^2 \mu_B^2 \sin(2\theta), \quad (2.18)$$

$$\begin{aligned} \mu_1(k_1, k_2, k_3, k_4) &= \frac{1}{4} [J(k_1) + J(-k_2) + J(k_3) + J(-k_4) - 4J(k_1 + k_3)] \\ &+ \frac{1}{16} g^2 \mu_B^2 (2 - 3\sin^2 \theta) [D^{z,z}(k_1) + D^{z,z}(-k_2) + D^{z,z}(k_3) + D^{z,z}(-k_4) + 8D^{z,z}(k_1 + k_3)] \end{aligned}$$

$$\mu_2(k_1, k_3) = \frac{3}{16} g^2 \mu_B^2 \sin^2 \theta (D^{z,z}(k_1) + D^{z,z}(-k_3)),$$

$$\mu_3(k_2, k_4) = \frac{3}{16} g^2 \mu_B^2 \sin^2 \theta (D^{z,z}(k_2) + D^{z,z}(-k_4)). \quad (2.19)$$

2.3 Linear spin waves and the Bogoliubov transformation

In order to find the linear SW dispersion relation of the system the second-order Hamiltonian in the wavenumber-space representation must be diagonalized. This can be

done by applying the so-called Bogoliubov transformation [5, 17]:

$$\begin{aligned} a_k^+ &= s_k \alpha_k^+ + t_k \alpha_{-k}, \\ a_k &= s_k \alpha_k + t_k \alpha_{-k}^+. \end{aligned} \quad (2.20)$$

With this transformation the Hamiltonian can be expressed in terms of a new set of boson operators α_k^+ and α_k . The transformation is done by first substituting Eq. (2.20) into the second-order Hamiltonian, Eq. (2.14), which leads to a new expression with operator products like $\alpha_k^+ \alpha_k$, $\alpha_{-k} \alpha_k$, and $\alpha_k^+ \alpha_{-k}^+$. Then, if the coefficients s_k and t_k can be chosen such that the terms $\alpha_{-k} \alpha_k$ and $\alpha_k^+ \alpha_{-k}^+$ vanish, the transformed Hamiltonian will be in “quasi-particle” form (i.e., with operators only in the combination $\alpha_k^+ \alpha_k$). Utilizing the commutation relations stated in Eq. (2.5) for the original boson operators and the analogous commutation relations

$$[\alpha_k, \alpha_k^+] = \delta_{k,k'}, \quad [\alpha_k, \alpha_{k'}] = [\alpha_k^+, \alpha_{k'}^+] = 0 \quad (2.21)$$

for the new boson operators, it is first found that the scalar functions s_k and t_k satisfy

$s_k^2 - t_k^2 = 1$, and so they can be re-expressed as

$$s_k = \cosh \phi_k, \quad t_k = \sinh \phi_k. \quad (2.22)$$

Next, ϕ_k is deduced by setting the coefficients of the terms $\alpha_{-k} \alpha_k$ and $\alpha_k^+ \alpha_{-k}^+$ to zero, as mentioned above. This leads to the relation

$$\tanh(2\phi_k) = -Y(k)/X(k). \quad (2.23)$$

Using Eqs. (2.22) and (2.23) we can express the scalar functions as

$$s_k = \frac{1}{\sqrt{2}} \left[\frac{X(k)}{\sqrt{X^2(k) - Y^2(k)}} + 1 \right]^{1/2}, \quad t_k = \varepsilon \frac{1}{\sqrt{2}} \left[\frac{X(k)}{\sqrt{X^2(k) - Y^2(k)}} - 1 \right]^{1/2}, \quad (2.24)$$

where $X(k)$ and $Y(k)$ were defined in Eq. (2.15), while $\varepsilon = 1$ if $Y(k)/X(k) < 0$ and $\varepsilon = -1$ if $Y(k)/X(k) > 0$.

Using Eqs. (2.20) and (2.24) it can be shown that the second-order Hamiltonian in quasi-particle form is

$$H^{(2)} = \sum_k E_k \alpha_k^+ \alpha_k + U_0, \quad (2.25)$$

where the coefficient E_k of the $\alpha_k^+ \alpha_k$ term is just the linear SW dispersion relation:

$$E_k = \sqrt{X^2(k) - Y^2(k)}. \quad (2.26)$$

The additional term U_0 in Eq. (2.25) is the zero-point energy of the linear SWs and gives an additional contribution to the zeroth-order Hamiltonian. The expression for U_0 is

$$U_0 = \frac{1}{2} \sum_k \left[\sqrt{X^2(k) - Y^2(k)} - X(k) \right]. \quad (2.27)$$

2.4 The three-magnon and four-magnon interaction terms

In order to find the interaction potential for the three-magnon and four-magnon processes, the third-order and fourth-order Hamiltonians must also be transformed by re-expressing them in terms of α_k^+ and α_k operators. Following the same procedure as above, the interaction Hamiltonians are obtained by substituting Eq. (2.20) into Eqs. (2.16) and (2.17).

After some straightforward but lengthy algebra, it is found that the third-order Hamiltonian is

$$H^{(3)} = \frac{1}{2\sqrt{N}} \sum_{k_1, k_2, k_3} \left[V_1 \alpha_{k_1}^+ \alpha_{k_2}^+ \alpha_{-k_3} + V_2 \alpha_{k_1}^+ \alpha_{-k_2} \alpha_{-k_3} \right. \\ \left. + V_3 \alpha_{k_1}^+ \alpha_{k_2}^+ \alpha_{k_3}^+ + V_4 \alpha_{-k_1} \alpha_{-k_2} \alpha_{-k_3} \right] \delta_{k_1+k_2+k_3, 0}, \quad (2.28)$$

where

$$\begin{aligned}
V_1(k_1, k_2, k_3) &= i\gamma \left\{ \left[D^{z,z}(k_1) + D^{z,z}(-k_2) \right] s_{k_1} s_{k_2} s_{-k_3} + \left[D^{z,z}(k_1) + D^{z,z}(-k_3) \right] s_{k_1} t_{k_3} t_{-k_2} \right. \\
&+ \left. \left[D^{z,z}(k_3) + D^{z,z}(-k_2) \right] t_{k_3} s_{k_2} t_{-k_1} - \left[D^{z,z}(k_3) + D^{z,z}(-k_2) \right] s_{k_1} s_{-k_3} t_{-k_2} \right. \\
&- \left. \left[D^{z,z}(k_2) + D^{z,z}(-k_3) \right] s_{k_1} t_{-k_2} s_{-k_3} - \left[D^{z,z}(k_2) + D^{z,z}(-k_1) \right] t_{k_3} t_{-k_2} t_{-k_1} \right\}, \\
V_2(k_1, k_2, k_3) &= i\gamma \left\{ \left[D^{z,z}(k_2) + D^{z,z}(-k_1) \right] t_{k_2} s_{k_1} s_{-k_3} + \left[D^{z,z}(k_1) + D^{z,z}(-k_2) \right] s_{k_1} t_{k_2} s_{-k_3} \right. \\
&+ \left. \left[D^{z,z}(k_3) + D^{z,z}(-k_2) \right] t_{k_3} t_{k_2} t_{-k_1} - \left[D^{z,z}(k_2) + D^{z,z}(-k_1) \right] t_{k_3} s_{-k_2} t_{-k_1} \right. \\
&- \left. \left[D^{z,z}(k_1) + D^{z,z}(-k_3) \right] t_{k_2} t_{-k_1} s_{-k_3} - \left[D^{z,z}(k_2) + D^{z,z}(-k_3) \right] s_{k_1} s_{-k_2} s_{-k_3} \right\}, \\
V_3(k_1, k_2, k_3) &= i\gamma \left\{ \left[D^{z,z}(k_1) + D^{z,z}(-k_2) \right] s_{k_1} s_{k_2} t_{-k_3} - \left[D^{z,z}(k_2) + D^{z,z}(-k_3) \right] s_{k_1} t_{-k_2} t_{-k_3} \right\}, \\
V_4(k_1, k_2, k_3) &= i\gamma \left\{ \left[D^{z,z}(k_1) + D^{z,z}(-k_2) \right] t_{k_1} t_{k_2} s_{-k_3} - \left[D^{z,z}(k_2) + D^{z,z}(-k_3) \right] t_{k_1} s_{-k_2} s_{-k_3} \right\}. \quad (2.29)
\end{aligned}$$

The scalar functions s_k and t_k are defined in Eq. (2.24) and the angular-dependent coefficient γ is defined in Eq. (2.18).

Similarly the general form of the fourth-order Hamiltonian is given by

$$\begin{aligned}
H^{(4)} &= \frac{1}{2N} \sum_{k_1, k_2, k_3, k_4} \left\{ \Lambda_1 \alpha_{k_1}^+ \alpha_{k_2}^+ \alpha_{-k_3} \alpha_{-k_4} + \Lambda_2 \alpha_{k_1}^+ \alpha_{-k_2} \alpha_{-k_3} \alpha_{-k_4} + \Lambda_3 \alpha_{k_1}^+ \alpha_{k_2}^+ \alpha_{k_3}^+ \alpha_{-k_4} \right. \\
&+ \left. \Lambda_4 \alpha_{k_1}^+ \alpha_{k_2}^+ \alpha_{k_3}^+ \alpha_{k_4}^+ + \Lambda_5 \alpha_{-k_1} \alpha_{-k_2} \alpha_{-k_3} \alpha_{-k_4} \right\} \delta_{k_1+k_2+k_3+k_4, 0}, \quad (2.30)
\end{aligned}$$

where the weighting factors Λ_p ($p = 1, 2, 3, 4, 5$) are stated in Appendix A. In the special case of a longitudinal applied field (implying $\theta = 0$), the third order Hamiltonian $H^{(3)}$ vanishes since the term γ in Eq. (2.18) becomes identically zero, and the fourth order Hamiltonian $H^{(4)}$ reduces significantly since

$$\begin{aligned}
\Lambda_1(k_1, k_2, k_3, k_4) &= \frac{1}{4} \left[J(k_1) + J(-k_2) + J(k_3) + J(-k_4) - 4J(k_1 + k_3) \right] \\
&+ \frac{1}{8} g^2 \mu_B^2 \left[D^{z,z}(k_1) + D^{z,z}(-k_2) + D^{z,z}(k_3) + D^{z,z}(-k_4) + 8D^{z,z}(k_1 + k_3) \right], \quad (2.31)
\end{aligned}$$

while the other weighting factors $\Lambda_2 = \Lambda_3 = \Lambda_4 = \Lambda_5 = 0$.

In the following chapter there will be an in-depth discussion of the SW interaction effects found by applying a perturbation approach (in terms of Feynman diagrams) to the third-order and fourth-order Hamiltonian stated in Eqs. (2.28) and (2.30).

CHAPTER 3

The Diagrammatic Perturbation Formalism

In Chapter 1 the basic concepts of SWs were introduced by two methods, one semi-classical and one quantum-mechanical. In both cases a linearizing approximation was employed, and so the SW interactions (nonlinearities) were ignored. However, since the focus of this thesis is on the nonlinear properties of the SWs, a perturbation method must be adopted so that these properties can be systematically studied. In this chapter we will lay down the foundation for the perturbation formalism, based on boson operators, that allows us to use the nonlinear Hamiltonians $H^{(3)}$ and $H^{(4)}$ derived in Chapter 2 to deduce expressions for the SW energy shift and damping.

The standard diagrammatic perturbation formalism, as applied to bosons, interacting through a scalar pairwise interaction potential, is described in numerous text books on the many body theory of condensed matter systems (see, e.g., [13, 31, 32, 33, 34, 35]). Typically a Hamiltonian of the form $H = H_0 + H_1$ is considered, where H_0 is the non-interacting Hamiltonian given by

$$H_0 = \sum_k E_k \alpha_k^+ \alpha_k, \quad (3.1)$$

and E_k is the unperturbed energy of the bosons at wavenumber k . The interaction Hamiltonian H_1 is

$$H_1 = \frac{1}{2} \sum_{k_1, k_2, q} v(q) \alpha_{k_1}^+ \alpha_{k_2}^+ \alpha_{k_2+q} \alpha_{k_1-q}, \quad (3.2)$$

where $v(q)$ is the wavenumber Fourier transform of the pairwise interaction potential that

depends on the particle positions, and the $1/2$ avoids double counting. Comparing the above with the Hamiltonian in Eq. (2.10) for our nanowire system, we see that $H^{(2)}$ has the same form as the unperturbed Hamiltonian H_0 , but there are no terms analogous to the $H^{(3)}$ Hamiltonian. Also the $H^{(4)}$ Hamiltonian involves a more complicated interaction than the potential $v(q)$ in Eq. (3.2), plus there are additional terms. The constant term $H^{(0)}$ in Chapter 2 is unimportant for the dynamical properties of SWs.

In the next section we outline the standard diagrammatic perturbation formalism as applied to bosons. Then a generalization of this formalism is made so that it can be applied to the nanowire system, i.e., to include the more complicated diagram vertices due to the $H^{(3)}$ and $H^{(4)}$ terms following [19] for thin films.

3.1 Outline of standard diagrammatic perturbation theory

In order to relate the full Hamiltonian H to the unperturbed Hamiltonian H_0 , we define the so-called S -matrix operator [32, 33, 35] such that

$$e^{-\beta H} = e^{-\beta H_0} S(\beta), \quad (3.3)$$

where $\beta = 1/k_B T$. It is known that the mathematical solution for $S(\beta)$ can be expanded in integral form [32, 35] as

$$S(\beta) = 1 + \sum_{n=1}^{\infty} \frac{(-1)^n}{n!} \int_0^\beta d\tau_1 \int_0^\beta d\tau_2 \dots \int_0^\beta d\tau_n \hat{T}_w \{H_1(\tau_1)H_1(\tau_2)\dots H_1(\tau_n)\}, \quad (3.4)$$

where each $H_1(\tau) = e^{\tau H_0} H_1 e^{-\tau H_0}$, operator \hat{T}_w rearranges a product of terms such that the τ labels decrease from left to right, and n is the order of any expansion term. Next we recall the definition of thermal average given in Eq. (1.7) and introduce the notations

$Q_0 = \text{Tr}(e^{-\beta H_0})$ and $Q = \text{Tr}(e^{-\beta H})$ as the partition functions for the unperturbed and the full systems, respectively. Denoting an unperturbed thermal average by $\langle \dots \rangle_0$, it can be proved that

$$\frac{Q}{Q_0} = \langle S(\beta) \rangle_0 = 1 + \sum_{n=1}^{\infty} \frac{(-1)^n}{n!} \int_0^\beta d\tau_1 \int_0^\beta d\tau_2 \dots \int_0^\beta d\tau_n \langle \hat{T}_W \{H_1(\tau_1)H_1(\tau_2)\dots H_1(\tau_n)\} \rangle_0. \quad (3.5)$$

Determining the full partition function therefore involves the evaluation of the unperturbed thermal average within the above integral. Since H_1 contains an even number of operators, the expressions to be evaluated are

$$\langle \hat{T}_W \{b_1 b_2 b_3 \dots b_m\} \rangle_0, \quad (3.6)$$

where b_i denotes either a creation or annihilation operator, and integer m is *even*. This can be accomplished by the use of Wick's theorem, which expresses the unperturbed thermal average of any product of an even number of creation and annihilation operators in terms of a sum of products of thermal averages over *pairs* of operators [32, 36]. As an example, we consider a set of four operators b_1, b_2, b_3 , and b_4 . Wick's theorem allows the τ -ordered thermal average of the four operators to be re-expressed as

$$\langle \hat{T}_W b_1 b_2 b_3 b_4 \rangle_0 = \langle \hat{T}_W b_1 b_2 \rangle_0 \langle \hat{T}_W b_3 b_4 \rangle_0 + \langle \hat{T}_W b_1 b_3 \rangle_0 \langle \hat{T}_W b_2 b_4 \rangle_0 + \langle \hat{T}_W b_1 b_4 \rangle_0 \langle \hat{T}_W b_2 b_3 \rangle_0. \quad (3.7)$$

This theorem opens the way for the use of a Green's function formalism. It can be shown that the only non-zero results for any term $\langle \hat{T}_W b_1 b_2 \rangle_0$ involve the operators $\alpha_k(\tau_1)$ and $\alpha_k^+(\tau_2)$, or vice-versa [35]. The causal Green's function [31] for the unperturbed system is conventionally defined as

$$G_k^0(\tau_1 - \tau_2) = -i \langle \hat{T}_W \alpha_k(\tau_1) \alpha_k^+(\tau_2) \rangle_0, \quad (3.8)$$

where $\alpha_k(\tau) = e^{H_0\tau} \alpha_k e^{-H_0\tau}$. The results are found to be

$$G_k^0(\tau_1 - \tau_2) = \begin{cases} \langle \alpha_k \alpha_k^+ \rangle_0 e^{E_k(\tau_2 - \tau_1)} = (1 + n_k^0) e^{E_k(\tau_2 - \tau_1)} & \tau_1 > \tau_2 \\ \langle \alpha_k^+ \alpha_k \rangle_0 e^{E_k(\tau_2 - \tau_1)} = n_k^0 e^{E_k(\tau_2 - \tau_1)} & \tau_1 < \tau_2 \end{cases}, \quad (3.9)$$

where n_k^0 is the usual unperturbed Bose-Einstein distribution function [37]:

$$n_k^0 = \frac{1}{\exp(\beta E_k) - 1}. \quad (3.10)$$

3.1.1 Diagrammatic representation

Rather than proceeding algebraically (which is tedious), it is convenient to relate the Green's function formalism to a diagrammatic representation, which keeps track of all the products that come about when applying Wick's theorem. Referring to Eq. (3.2) the terms of the interaction Hamiltonian can be represented as in Fig. 3.1. The interaction vertex $v(q)$ is drawn as a broken line carrying the wavenumber label q and the τ label. Each solid line represents a creation or annihilation operator depending on whether the arrow begins or ends at the interaction vertex, respectively. In order to relate these diagrams to the above formalism the solid lines must be connected in all possible ways, consistent with the direction of arrows and wavenumber conservation. For the simplest case of a diagram with just one interaction vertex there are two possibilities, as shown in Fig. 3.2. In n^{th} order of perturbation there will be n vertices, and the lines must be connected in all possible ways, giving a set of Feynman diagrams [32, 35].

The correspondence between Wick's theorem and the diagrams in Fig. 3.2 can be illustrated by considering Eq. (3.7) when applied specifically to the terms of the interaction Hamiltonian Eq. (3.2) in first order:

$$\begin{aligned} \langle \widehat{T}_W v(q) \alpha_{k_1}^+ \alpha_{k_2}^+ \alpha_{k_2+q} \alpha_{k_1-q} \rangle_0 &= v(q) \langle \widehat{T}_W \alpha_{k_1}^+ \alpha_{k_2}^+ \rangle_0 \langle \widehat{T}_W \alpha_{k_2+q} \alpha_{k_1-q} \rangle_0 \\ &+ v(q) \langle \widehat{T}_W \alpha_{k_1}^+ \alpha_{k_2+q} \rangle_0 \langle \widehat{T}_W \alpha_{k_2}^+ \alpha_{k_1-q} \rangle_0 + v(q) \langle \widehat{T}_W \alpha_{k_1}^+ \alpha_{k_1-q} \rangle_0 \langle \widehat{T}_W \alpha_{k_2}^+ \alpha_{k_2+q} \rangle_0 \end{aligned} \quad (3.11)$$

The first term involves averages $\langle \widehat{T}_W \alpha_{k_1}^+ \alpha_{k_2}^+ \rangle_0$ and $\langle \widehat{T}_W \alpha_{k_2+q} \alpha_{k_1-q} \rangle_0$ that are identically zero, while the other two terms of the form $\langle \widehat{T}_W \alpha_{k_1}^+ \alpha_{k_2} \rangle_0$ are just the causal Green's function, which can be represented as the solid lines in Fig. 3.2.

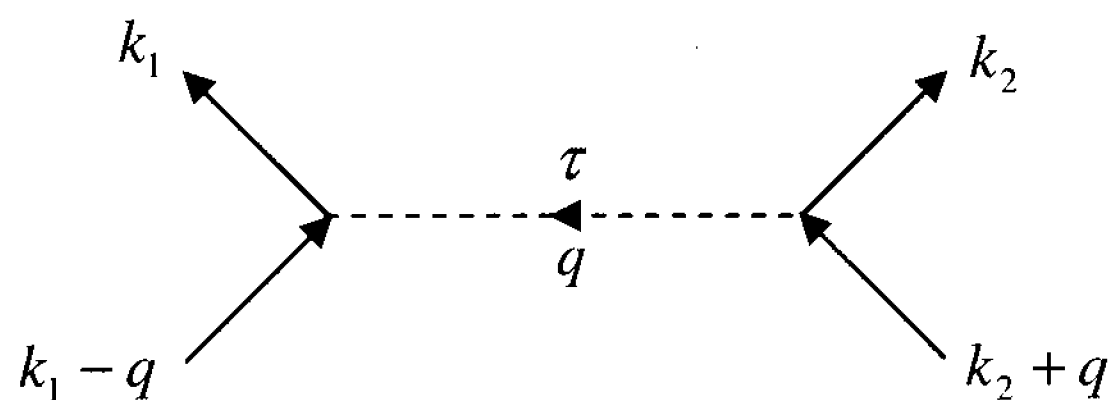


Fig. 3.1: An interaction vertex $v(q)$ represented by the dashed line, carrying wavenumber q and the label τ .

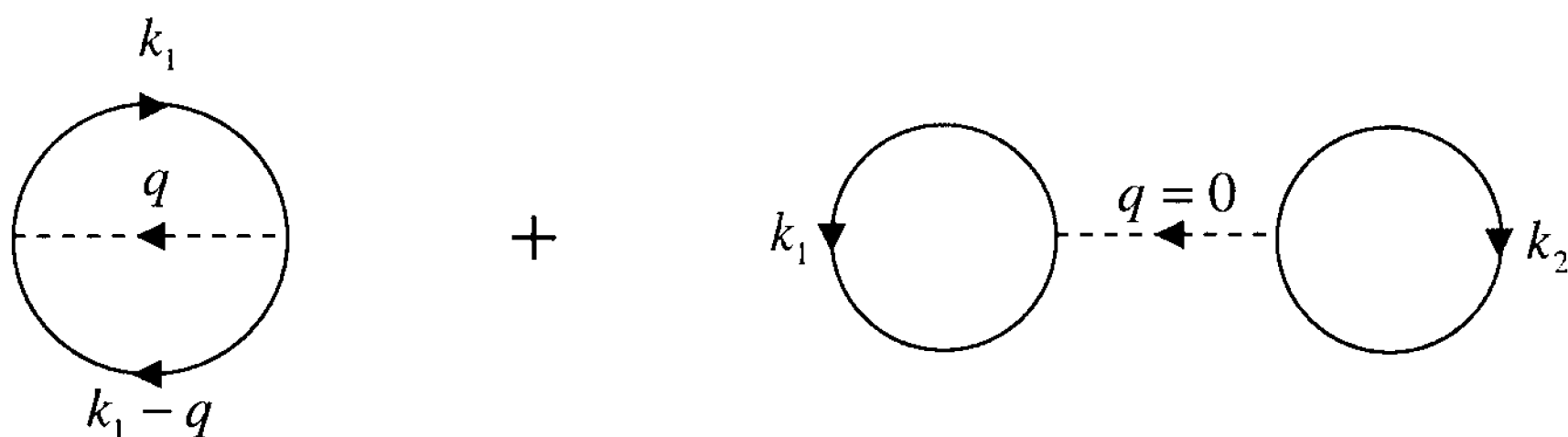


Fig 3.2: The two first order diagrams with no external lines.

There are two simplifications to mention briefly in the diagrammatic formalism. First, from Eq. (3.5) and Wick's theorem it follows that Q/Q_0 is obtained by summing over *all* distinct diagrams with no external lines. Here *all* covers linked and unlinked diagrams, and we illustrate this distinction for second order ($n = 2$). By connecting the solid lines in all possible ways two classes of diagrams are found, as illustrated by particular examples in Fig. 3.3. By detailed counting arguments based on the number of possible terms from Wick's theorem that give either linked or unlinked diagrams and

using permutation theory, it can be proven [31, 35] that

$$\ln\left(\frac{Q}{Q_0}\right) = \sum [\text{All distinct linked diagrams with no external lines}]. \quad (3.12)$$

This is known as the “Linked Cluster Theorem”, and it means that we need to use only the subset of diagrams that are linked. Second, we recall that the terms in Eq. (3.5) involve an integration over each of the τ labels from 0 to β . This step can be simplified by transforming the Green's function from a representation in terms of τ labels to a “frequency” representation $G^0(k, i\omega_m)$. Starting with Eq. (3.9) and applying the contour integration method [38] it can be shown that

$$G_k^0(\tau) = \sum_m G^0(k, i\omega_m) \exp(-i\omega_m \tau) = -\frac{1}{\beta} \sum_m \frac{\exp(-i\omega_m \tau)}{i\omega_m - E_k}, \quad (3.13)$$

where $i\omega_m = 2\pi mi / \beta$, with integer m ranging from $-\infty$ to $+\infty$, is an imaginary frequency label that is related to the complex poles of the Bose-Einstein function. It is then found that the required integration over any τ simply leads to a factor of $\beta \delta_{\omega_{m_1} + \omega_{m_2}, \omega_{m_3} + \omega_{m_4}}$, which translates to the “conservation of frequency” at each vertex.



Fig 3.3: Examples of second order diagrams with no external lines that are (a) linked and (b) unlinked (i.e., that separate into parts).

3.1.2 The interacting Green's function

By analogy with Eq. (3.8) for the non-interacting case, the Green's function for the full (interacting) system is defined by

$$G_k(\tau_1 - \tau_2) = -i \langle \hat{T}_W \bar{\alpha}_k(\tau_1) \bar{\alpha}_k^+(\tau_2) \rangle, \quad (3.14)$$

where the averages and all other quantities are taken with respect to the full Hamiltonian. For example $\bar{\alpha}_k(\tau) = e^{H\tau} \alpha_k e^{-H\tau}$. Using the definitions of thermal average Eq. (1.7) and the expansion in Eq. (3.4) it can be shown that [13]

$$G_k(\tau_1 - \tau_2) = \frac{\langle \hat{T}_W \alpha_k(\tau_1) \alpha_k^+(\tau_2) S(\beta) \rangle_0}{\langle S(\beta) \rangle_0}. \quad (3.15)$$

The numerator and denominator on the right-hand side involve thermal averages of the form $\langle \hat{T}_W \{b_1 b_2 b_3 \dots b_m\} \rangle_0$ with respect to the unperturbed Hamiltonian. Hence Wick's theorem and a diagrammatic representation can again be employed. The main distinction here arises because the numerator of Eq. (3.15) has an extra operator α_k^+ and an extra operator α_k . These correspond to having two *external* lines in the diagrams, one that does not begin at a vertex and one that does not end at a vertex, as depicted in Fig. 3.4, where the shaded region is usually called a "self energy". A *proper* self energy diagram is one that cannot be broken into separate parts by breaking any one of its internal Green's function lines. We illustrate this point using Fig. 3.5(a), which can be broken to form two new diagrams. However, the diagram in Fig. 3.5(b) cannot be broken in this manner. Thus Fig. 3.5(a) is not a proper self energy diagram, while Fig. 3.5(b) is.

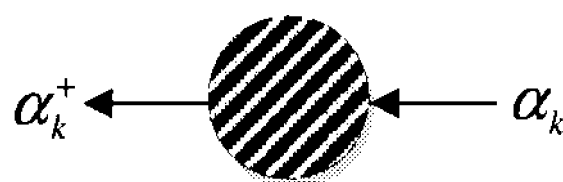


Fig. 3.4: Diagrammatic representation of a Green's function. The shaded region represents any allowed diagrammatic structure of lines and interaction vertices.

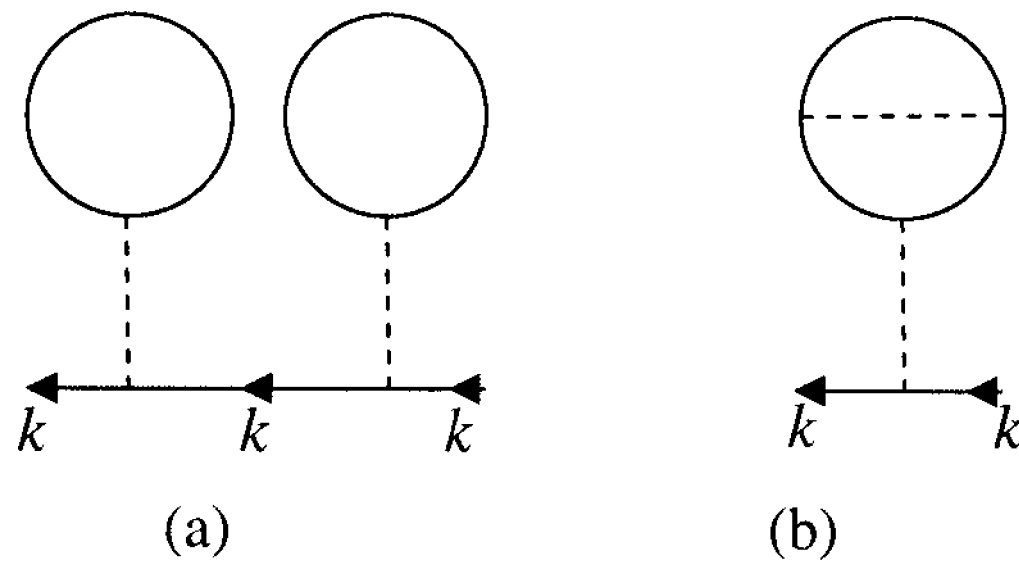


Fig. 3.5: (a) A diagrammatic structure that is not a proper self energy diagram. (b) An example of a proper self energy diagram.

Another form of the Linked Cluster Theorem can be established for the interacting Green's function, with the effect that the denominator in Eq. (3.15) is eliminated when only linked diagrams are counted. The formal result becomes

$$G_k(\tau_1 - \tau_2) = \sum [\text{All distinct } \textit{linked} \text{ diagrams with two external lines}]. \quad (3.16)$$

The interacting Green's function can be related to the non-interacting Green's function by utilizing the above concept of proper self energy. Consider the diagrammatic series illustrated in Fig. 3.6, where the interacting and non-interacting Green's functions are represented by a heavy arrowed line G and a light arrowed line G^0 , respectively. The shaded region Σ is the sum of all proper self energy contributions for a chosen interaction order. This diagrammatic series can be re-formulated as a geometric series in terms of a so-called Dyson's equation [13]:

$$G(k, i\omega_m) = G^0(k, i\omega_m) + G^0(k, i\omega_m) \Sigma(k, i\omega_m) G(k, i\omega_m), \quad (3.17)$$

where we are again using the "frequency" representation. Then, using Eq. (3.13), the interacting Green's function is obtained as

$$G(k, i\omega_m) = \left(-\frac{1}{\beta} \right) \frac{1}{i\omega_m - E_k + (1/\beta)\Sigma(k, i\omega_m)}. \quad (3.18)$$

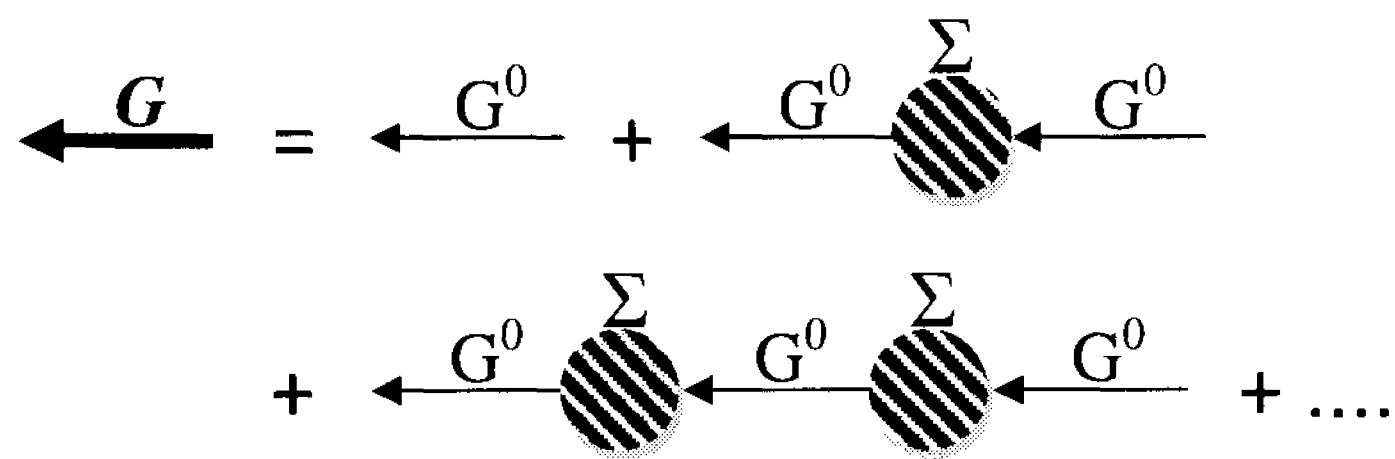


Fig. 3.6: A series of diagrams for the interacting Green's function in terms of the non-interacting Green's function and proper self energy Σ .

To study the boson excitations of the system, we are interested in the poles of Eq. (3.18), i.e., in the (complex) frequencies ω at which the denominator vanishes. In the non-interacting case, Eq. (3.13), this is simply E_k . For weakly interacting systems the new pole for ω will still be close to the unperturbed value E_k and so, to a first approximation, the proper self energy in Eq. (3.18) can be replaced by its value $\Sigma(k, E_k)$ at frequency E_k . In general, the proper self energy is complex, so we write

$$\Sigma(k, E_k) = \Lambda(k, E_k) + i\Phi(k, E_k). \quad (3.19)$$

The pole of the interacting Green's function occurs approximately at

$$\omega - E_k + (1/\beta)\Lambda(k, E_k) + i(1/\beta)\Phi(k, E_k) = 0, \quad (3.20)$$

where $i\omega_m$ has been replaced by a complex frequency label $\omega = \omega' - i\omega''$ (a process referred to as analytic continuation [33]). This gives for the real part

$$\omega' = E_k - (1/\beta)\Lambda(k, E_k), \quad (3.21)$$

which is the modified (or renormalized) boson energy, and for the imaginary part

$$\omega'' = (1/\beta)\Phi(k, E_k), \quad (3.22)$$

which corresponds to the damping (i.e., the reciprocal lifetime) of the bosons. Later we will need to specify more carefully how the real and imaginary parts are taken.

Finally, we summarize the diagrammatic rules for the proper self energy [13, 32, 35]. Draw all topologically distinct linked diagrams of a chosen order with one external line labelled $(k, i\omega_m)$ entering and another external line $(k, i\omega_m)$ leaving. Then calculate the contribution of each diagram as specified below.

1. Label the diagrams so that wavenumber and “frequency” are conserved at each vertex.
2. Associate a factor $\beta v(q)/2$ with each vertex, where q is its wavenumber.
3. For each Green’s function line associate a factor $G^0(k, i\omega_m)$, where k and $i\omega_m$ are the wavenumber and frequency along the line, respectively.
4. Include a factor $(-1)^n$, where n is the number of vertices, as well as any symmetry factor (due to Wick’s theorem).
5. Sum over all internal wavenumber and frequency labels within the restrictions of rule 1. The fixed external labels $(k, i\omega_m)$ are not summed over.

Extra convergence factors need to be included if any line is “self-contracting” (i.e., if it begins and ends on the same vertex).

3.2 Extension of the diagrammatic method to the magnetic nanowire

The formalism in Section 3.1 will now be modified so that it can be applied to the model of a magnetic nanowire described in Chapter 2. This will be done separately for

the three-magnon and four-magnon processes described by $H^{(3)}$ and $H^{(4)}$, respectively. Formal expressions for the renormalized energy and damping of the SW will be deduced following a similar approach to [19] for a magnetic film.

3.2.1 Proper self energy for the three-magnon interactions

We recall that the three-magnon interaction Hamiltonian in terms of α^+ and α operators is given by Eq. (2.28), so there are four types of interaction vertices, which can be represented diagrammatically as in Fig. 3.7. Here we choose to represent the interaction vertices by dots, since the vertices V_i are more complicated.

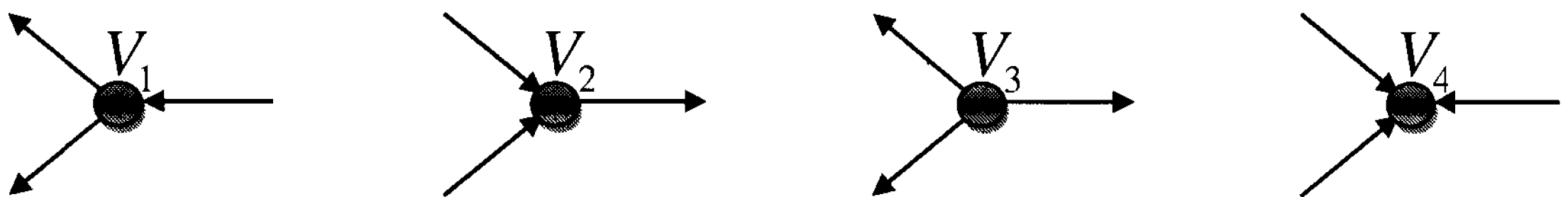


Fig. 3.7: The vertices of the 3rd order Hamiltonian represented diagrammatically. The dots represent the interaction vertices.

It might appear that a problem arises because these vertices involve three operators, whereas Wick's theorem (as discussed in Section 3.1) deals with products of an even number of operators. However, this is not an issue since we shall see that the three-magnon interaction vertices come in conjugate pairs in the diagrams, allowing us to apply Wick's theorem for each pair. For example the V_1 and V_2 vertices give products like $\langle \hat{T}_W \{ V_1 V_2 \alpha_{k_1}^+ \alpha_{-k_2}^+ \alpha_{k_3} \alpha_{k_1'}^+ \alpha_{k_2'} \alpha_{k_3'} \} \rangle_0$, which correspond to a second order diagram since two vertices are involved.

The task at hand is to first draw all topologically distinct linked diagrams with one

external line $(k, i\omega_m)$ entering and another external line $(k, i\omega_m)$ leaving. The leading order self energy diagrams can just be written down directly. Alternatively, in order to insure that all topologically distinct proper self energy diagrams are systematically included, a process that will be used here is to draw all such diagrams with no external lines and then imagine “breaking” the lines one at a time in all possible allowed ways to generate the corresponding proper self energy diagrams. It is easily seen that there are no allowable first-order diagrams, and so we consider $n = 2$ for which there are three closed diagrams as in Fig. 3.8. They involve either the conjugate V_1 and V_2 vertices or the V_3 and V_4 vertices. In each case there might be several permutations of connecting the lines in order to obtain each diagram. Each permutation is unique in the sense that it gives rise to a different set of conserved wavenumber and frequency labels.

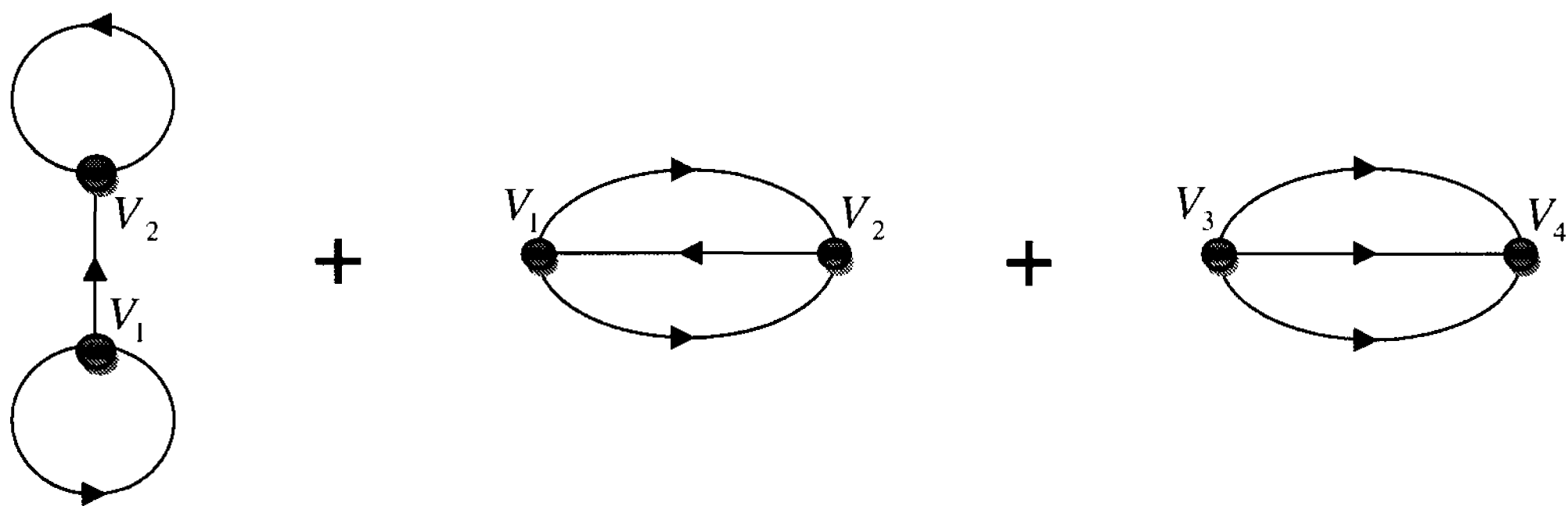


Fig. 3.8: All distinct linked diagrams with no external lines for each conjugate pair of vertices.

Through the process of breaking Green’s function lines, the first diagram in Fig. 3.8 leads to the proper self energy diagrams in Fig. 3.9. The labelling of the proper self energy diagrams insures that the external labels $(k, i\omega_m)$ are the same and that momentum and frequency are conserved. The second diagram in Fig. 3.8 can also be broken in two topologically distinct ways to generate the proper self energy diagrams in Fig. 3.10, while

the third diagram in Fig. 3.8 can be broken in one way to give the diagram in Fig. 3.11. Therefore we have five diagrams for the proper self energy in second order of perturbation.

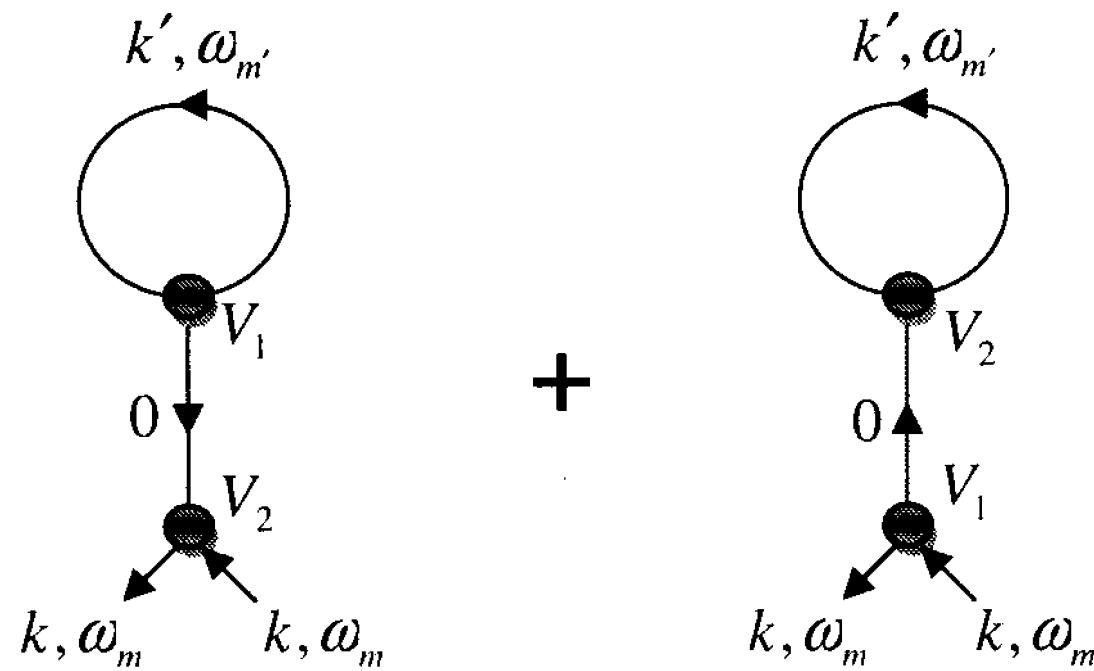


Fig. 3.9: Proper self energy diagrams corresponding to the first diagram in Fig. 3.8.

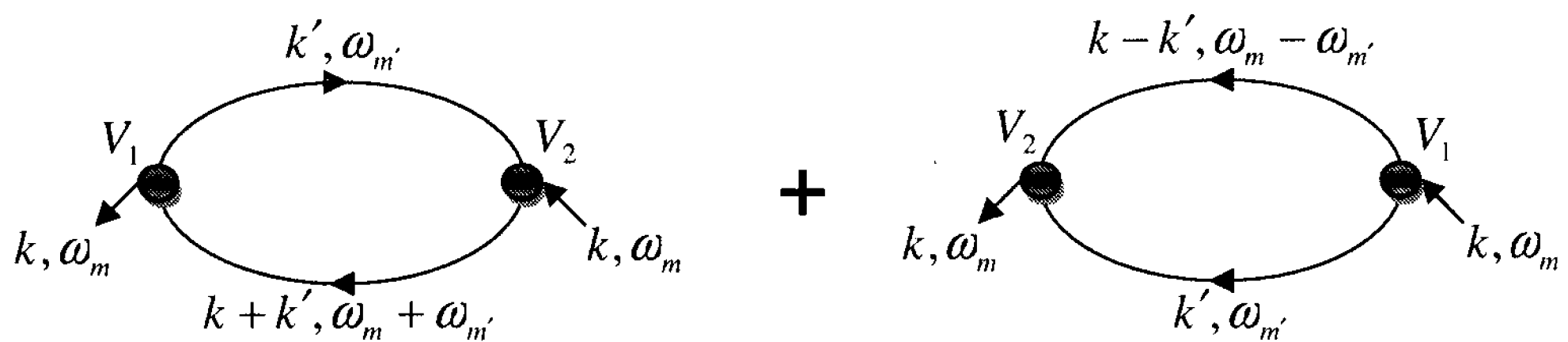


Fig. 3.10: Proper self energy diagrams corresponding to the second diagram in Fig. 3.8.

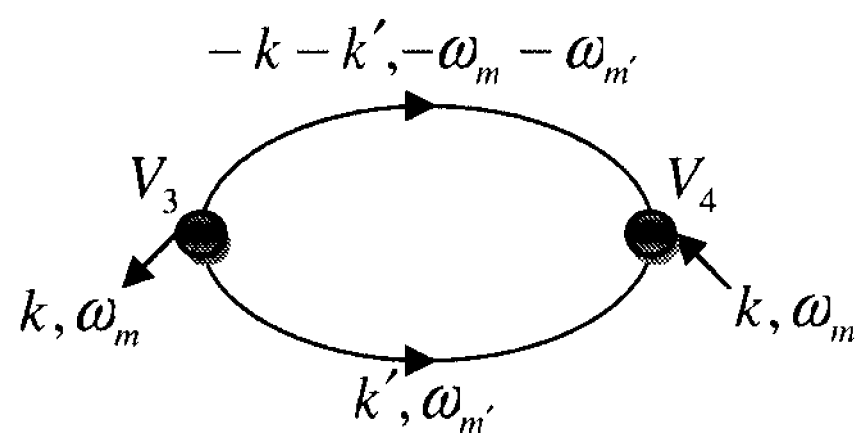


Fig.3.11: Proper self energy diagram corresponding to the third diagram in Fig. 3.8.

It is important to note a distinction between the standard diagrammatic formalism in Section 3.1 and the modified formalism for dealing with our magnetic system. In the standard formalism the interaction potential is pairwise, whereas the three-magnon interaction potentials V_i have a more complicated dependence on the wavenumber labels.

This modifies the symmetry properties of the proper self energy diagrams, because each permutation gives a different set of wavenumber labels in the interaction potential, even though the diagrams are topologically similar. This is discussed in Appendix B. Taking into account the symmetry factors and permutations of vertex labels, as well as combining the contribution for all five diagrams, the total proper self energy due to the three-magnon interaction process is eventually found to be

$$\begin{aligned} \Sigma(k, i\omega_m) = & -\frac{1}{N} \beta \sum_{k'} \left\{ (W_A + W_B) \frac{n^0(E_{k'})}{E_0} + W_C \frac{[n^0(E_{k'}) + n^0(E_{-k-k'}) + 1]}{E_{k'} + E_{-k-k'} + i\omega_m} \right. \\ & \left. + W_D \frac{[n^0(E_{k'}) + n^0(E_{k-k'}) + 1]}{E_{k-k'} + E_{k'} - i\omega_m} + W_E \frac{[n^0(E_{k'}) - n^0(E_{k+k'})]}{E_{k+k'} - E_{k'} - i\omega_m} \right\}, \end{aligned} \quad (3.23)$$

where

$$W_A = \frac{1}{4} [V_1(k', 0) + V_1(0, k')] [V_2(k, 0) + V_2(k, -k)]$$

$$W_B = \frac{1}{4} [V_1(k, 0) + V_1(0, k)] [V_2(k', 0) + V_2(k', -k')]$$

$$\begin{aligned} W_C = & \frac{1}{8} [V_3(k, k') + V_3(k, -k - k') + V_3(k', k) + V_3(k', -k - k') \\ & + V_3(-k - k', k) + V_3(-k - k', k')] \times [V_4(-k, -k') + V_4(-k, k + k') \\ & + V_4(-k', -k) + V_4(-k', k + k') + V_4(k + k', -k) + V_4(k + k', -k')] \end{aligned}$$

$$W_D = \frac{1}{8} [V_1(k', k - k') + V_1(k - k', k')] [V_2(k, k' - k) + V_2(k, -k')]$$

$$W_E = \frac{1}{4} [V_1(k, k') + V_1(k', k)] [V_2(k + k', -k) + V_2(k + k', -k')]. \quad (3.24)$$

We have simplified the notation for the V_i factors defined in Eq. (2.29) by dropping the third wavenumber label, which is redundant due to the Kronecker delta in Eq. (2.28).

Finally, to obtain the real and imaginary parts Λ and Φ of the self energy, we use

the mathematical identity given below [31]:

$$\frac{1}{x \pm i\eta} = P\left(\frac{1}{x}\right) \mp i\pi\delta(x). \quad (3.25)$$

Here x can be any real variable, η is an infinitesimal positive number ($\eta \rightarrow 0$), and P indicates that the principal part is taken in any summation over the real variable. The correct procedure for making the analytic continuation mentioned in Section 3.1 is to replace the frequency label in the self energy by $E_k - i\eta$. Thus from Eq. (3.21) the renormalized energy is $E_k + \Delta E_k$, where the energy shift ΔE_k becomes

$$\begin{aligned} \Delta E_k &\approx -\frac{1}{\beta} \text{Re}[\Sigma(k, E_k - i\eta)] \\ &= \frac{1}{N} \sum_{k'} \left\{ (W_A + W_B) \frac{n^0(E_{k'})}{E_0} + W_C \frac{[n^0(E_{k'}) + n^0(E_{-k-k'}) + 1]}{E_{k'} + E_{-k-k'} + E_k} \right. \\ &\quad \left. + W_D \frac{[n^0(E_{k'}) + n^0(E_{k-k'}) + 1]}{E_{k-k'} + E_{k'} - E_k} + W_E \frac{[n^0(E_{k'}) - n^0(E_{k+k'})]}{E_{k+k'} - E_{k'} - E_k} \right\}. \end{aligned} \quad (3.26)$$

Likewise, the damping Γ_k becomes

$$\begin{aligned} \Gamma_k &\approx -\frac{1}{\beta} \text{Im}[\Sigma(k, E_k - i\eta)] \\ &= -\frac{1}{N} \pi \sum_{k'} \left\{ W_D [n^0(E_{k'}) + n^0(E_{k-k'}) + 1] \delta(E_{k-k'} + E_{k'} - E_k) \right. \\ &\quad \left. + W_E [n^0(E_{k'}) - n^0(E_{k+k'})] \delta(E_{k+k'} - E_{k'} - E_k) \right\}. \end{aligned} \quad (3.27)$$

We note that there is no term proportional to $W_C \delta(E_{k'} + E_{-k-k'} + E_k)$ in Eq. (3.27) for the overall damping, because the delta function could never be satisfied. The two damping terms with weighting factors W_D and W_E are the analogs of the three-magnon “splitting” and “confluence” processes, respectively, that are known from studies of bulk magnetic

materials [17] and magnetic films [19]. Temperature-dependent effects are included in the results through the Bose-Einstein thermal factors in Eqs. (3.26) and (3.27). Note that the energy shift and damping can still occur in the $T \rightarrow 0$ limit (when all the Bose-Einstein factors are zero), as will be discussed in Chapter 4.

3.2.2 Proper self energy for the four-magnon interactions

We recall that the four-magnon interaction Hamiltonian is given by Eq. (2.30), which has five terms. The diagrammatic representations for the corresponding five vertices are as shown in Fig. 3.12.

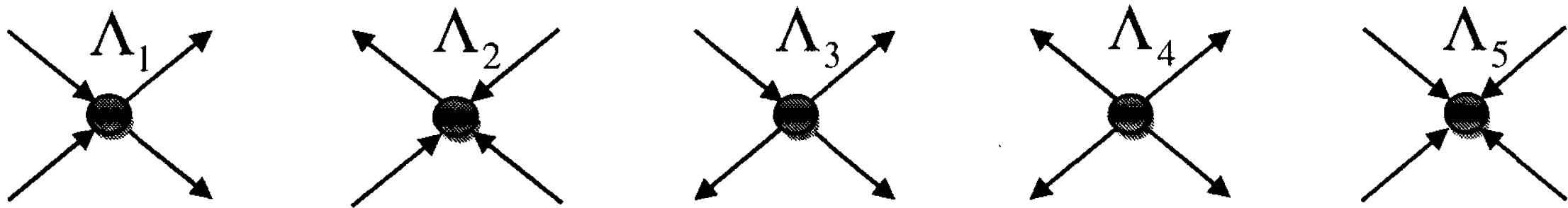


Fig. 3.12 Diagrammatic representation of the vertices for the four-magnon processes.

The first interaction term contains two creation and two annihilation operators, which can be connected to form the first order ($n = 1$) proper self energy diagram in Fig. 3.13. This diagram turns out to be real, so it gives the leading order contribution to the energy shift due to the four-magnon processes. The expression is

$$\Delta E_k = -\frac{1}{N} \sum_{k'} Z_A n^0(E_{k'}), \quad (3.28)$$

where

$$Z_A = \frac{1}{2} [\Lambda_1(k', k, -k)k + \Lambda_1(k', k, -k') + \Lambda_1(k, k', -k) + \Lambda_1(k, k', -k')]. \quad (3.29)$$

Note that we have omitted the fourth wavenumber label since it is redundant due to the Kronecker delta in Eq. (2.30).

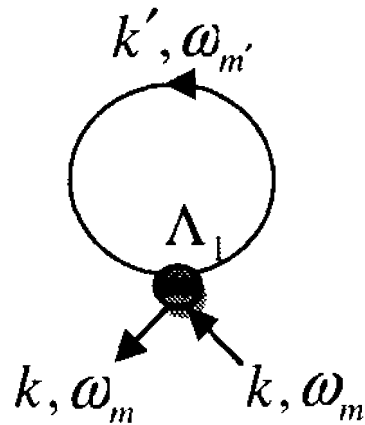


Fig. 3.13 First order proper self energy diagrams due to the Λ_1 vertex.

The other interaction terms have to be paired in order to create proper self energy diagrams, leading to contributions in higher order. We are interested here in the second order diagrams, since they are expected to provide the leading order contribution for the four-magnon damping. The conjugate Λ_2 and Λ_3 vertices can form the two distinct proper self energy diagrams shown in Fig. 3.14, but the conjugate Λ_4 and Λ_5 vertices do not lead to damping since the corresponding proper self energy for this pair of vertices gives rise to a delta function dependence that can never be satisfied. Furthermore, in order to include all leading order damping contributions, we must include the second order diagram involving a pair of Λ_1 vertices shown in Fig. 3.15. There are other second order proper self energy diagrams that can be written down, but these all turn out to be real (i.e., they do not describe damping processes).

It is found that the first diagram in Fig. 3.14 gives a contribution to the four-magnon damping proportional to $\delta(E_k - E_{k'} - E_{k''} - E_{k-k'-k''})$, which is analogous to the “splitting” process described in Subsection 3.2.1 for the three-magnon case. The second diagram in Fig. 3.14 gives a contribution proportional to $\delta(E_k + E_{k'} + E_{k'-k'-k} - E_{k'})$, which is analogous to the three-magnon “confluence” process. The damping contribution for the diagram in Fig. 3.15, which is proportional to $\delta(E_k + E_{k'} - E_{k''} - E_{k+k'-k''})$,

corresponds to a scattering of magnons and has no analog in the three-magnon case.

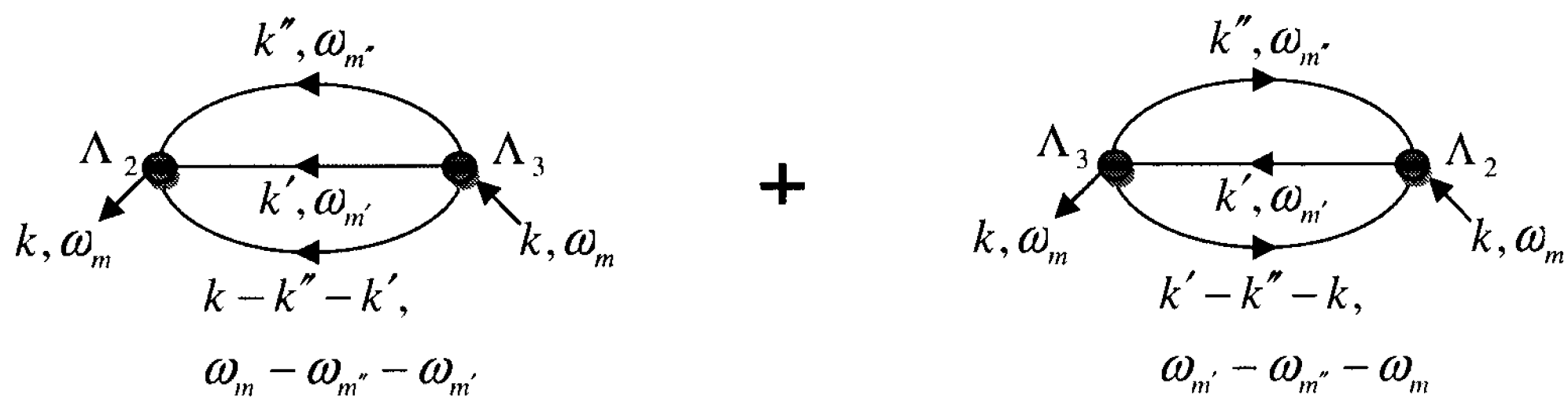


Fig. 3.14 Second order proper self energy diagrams due to the Λ_3 and Λ_2 vertices.

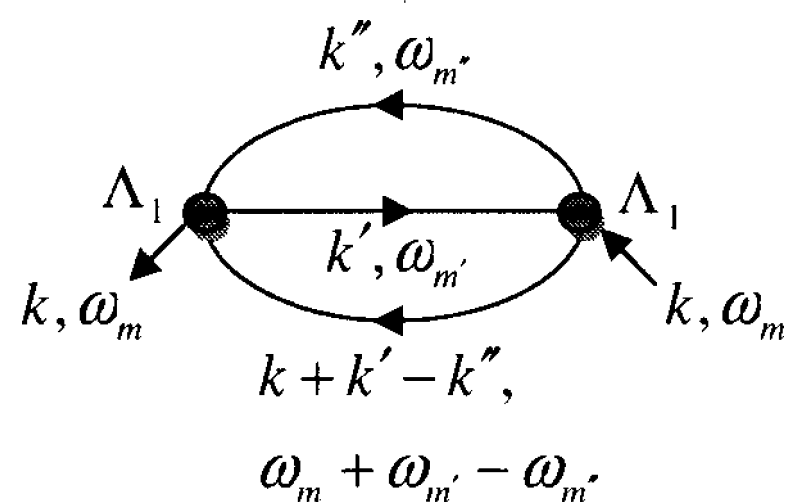


Fig. 3.15 Second order proper self energy diagram due to a pair of Λ_1 vertices.

In the next two chapters some numerical results will be discussed for the wire geometry. The focus of these applications will be mainly for the three-magnon interaction phenomena for various orientations of the external magnetic field.

CHAPTER 4

Results for Longitudinal and Transverse Applied Magnetic Field

In this and the following chapter the focus will be on obtaining numerical results for the linear SW energy E_k , the SW energy shift ΔE_k , and the SW damping Γ_k . For the damping, the emphasis will be on the three-magnon processes, since these will typically tend to be more important. We will also illustrate interesting effects that depend on the orientation of the applied magnetic field.

From Eq. (2.13) the relation between the canting angle θ of the spins and the orientation α of the applied magnetic field can be re-expressed as

$$\sin(2\theta) = 2(B_0 / B_C) \sin(\alpha - \theta), \quad (4.1)$$

where B_C is a characteristic field value defined by

$$B_C = -\frac{3}{2} Sg\mu_B D^{z,z}(0) > 0. \quad (4.2)$$

The ratio of B_0 to B_C , as well as the angle α , will prove to be important parameters for the SW behaviour. Two cases will be investigated in the present chapter. The first case is a longitudinal field along the symmetry axis of the wire (angle $\alpha = 0$), while the second and more interesting case is a field transverse to the wire axis ($\alpha = \pi/2$). The formalism for the general oblique angle α will be presented in the next chapter.

4.1 Longitudinal applied magnetic field

In the case of the longitudinal field it is clear that there will be no canting of the

spins, since the orientation of the field is parallel to the preferred direction of net magnetization. This significantly simplifies the linear and nonlinear SW properties, since we may put $\theta = \alpha = 0$ in the general expressions derived in Chapters 2 and 3.

4.1.1 Linear SW behaviour for a longitudinal field

From Eqs. (2.15) and (2.26) it is easy to show that the linear SW dispersion relation reduces to

$$E_k = S(J(0) - J(k)) + g\mu_B B_0 - \frac{1}{2} g^2 \mu_B^2 S (2D^{z,z}(0) + D^{z,z}(k)). \quad (4.3)$$

It follows that the energy $E_{k=0}$ at zero wavenumber depends on the dipole strength and the external field, but not on the exchange:

$$E_{k=0} = g\mu_B B_0 - \frac{3}{2} g^2 \mu_B^2 S D^{z,z}(0) = g\mu_B (B_0 + B_C). \quad (4.4)$$

Thus the energy gap at $k=0$ in the linear SW spectrum becomes larger as the dipolar effects and/or the external field B_0 are increased. To illustrate the k dependence given by Eq. (4.3) we proceed numerically. We choose spin quantum number $S=1$, and adopt units such that nearest-neighbour exchange constant $J=1$ and lattice constant $a=1$. Hence the SW energy E_k is in units of $SJ=1$. Additionally, we introduce the ratio $R_{DE} = g^2 \mu_B^2 / SJ a^3$ as a measure of the relative strength of the dipolar and exchange interactions. For a ferromagnetic metal (such as Ni) the order of magnitude for R_{DE} is ~ 0.1 . Finally for the magnitude of the applied field we introduce the dimensionless parameter $b = g\mu_B B_0 / SJ$, although in some cases it will be helpful to discuss the field dependence in terms of the ratio B_0 / B_C . Typically $b \ll 1$ for the values of B_0 used in

experimental techniques such as ferromagnetic resonance (FMR) and Brillouin light scattering (BLS). Next, in order to produce numerical plots we must consider how to evaluate the dipole sums. From Eq. (2.3) and the inverse of the wavenumber Fourier transform in Eq. (2.7) it follows that

$$D^{z,z}(k) = -\sum_j \left(2/|z_{i,j}|^3 \right) \exp[ik(z_i - z_j)], \quad (4.5)$$

where the notation is that of Subsection 2.2.2. This can be re-expressed explicitly as

$$D^{z,z}(k) = -\sum_{n=1}^{N'} \frac{2}{(na)^3} 2 \cos(nka), \quad (4.6)$$

where the integer n labels the spins above and below any given spin i , and the total number of spin $N = 2N' + 1 \rightarrow \infty$. The expression above can be easily summed numerically by choosing a sufficiently large finite N' to truncate the series. By trial we find that for good convergence it is sufficient to set $N' = 50000$.

Now that we have established the numerical procedure we consider first in Fig. 4.1 a set of linear SW dispersion curves for various R_{DE} and b values. We see that the curves shift up with increasing field which is evident from Eq. (4.4). For increasing R_{DE} the dispersion curves also shift up, but with the effect being more significant in the small wavenumber regime. This is to be expected on physical grounds since the dipole interactions are long-range.

4.1.2 SW renormalization for a longitudinal field

The formal expressions given in Chapter 3 for the SW renormalized energy and damping involve temperature dependences due to the Bose-Einstein factors as well as summations over one (or more) wavenumber labels. We need to discuss how these two

features can be taken into account for the numerical calculations.

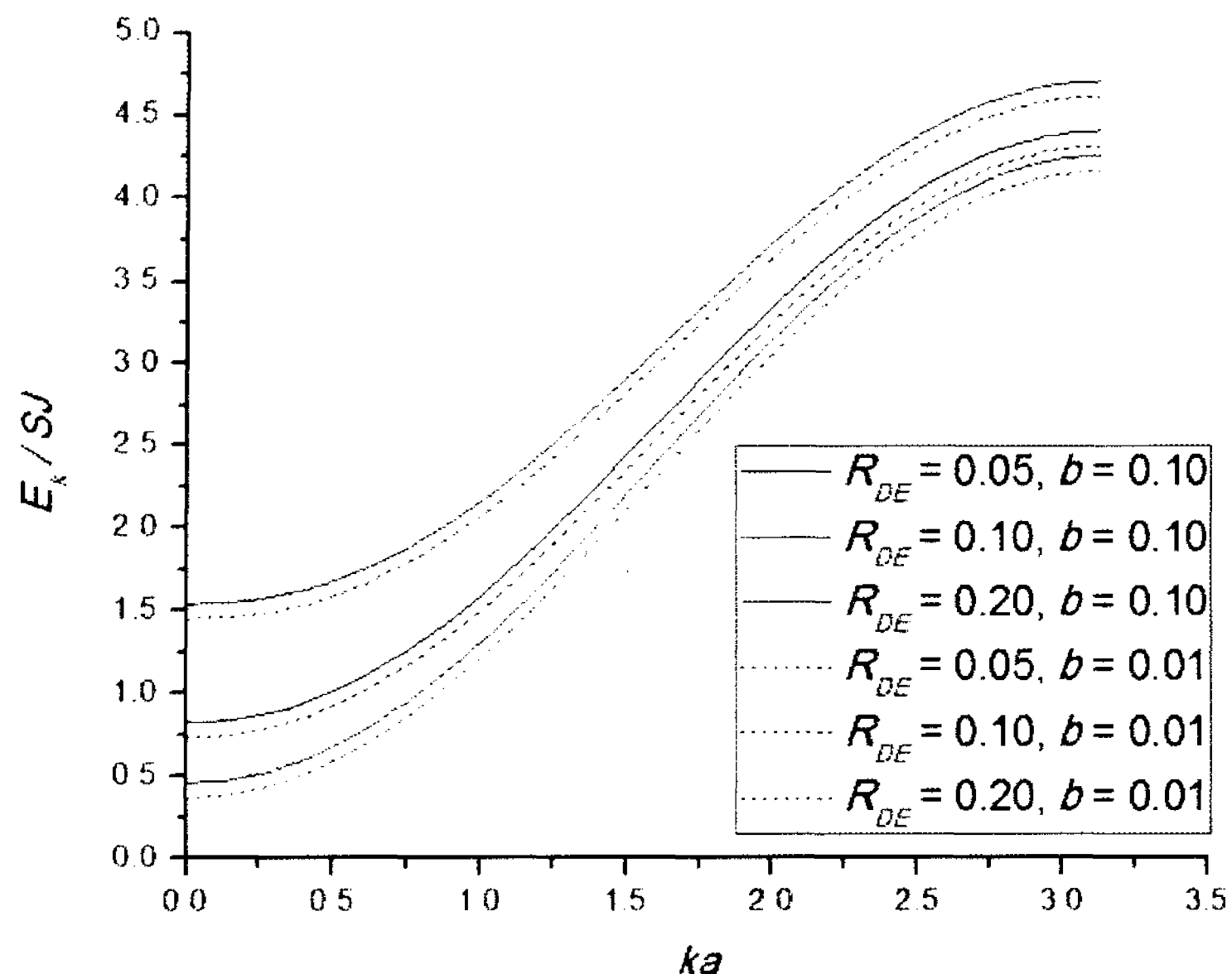


Fig. 4.1: Linear SW dispersion relation for varying dipole-exchange ratio R_{DE} and external field b .

First, the general formulation in Chapters 2 and 3 is for a low-temperature regime and therefore a critical temperature T_C needs to be deduced as a point of reference to define the temperature scale. In Chapter 1 we discussed a mean field estimate of the Curie temperature for any value of spin, in the exchange limit. The usual expression [1] now needs to be generalized to include the static dipolar field as well as the static exchange field, giving

$$T_C = \frac{1}{3k_B} S(S+1) [2J - g^2 u_B^2 D^{zz}(0)]. \quad (4.7)$$

For all the numerical calculations we will employ a dimensionless reduced temperature defined by $T_R = T/T_C$, where typically we take $T_R \leq 0.3$ to insure a low temperature regime. To proceed numerically we need to discretize the Brillouin Zone. We start by noting that in the limit $N \rightarrow \infty$ we can transform the summation over any wavenumber q

to an integral form

$$\frac{1}{N} \sum_q f(q) \rightarrow \frac{1}{2\pi} \int_{-\pi}^{\pi} f(q) dq, \quad (4.8)$$

where $f(q)$ is a q -dependent function. Next we divide the zone of integration up into $2M + 1$ cells each of width $2\pi/(2M + 1)$, where M is a large positive integer. In this scheme the centres of the elements are at wavenumber values $0, \pm 2\pi/(2M + 1), \pm 4\pi/(2M + 1), \dots, \pm 2\pi M/(2M + 1)$, i.e., at values $q = q_m$ where

$$q_m = 2\pi m/(2M + 1), \quad (4.9)$$

and the integer m ranges from $-M$ to M . Therefore we employ the numerical approximation

$$\frac{1}{2\pi} \int_{-\pi}^{\pi} f(q) dq \rightarrow \frac{1}{2M + 1} \sum_{-M}^M f(q_m). \quad (4.10)$$

By trial, using narrower and narrower cells to test for the appropriate convergence, we find that a value of $M = 2000$ is sufficient.

For the special case of a longitudinal field the three-magnon processes all vanish, as can be seen by referring back to Eq. (2.18). Since the angle-dependent coefficient γ vanishes at $\theta = 0$, all the V factors in Eq. (2.29) also vanish. As a result the lowest order nonlinear contribution comes from the fourth-order Hamiltonian.

Before proceeding to the more interesting cases when a transverse field component is present, we will calculate the SW energy shift ΔE_k due to the four-magnon process for a range of parameters. The relevant expressions are quoted in Eqs. (3.28), (3.29) and (2.31), but we note first that in the longitudinal case there is a simplification of the weighting factor Z_A which reduces to

$$Z_A = [J(k) + J(k') - J(0) - J(k - k')] + \frac{1}{2} g^2 \mu_B^2 [D^{z,z}(k) + D^{z,z}(k') + 2D^{z,z}(0) + 2D^{z,z}(k - k')] \quad (4.11)$$

After carrying out the internal wavenumber summation as described above, the energy shift as a function of wavenumber is plotted in Fig. 4.2. We see that ΔE_k is about two orders of magnitude smaller than E_k . In general the energy shift is negative for small wavenumber values and positive for larger wavenumber values. The wavenumber at which $\Delta E_k = 0$ appears to be roughly constant ($ka \approx 1.4$) for various longitudinal fields. However, we note that the magnitude of ΔE_k is reduced as b is increased. This is expected because an increase in b leads to an increase in the linear SW energy (as noted in Subsection 4.1.1) and hence to a decrease in the Bose-Einstein thermal factor in Eq. (3.28).

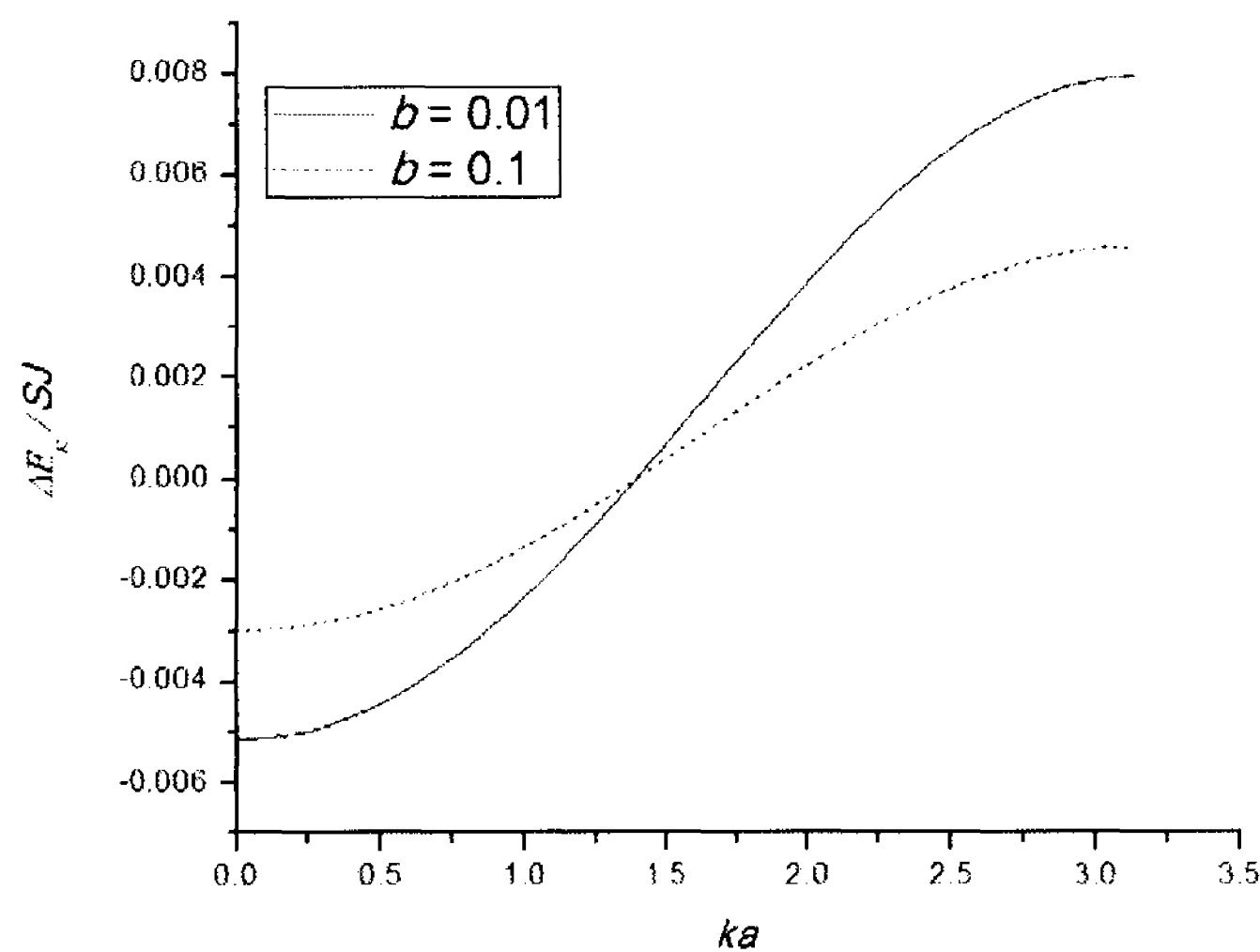


Fig. 4.2: SW energy shift vs. wavenumber ka at reduced temperature $T_R = 0.1$, dipole-exchange ratio $R_{DE} = 0.1$ and two values of the longitudinal field b .

The effect of varying the dipole-exchange ratio is seen by comparing the solid curve in Fig. 4.2 with Fig. 4.3. Reducing R_{DE} in this case increases the magnitude of the

energy shift at small k , while keeping the same overall qualitative behaviour. This is mainly because the energy gap in the linear SW spectrum has been reduced, thus increasing the Bose-Einstein factor in Eq. (3.28). Also, by comparing Fig. 4.2 (solid curve) with Fig. 4.4, we see that increasing the temperature leads to a large increase in the magnitudes of ΔE_k . This is expected since the Bose-Einstein factors are temperature dependent. It also follows that $\Delta E_k \rightarrow 0$ as $T_R \rightarrow 0$.

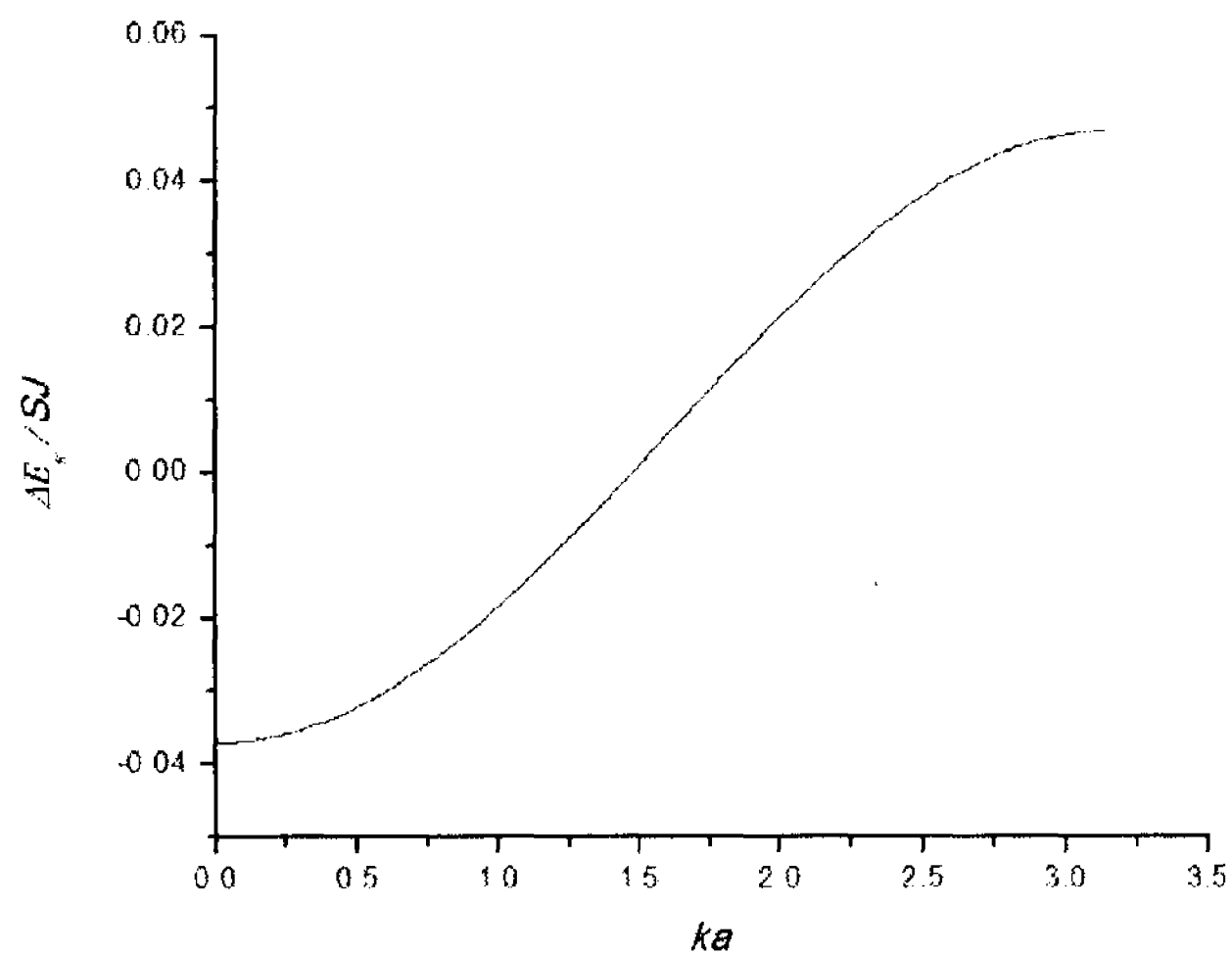


Fig. 4.3: SW energy shift vs. wavenumber ka at longitudinal field $b = 0.01$, dipole-exchange ratio $R_{DE} = 0.05$, and temperature $T_R = 0.1$.

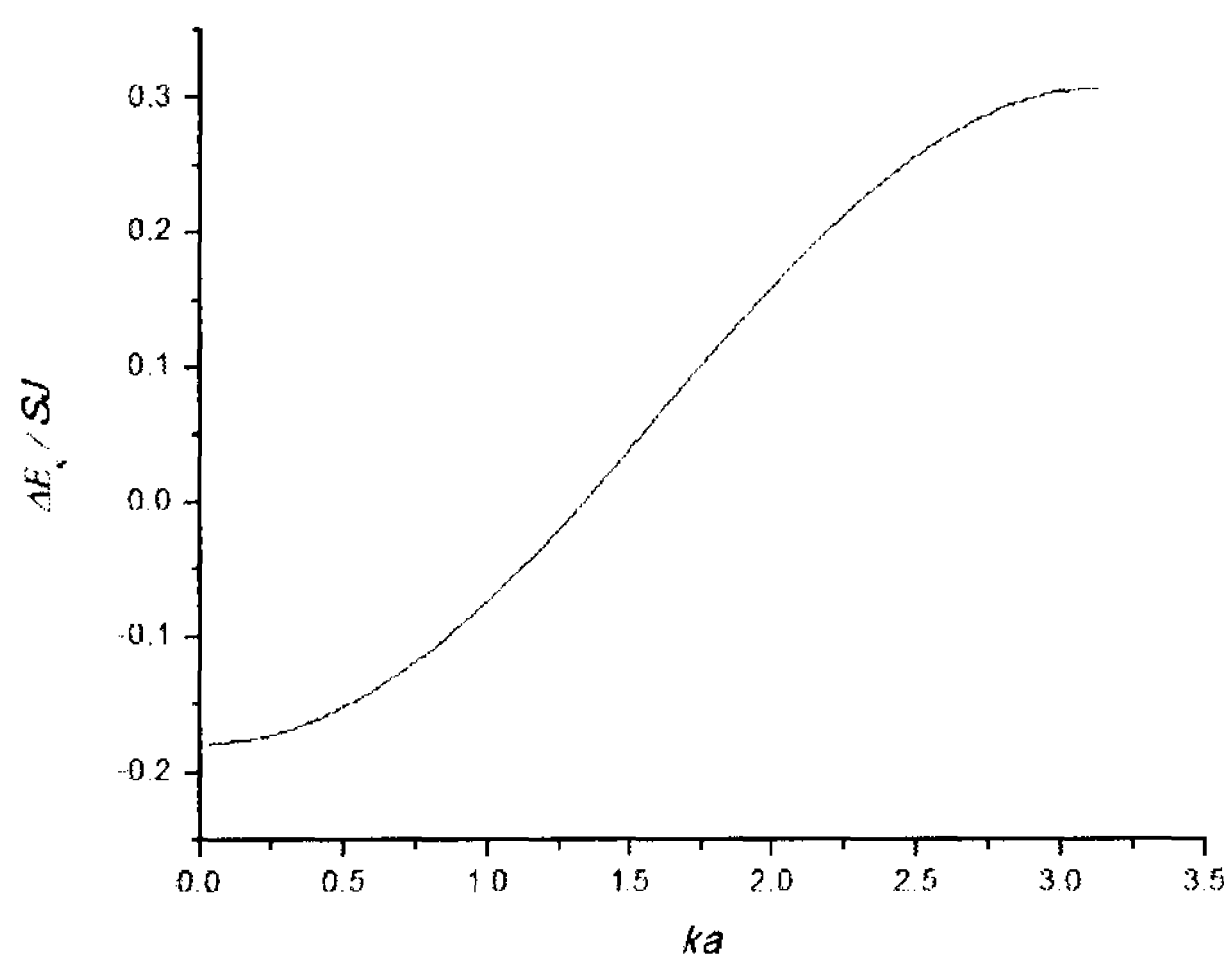


Fig. 4.4: SW energy shift vs. wavenumber ka at longitudinal field $b = 0.01$, dipole-exchange ratio $R_{DE} = 0.1$, and temperature $T_R = 0.3$.

4.2 Transverse applied magnetic field

For the case of a transverse applied magnetic field the spins in the system are canted towards the field direction. However, the canting orientation θ and the applied field orientation α are not necessarily the same, since θ depends on the magnitude of the applied field. This can be seen by substituting $\alpha = \pi/2$ into Eq. (4.1) and using trigonometric identities, to yield

$$(\sin \theta - B_0 / B_C) \cos \theta = 0, \quad (4.12)$$

where B_C was defined in Eq. (4.2). The above equation provides two solutions: either

$$\sin \theta = B_0 / B_C, \quad (4.13)$$

or $\cos \theta = 0$ (implying $\theta = \pi/2$). It can be easily established that for $B_0 < B_C$ the canting angle is obtained from Eq. (4.13), while for $B_0 \geq B_C$ the canting angle is $\pi/2$.

Thus here B_C behaves as a critical field at which the spins align parallel to the field in the transverse direction. There are two regimes of SW behaviour: $B_0 < B_C$ (which turns out to be the interesting case for the nonlinear SW properties) and $B_0 \geq B_C$.

4.2.1 Linear SW behaviour for a transverse field

Using the above relation between the canting angle and B_0 we can restate the linear SW dispersion relation in the form

$$E_k = \begin{cases} \left[\tilde{E}_k^2 + \frac{3}{2} \tilde{E}_k g^2 \mu_B^2 S (B_0 / B_C)^2 D^{z,z}(k) \right]^{1/2} & B_0 < B_C \\ \left\{ \left[\tilde{E}_k + g \mu_B (B_0 - B_C) \right]^2 + \frac{3}{2} g^2 \mu_B^2 S D^{z,z}(k) \left[\tilde{E}_k + g \mu_B (B_0 - B_C) \right] \right\}^{1/2} & B_0 \geq B_C \end{cases}, \quad (4.14)$$

where we define

$$\tilde{E}_k = S(J(0) - J(k)) - \frac{1}{2} g^2 \mu_B^2 S(2D^{\text{ex}}(0) + D^{\text{ex}}(k)). \quad (4.15)$$

At zero wavenumber the above expressions simplify to give the SW energy gap as

$$E_{k=0} = \begin{cases} g\mu_B [B_C^2 - B_0^2]^{1/2} & B_0 < B_C \\ g\mu_B [B_0^2 - B_C B_0]^{1/2} & B_0 \geq B_C \end{cases}. \quad (4.16)$$

It is interesting to note that, as B_0 becomes close to B_C , the energy gap $E_{k=0}$ approaches zero (i.e., the linear SW exhibits a soft-mode behaviour at $k=0$). The SW energy vs. B_0/B_C at various fixed wavenumbers is plotted in Fig. 4.5. Note that, at small but non-zero wavenumbers, the curves do not dip to zero energy.

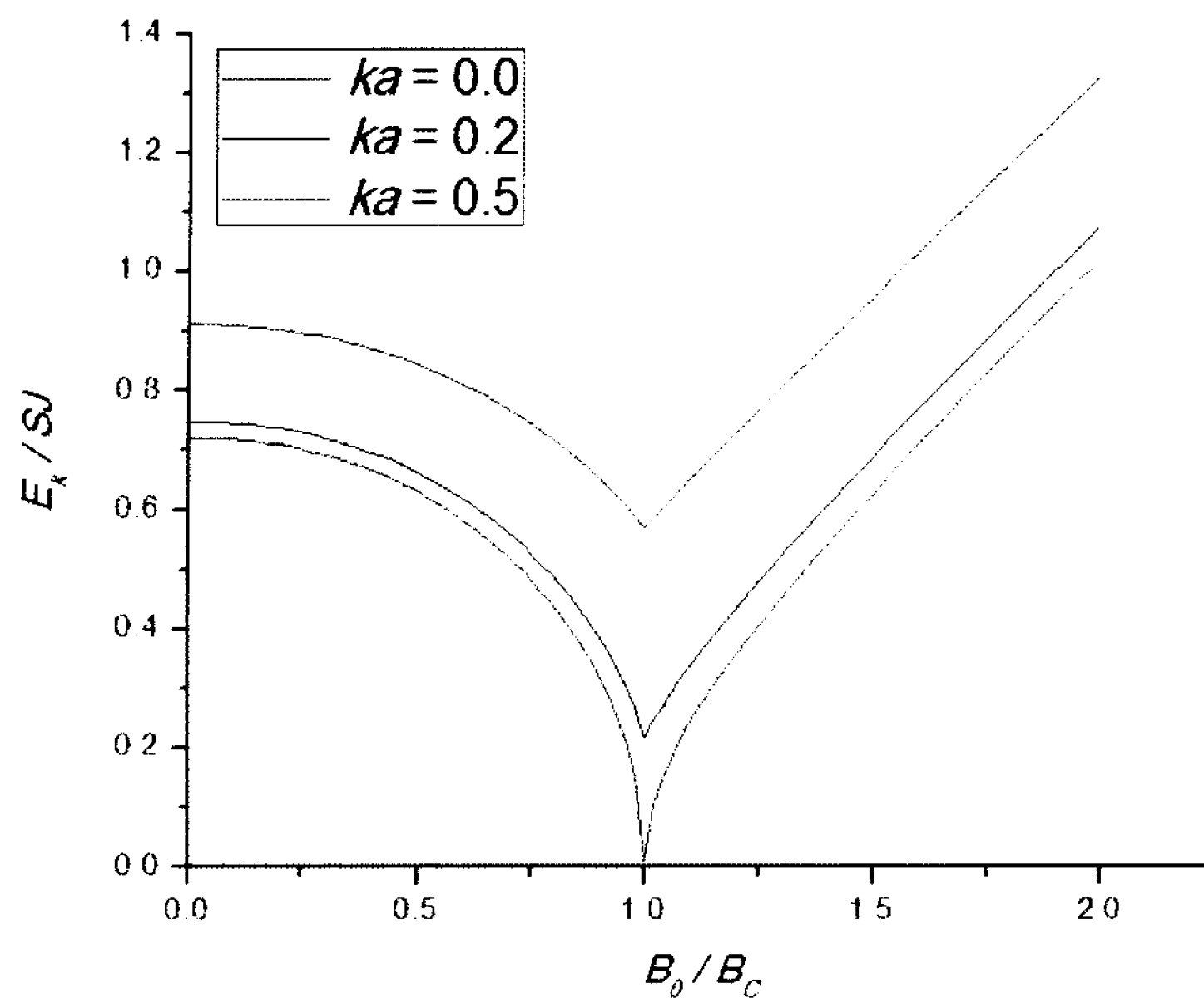


Fig. 4.5: Plot of E_k vs. B_0/B_C for dipole-exchange ratio of $R_{DE} = 0.1$ and several values of ka .

Next we plot in Fig. 4.6 the dispersion relations (E_k vs. k) for several values of

B_0/B_C . We see that increasing the field results in a larger range of values for E_k in the Brillouin zone. Another feature is that the energy near the centre of the Brillouin zone remains roughly unchanged (with a crossover occurring) provided $0 < B_0/B_C < 1$.

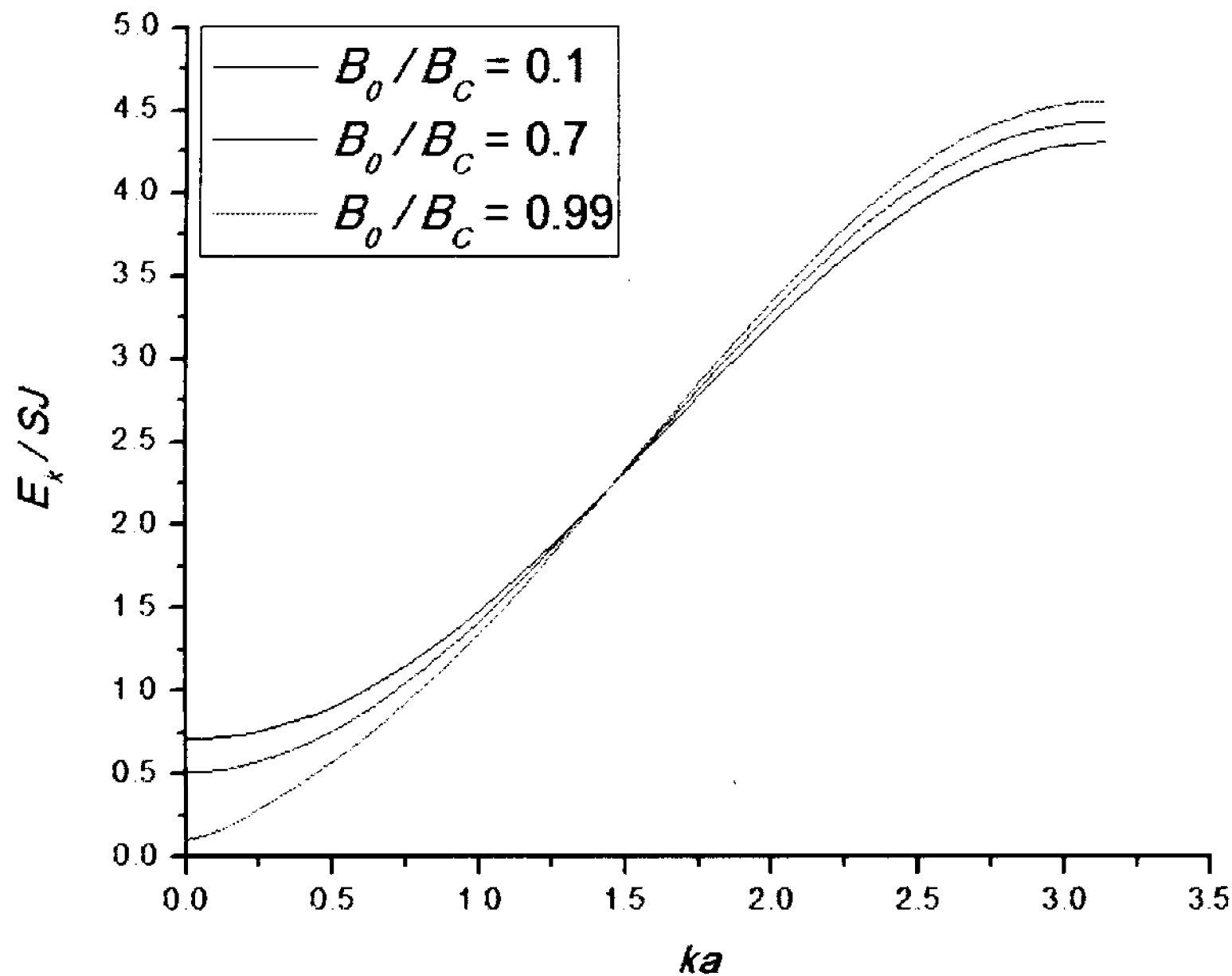


Fig. 4.6: Plot of the SW dispersion relation for various B_0/B_C and $R_{DE} = 0.1$.

4.2.2 SW renormalization for a transverse field

We now discuss the three-magnon damping process and its dependence on the external field, followed by some numerical examples. Referring back to Eq. (2.18) and using Eq. (4.1) we note that the coefficient γ , which depends on θ , is proportional to

$$\gamma \propto \frac{B_0}{B_C} \sqrt{\frac{B_C^2 - B_0^2}{B_C^2}} \quad (4.17)$$

for $B_0/B_C < 1$, while $\gamma = 0$ for $B_0/B_C \geq 1$. Since γ is an overall factor in the three-magnon vertices defined in Eq. (2.29), these results imply that the three-magnon renormalization effects vanish for all $B_0 \geq B_C$ as well as for $B_0 = 0$. It is easy to show

from Eq. (4.17) that the maximum value of γ occurs at $B_0/B_C = 1/\sqrt{2} \approx 0.71$.

To investigate the damping we need a numerical method for dealing with the energy-conserving delta functions appearing in the damping expressions in Chapter 3. This can be done straightforwardly by replacing the delta function with a normalized Lorentzian function of sufficiently small width. For example, the delta function corresponding to the “splitting” process in Eq. (3.27) can be replaced by

$$\delta(E_{k-k'} + E_{k'} - E_k) \rightarrow \frac{\sigma / \pi}{\sigma^2 + (E_{k-k'} + E_{k'} - E_k)^2}. \quad (4.18)$$

For accuracy we need to select a value for the half-width σ such that a sufficient number of points in the Brillouin zone summation fall within the width of the Lorentzian. Thus the choice of σ is related, in part, to the choice of the summation index M . By a simple analysis, including an empirical check for convergence, an appropriate value is $\sigma = 0.075$ in the dimensionless unit SJ of energy (and with M chosen as before).

Using Eq. (3.27) we now calculate the damping vs. wavenumber for several external field values. Panels (a) through (d) of Fig. 4.7 are examples of numerical plots at the same dipole-exchange ratio of $R_{DE} = 0.1$ and the same reduced temperature $T_R = 0.3$, but for different B_0/B_C . Contributions due to the splitting and confluence processes are shown as separate curves in the plots. There are several interesting trends that can be noted. One of the most obvious is that the damping due to the confluence process is typically smaller than that due to the splitting, mainly because of the different Bose-Einstein thermal factors. However, the confluence contribution becomes more comparable with the splitting contribution as the transverse field is increased. This latter

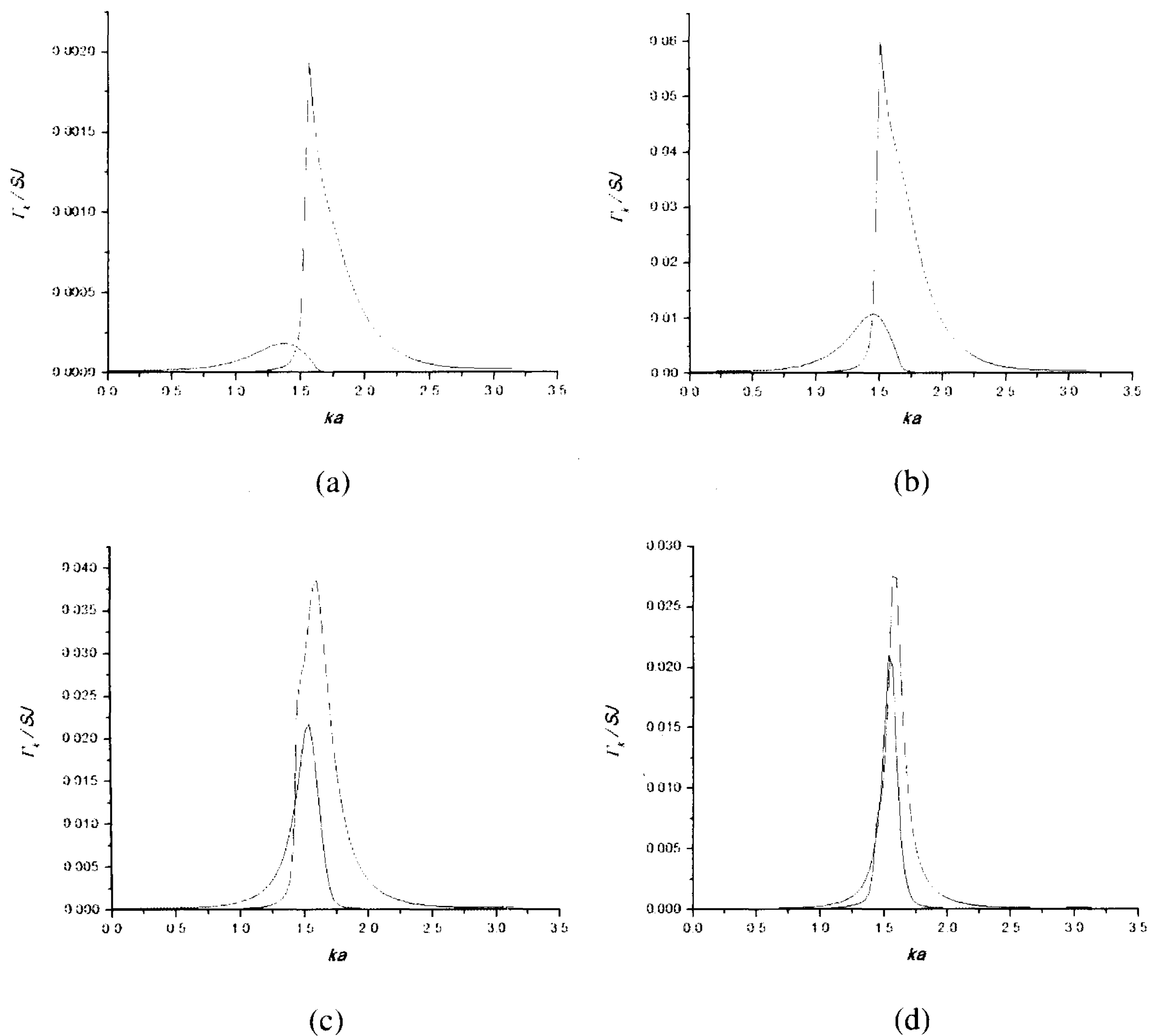


Fig. 4.7: SW damping vs. wavenumber at $R_{DE} = 0.1$ and $T_R = 0.3$: (a) $B_0 / B_C = 0.1$, (b) $B_0 / B_C = 0.7$, (c) $B_0 / B_C = 0.95$, and (d) $B_0 / B_C = 0.99$. Contributions from the splitting (black) and confluence (red) processes are shown.

behaviour is related to the fact that the SW energy gap decreases to a minimum as B_0 approaches B_C . Another interesting feature is that for B_0 near B_C the width of the damping profiles (in terms of ka) becomes smaller. This is presumably because the energy and wavenumber conservation conditions can then only be simultaneously satisfied in a more restricted range of wavenumbers. Also the damping has its peak near the middle of the Brillouin zone and is largest for $B_0 / B_C \approx 0.7$, which is close to the

value $1/\sqrt{2}$ where the overall factor γ has its maximum. Finally we see that the SW damping due to the confluence process can occur at smaller wavenumber values than that of the splitting process, for reasons that will become clear later.

Next we investigate what happens when the dipole-exchange ratio is changed. We would expect that the damping should increase with R_{DE} since the W factors defined in Subsection 3.2.1 for the three-magnon processes are dipole-dependent, leading to a factor of R_{DE}^2 . However, as R_{DE} is increased the thermal factors are reduced (because the SW energy gap is increased), so the overall effect on the SW damping is complicated. Comparing Fig. 4.7(b) with Fig. 4.8 we see that reducing R_{DE} by a factor of two significantly reduces the damping peak, as expected. Furthermore, we would expect that the threshold value of k where damping begins to take effect (damping turn-on) for the splitting process should become smaller with decreasing R_{DE} as a result of the reduction in the energy gap. This is because, as a crude approximation, the splitting can take place if the SW energy is at least double that of $E_{k=0}$, due to the conservation of energy. This condition does not apply for the confluence process since the merging of a SW with a thermal SW can happen at any energy as long as there are thermally excited SWs in the system. This is why in general the damping turn on for the confluence processes occurs at smaller wavenumber values than for the splitting processes.

Finally we investigate the effect of temperature on the damping vs. wavenumber curves. The temperature dependence comes through the Bose-Einstein factors in Eq. (3.27). In the zero temperature limit each Bose-Einstein factor approach zero, and so by inspection from Eq. (3.27) we see that the confluence process gives zero damping, while the splitting does not. Physically this seems reasonable since thermally excited SWs are

needed in the wire in order for the confluence of SWs to occur, while the splitting of a SW can occur independently of any thermally-excited SWs being present in the system. This phenomenon is apparent on comparing Fig. 4.7(b) with Fig. 4.9, where the temperatures are $T_R = 0.3$ and $T_R = 0.1$, respectively.

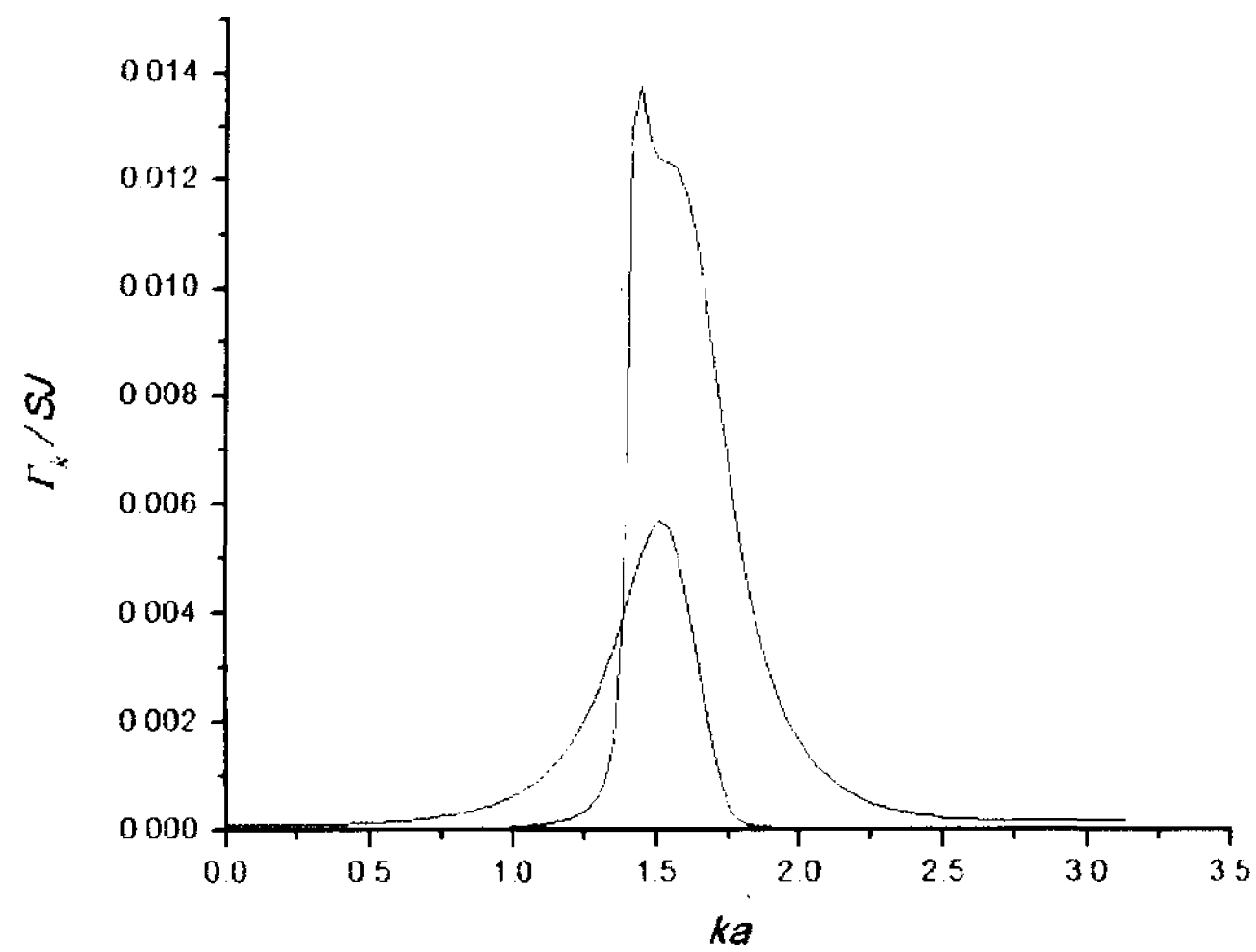


Fig 4.8: Damping vs. wavenumber at $T_R = 0.3$, $B_0 / B_C = 0.7$, $R_{DE} = 0.05$.

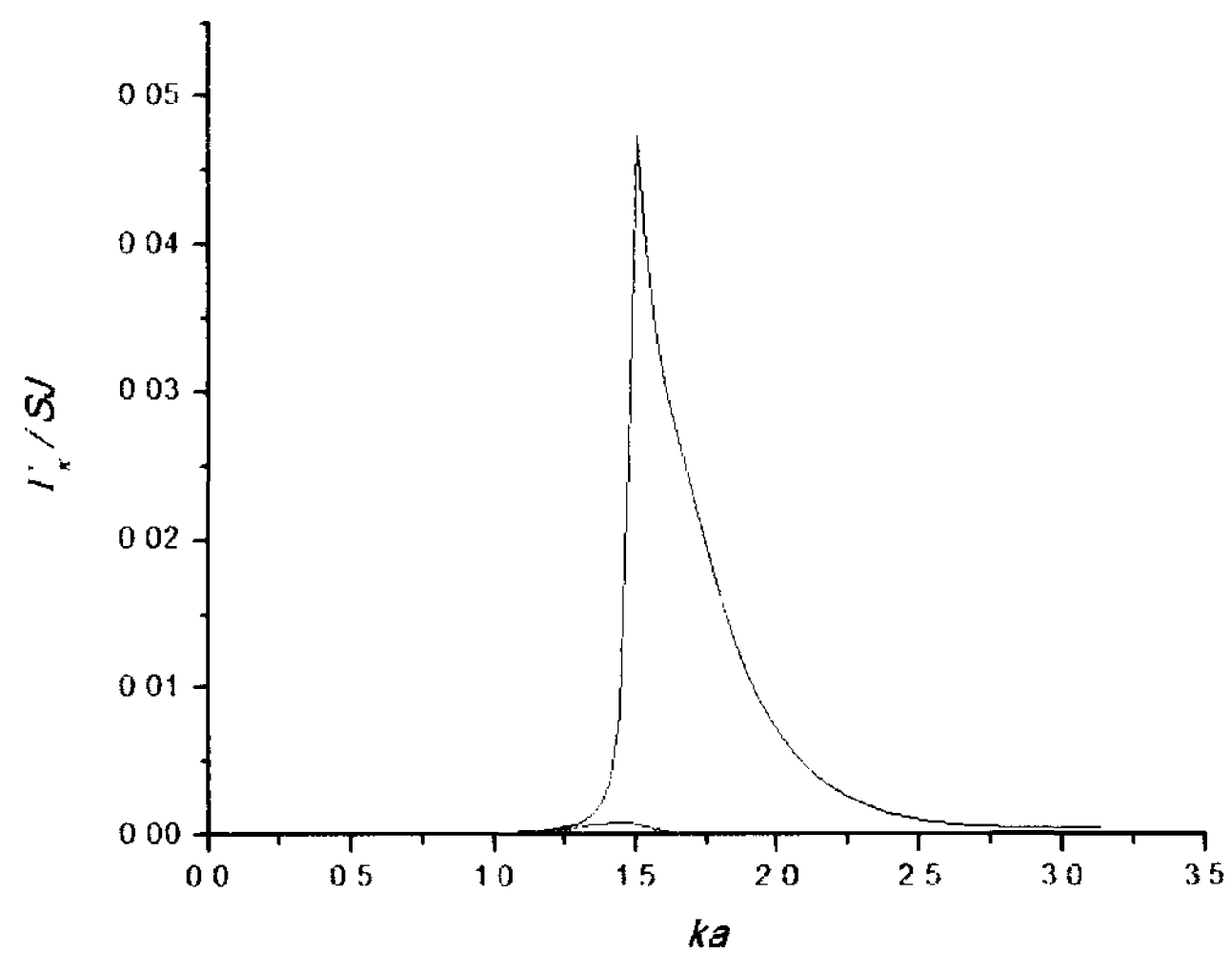


Fig 4.9: Damping vs. wavenumber at $T_R = 0.1$, $B_0 / B_C = 0.7$, $R_{DE} = 0.1$.

CHAPTER 5

Results for Oblique Applied Magnetic Field

In this chapter we will investigate the effects of an oblique applied field on the linear SW dispersion relation and the three-magnon SW damping processes. Specifically we will consider two field orientations, generalizing the results for the longitudinal and transverse fields in Chapter 4. The first case will be a field oriented at an angle of $\alpha = \pi/4$ (or 45°) with respect to the z -axis, and the second case will be a field at $\alpha = 4\pi/9$ (or 80°). The analogous numerical procedures to those in Chapter 4 will be applied here. Similar results could be obtained for any other chosen $0 < \alpha < \pi/2$.

5.1 Applied magnetic field at $\alpha = \pi/4$

We begin by substituting the field angle $\alpha = \pi/4$ (or 45°) into Eq. (4.1) and rearranging to obtain an expression for the canting angle θ as

$$\sin(2\theta) = (B_0/B_C) \left[\sqrt{(B_0/B_C)^2 + 2} - (B_0/B_C) \right], \quad (5.1)$$

where the characteristic field B_C is defined as before in Eq. (4.2). To illustrate the dependence of the canting angle on the field a plot of θ vs. B_0/B_C is given in Fig. 5.1, where we see that $\theta \rightarrow \pi/4$ as $B_0/B_C \rightarrow \infty$. The major distinction seen here between the oblique field case and the purely transverse field orientation discussed in Section 4.2 is that for the transverse case the spins align in the direction of the field at some finite critical value, whereas for $\alpha = \pi/4$ angle there is no such critical behaviour and θ tends to the value of α asymptotically.

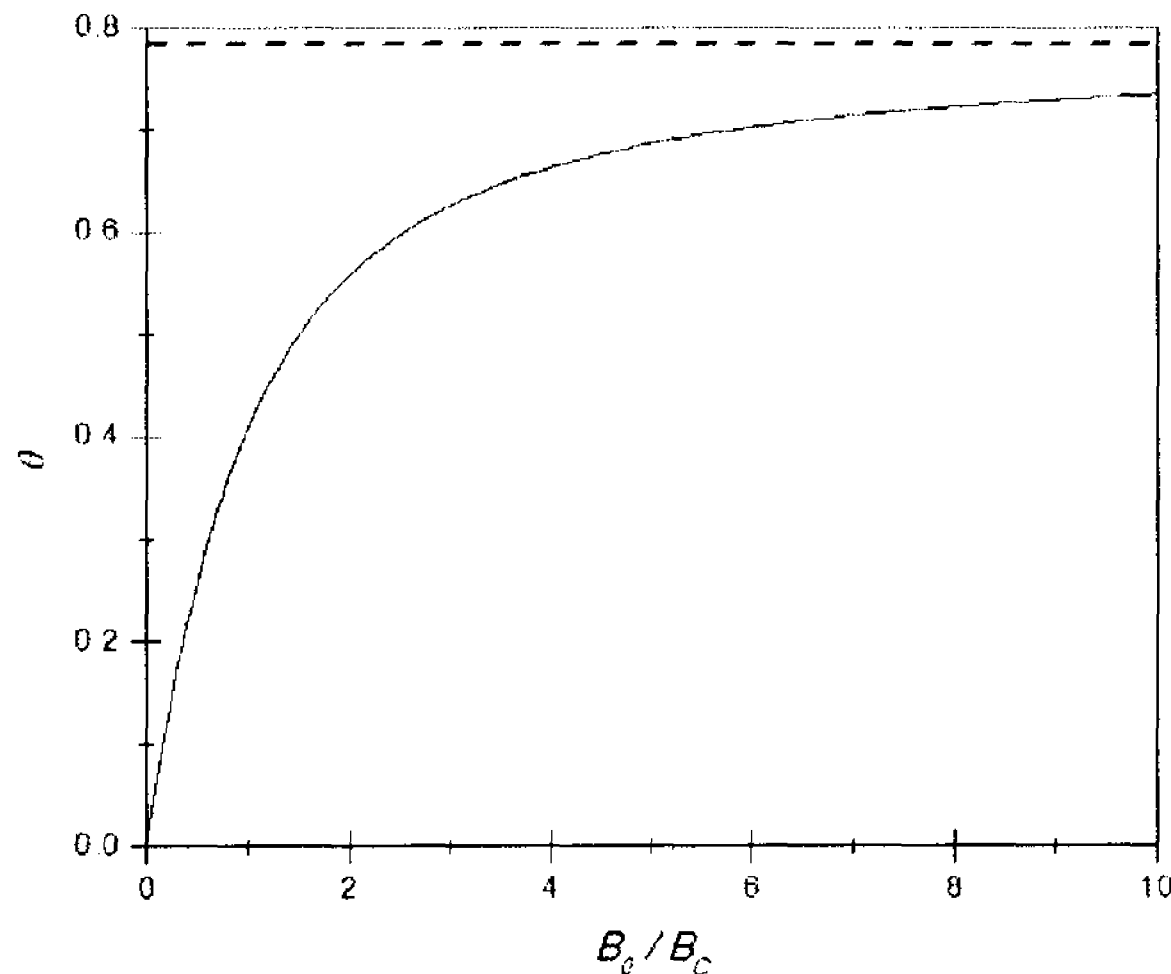


Fig. 5.1: Plot of θ (in radians) vs. B_0/B_C for a field orientation $\alpha = \pi/4$. The horizontal dashed line is at the asymptotic value corresponding to $\alpha = \pi/4 \approx 0.785$.

5.1.1 Linear SW behaviour for $\alpha = \pi/4$

The linear SW dispersion relation is defined as before by Eqs. (2.26) and (2.15).

However, the term $\cos(\alpha - \theta)$ in Eq. (2.15) can now be re-written as

$$\cos(\pi/4 - \theta) = \frac{1}{\sqrt{2}} \left(\sin \theta + \sqrt{1 - \sin^2 \theta} \right). \quad (5.2)$$

This, together with the result deduced from Eq. (5.1) that

$$\sin^2 \theta = 1/2 - (1/2) \left\{ 1 - (B_0/B_C)^2 \left(\sqrt{(B_0/B_C)^2 + 2} - (B_0/B_C) \right)^2 \right\}^{1/2}, \quad (5.3)$$

can be substituted into Eq. (2.15) in order to give an explicit expression from which numerical results for E_k may be obtained. Proceeding in a similar manner to Chapter 4, a plot of the linear SW energy vs. B_0/B_C at several fixed values of wavenumber are shown in Fig. 5.2. Unlike the transverse field case (see Fig. 4.5), there appears to be a steady increase of the energy E_k with increasing field when $\alpha = \pi/4$. Next we look at

the SW dispersion curves for various B_0/B_C values as in Fig. 4.6. The dispersion curves illustrated in Fig. 5.3 have a major distinction compared with the dispersion curves for the transverse field orientation. Here we find a vertical shift with varying field rather than

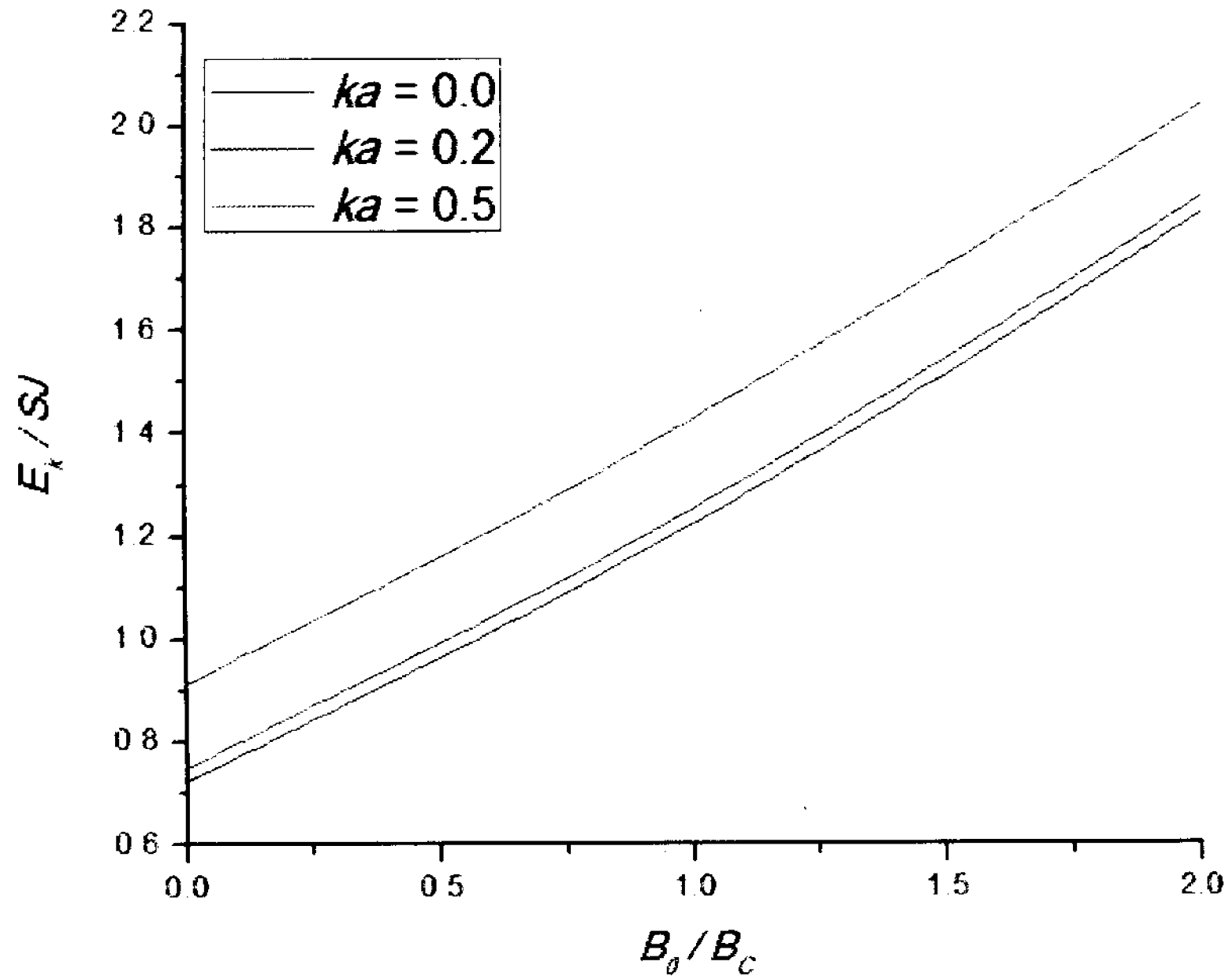


Fig. 5.2: Plot of fixed wavenumber energy vs. B_0/B_C at $R_{DE} = 0.1$.

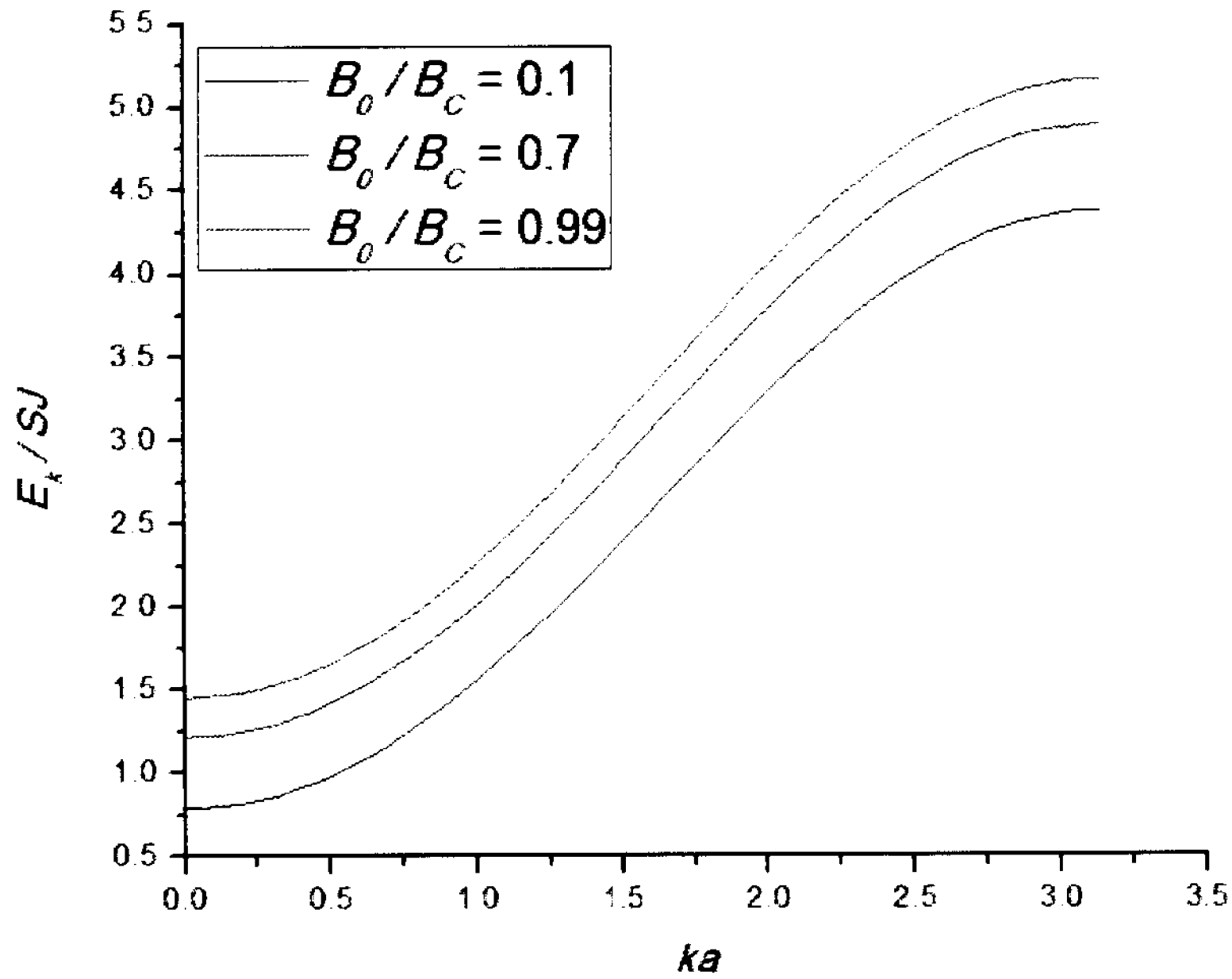


Fig. 5.3: Plot of the SW dispersion relation for various B_0/B_C at $\alpha = \pi/4$ and $R_{DE} = 0.1$.

the stretching effect in Fig. 4.6. Also for the same set of parameter values the energy gaps here are generally higher than for the transverse case. Overall, the linear SW behaviour is more similar to that found for the longitudinal field case.

5.1.2 SW renormalization for $\alpha = \pi/4$

From Eqs. (2.18) and (5.1) we see that the coefficient γ for the three-magnon processes now has its largest value as $B_0/B_C \rightarrow \infty$. This is different from the transverse field case, where there was a maximum for $B_0/B_C = 1/\sqrt{2}$ and for $B_0 > B_C$ the coefficient γ for the three-magnon damping vanished.

We now investigate the effect of the oblique field on the three-magnon damping. Fig. 5.4 shows some damping vs. wavenumber plots at fixed R_{DE} and T_R for various B_0/B_C . We see that as the field is increased the height of the damping peak also increases. This phenomenon is mainly due to the dependence on the canting coefficient γ which increases with B_0/B_C . However we also know from Subsection 5.1.1 that at large B_0 the SW energy gap $E_{k=0}$ becomes large. One consequence is that the delta function in the damping term becomes more restrictive, so we see that as B_0 increases the turn-on threshold value of the damping shifts to high wavenumbers. Also we note that with increasing field the confluence process becomes weaker relative to the splitting process, whereas in the transverse field case (provided $0 < B_0/B_C < 1$) the ratio of the confluence to the splitting increases with increasing field. This can again be understood in terms of the Bose-Einstein thermal factors.

The effects on the damping profile of varying the R_{DE} and T_R factors were also

investigated numerically. We found that they yielded the same general trends as in the case of the transverse field (see Section 4.2).

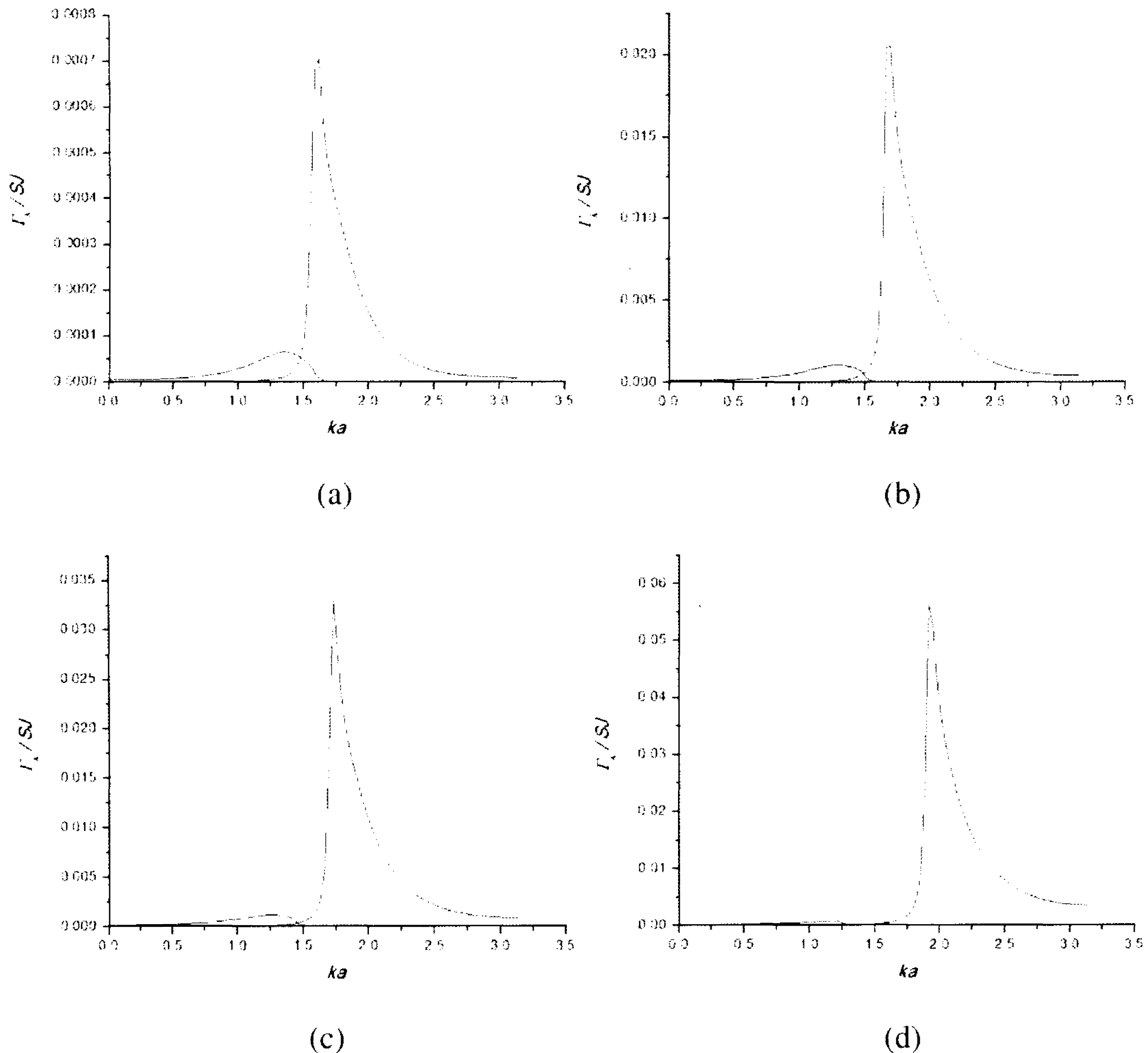


Fig. 5.4: Damping vs. Wavenumber at $R_{DE} = 0.1$, $T_R = 0.3$, (a) $B_0/B_C = 0.1$, (b) $B_0/B_C = 0.7$, (c) $B_0/B_C = 1.0$, and (d) $B_0/B_C = 2.0$.

5.2 Applied magnetic field at $\alpha = 4\pi/9$

We will now investigate the effect of an oblique field with α close to the transverse orientation, choosing $\alpha = 4\pi/9$ (or 80°). The motivation is to examine deviations from the “critical field” behaviour of the transverse case. For the present case we may employ an iterative method in order to deduce the canting angle θ , which

increases as B_0 is increased and tends to $4\pi/9$ as $B_0/B_C \rightarrow \infty$.

5.2.1 Linear SW behaviour for $\alpha = 4\pi/9$

We recall that in the transverse field orientation the SW energy gap $E_{k=0}$ decreases with increasing field until reaching zero at the critical field and then increasing again at larger field values (see Fig. 4.5). This dip does not occur when $\alpha = \pi/4$, but we might still expect to observe the formation of a dip if α is chosen to be near (but less than) $\pi/2$. This is what we see in Fig. 5.5 for the $\alpha = 4\pi/9$ case. A plot of linear SW energy vs. wavenumber for several values of B_0/B_C is presented in Fig. 5.6. The $k=0$ energy gap for different B_0/B_C values does not appear to change by much, but in other respects the behaviour is an intermediate case between Figs. 4.6 and 5.3.

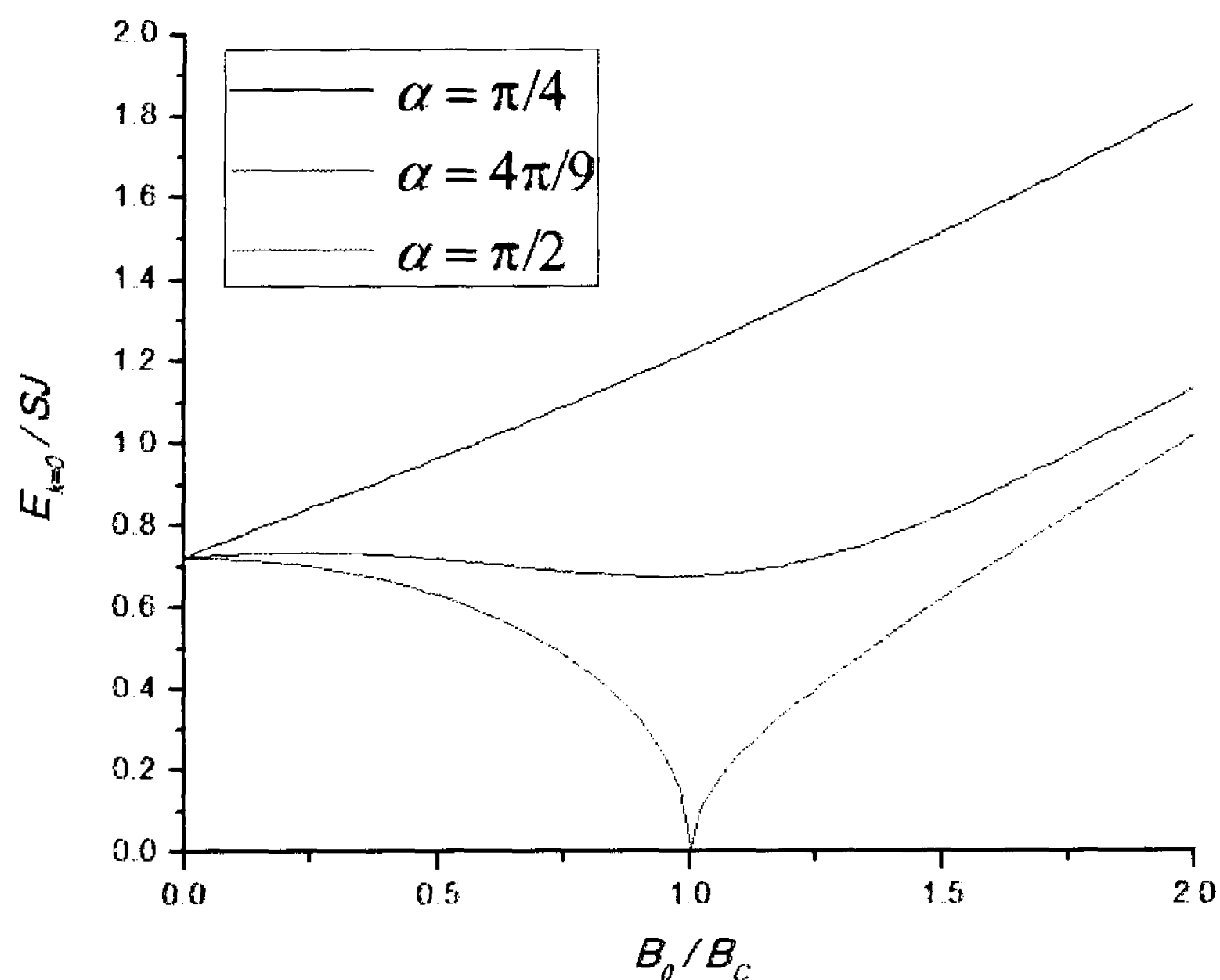


Fig. 5.5: Plot of zero $E_{k=0}$ vs. B_0/B_C at $R_{DE} = 0.1$ for different field orientations.

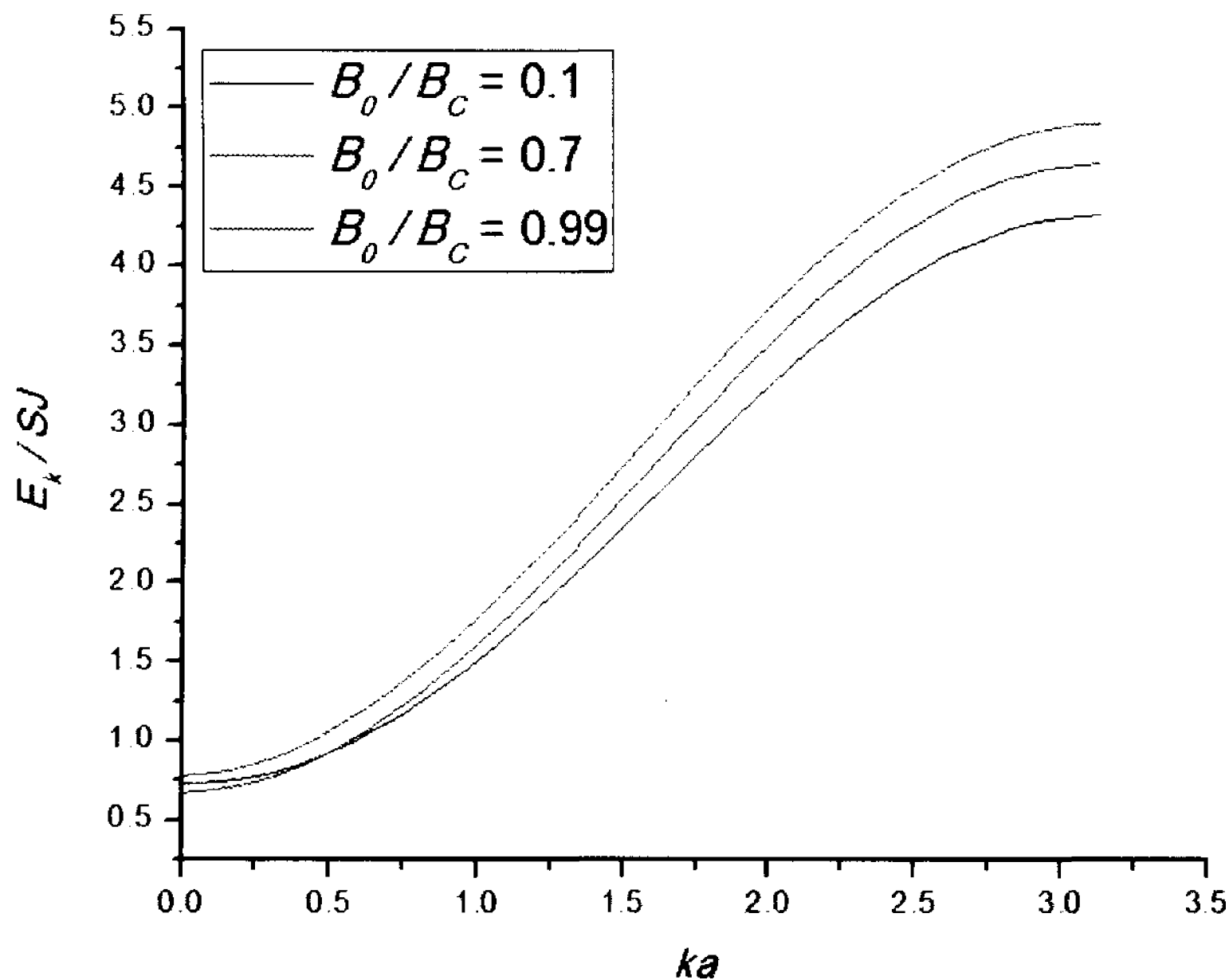
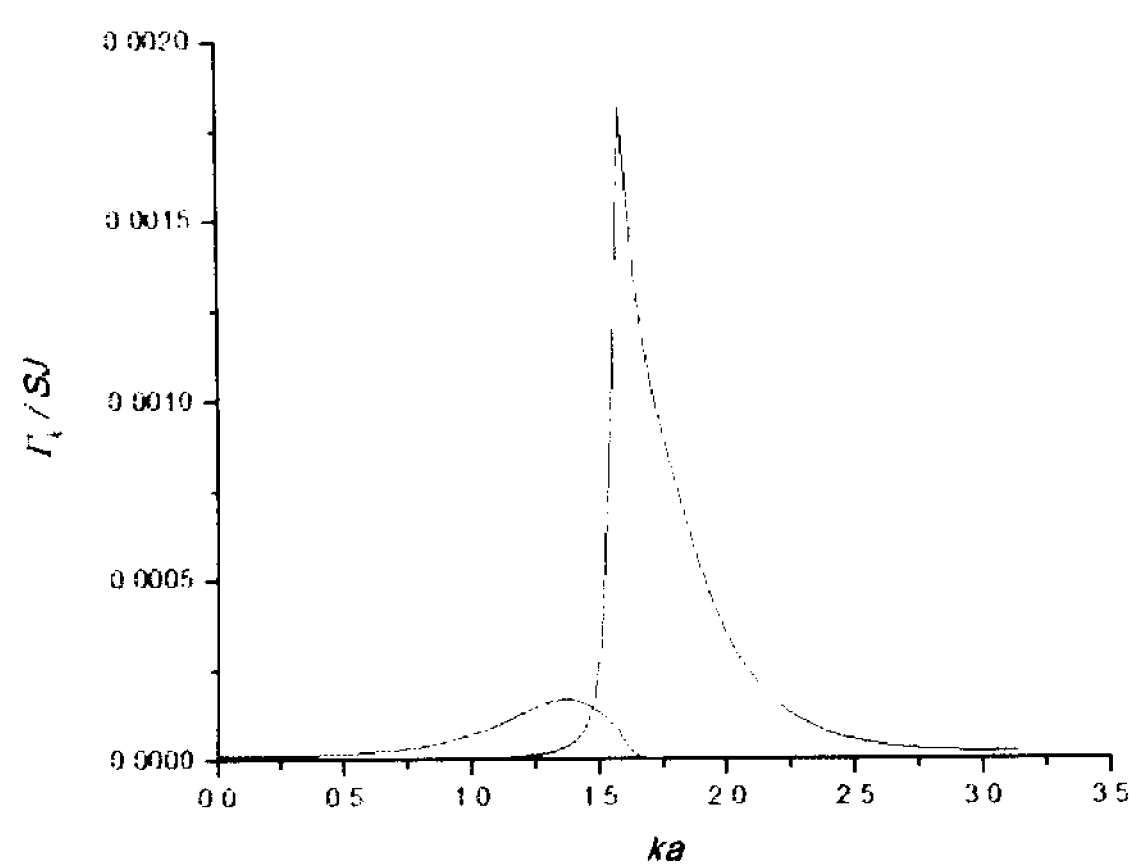


Fig. 5.6: Plot of the SW dispersion relation for various B_0/B_C at $\alpha = 4\pi/9$ and $R_{DE} = 0.1$.

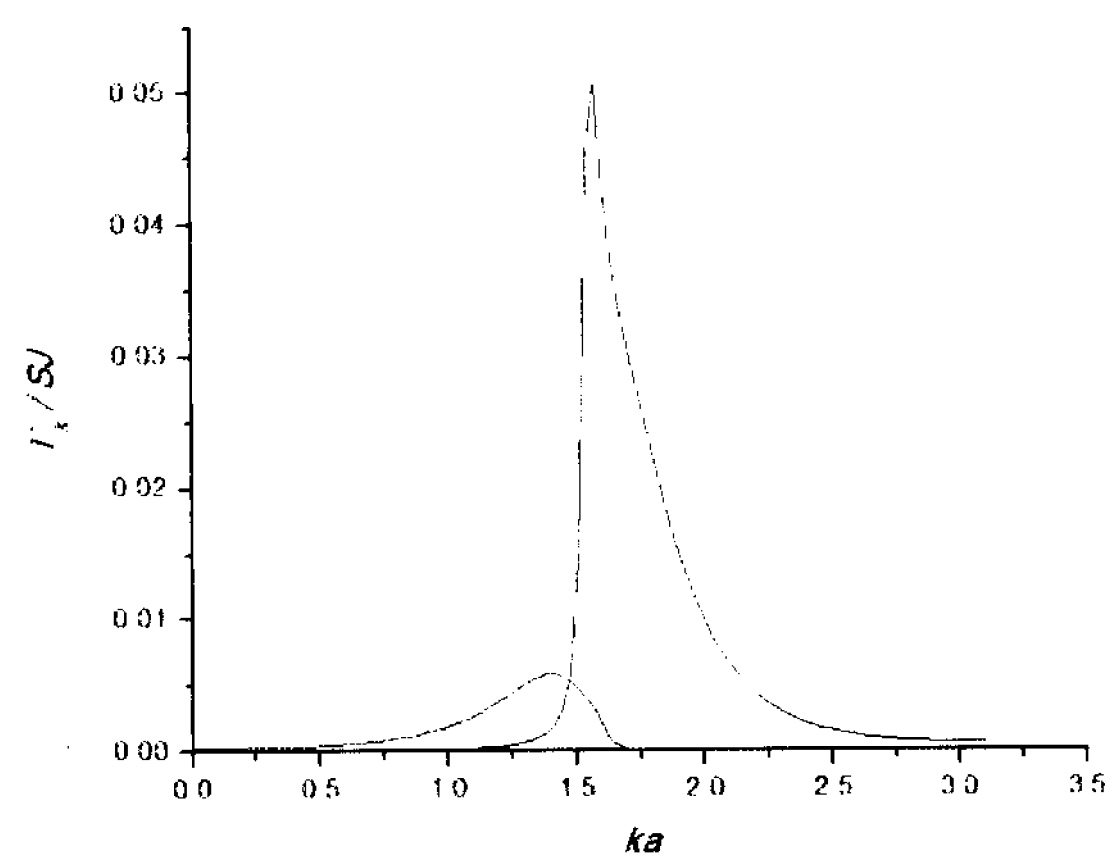
5.2.2 SW renormalization for $\alpha = 4\pi/9$

In Fig. 5.7 we present some plots for the SW damping vs. wavenumber using the same set of parameters as in Fig. 5.4 but with the field orientation now chosen to be $\alpha = 4\pi/9$. While there are several qualitative similarities, we can see an intermediate behaviour between the $\alpha = \pi/4$ and $\alpha = \pi/2$ cases. We recall that in the transverse case ($\alpha = \pi/2$) the three-magnon damping vanished for $B_0/B_C \geq 1$. By contrast, in the present case damping does still occur for field values above the characteristic field, but in Fig. 5.7 we notice that the damping peak at first increases with B_0/B_C but then begins to decrease for B_0/B_C greater than unity. This was not found for $\alpha = \pi/4$ field orientation (see Fig. 5.4). Furthermore, we see that the threshold wavenumber for the turn-on of damping tends to remain roughly constant with varying field as we would expect from

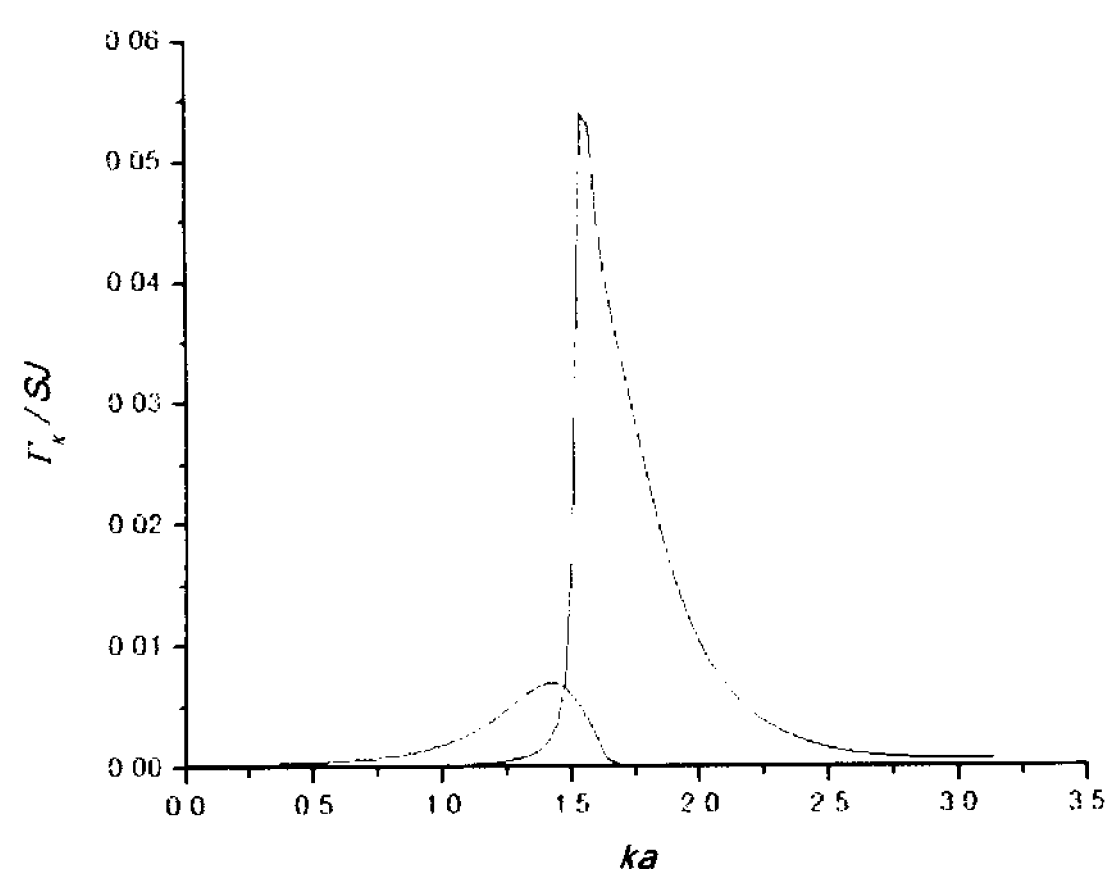
Fig. 5.6.



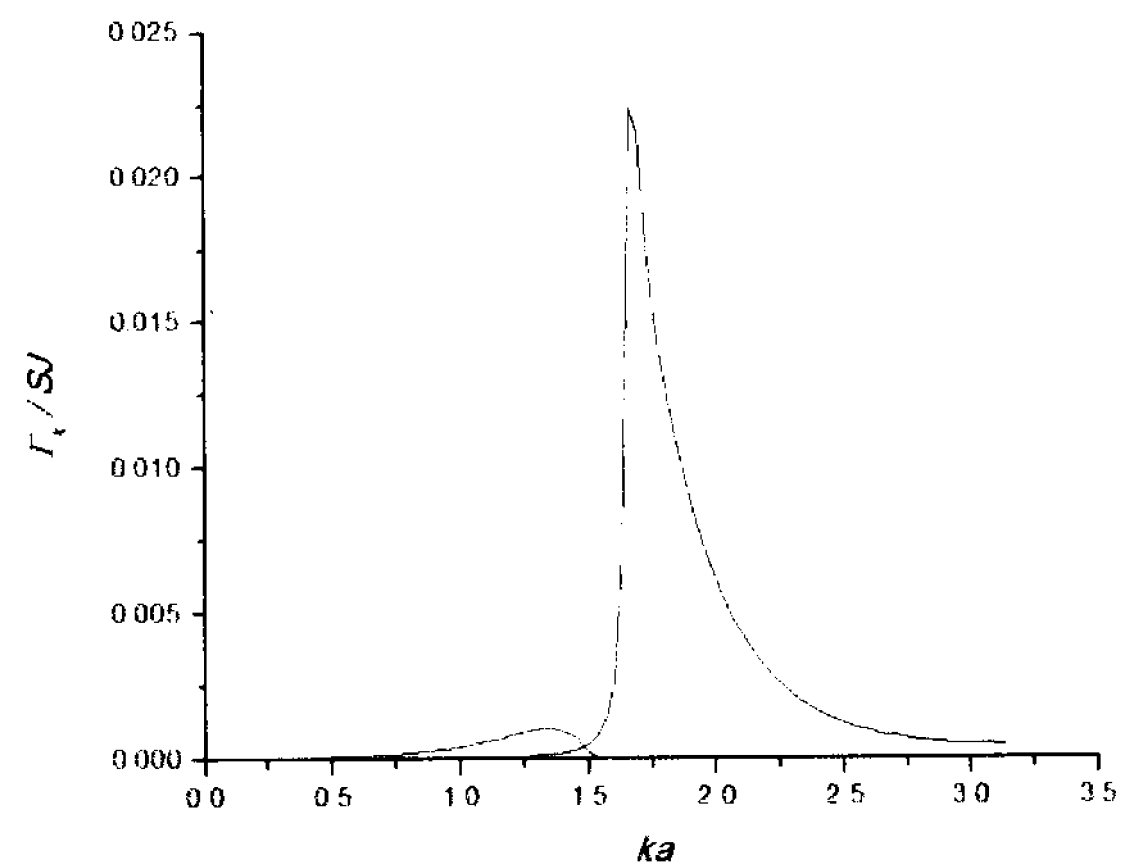
(a)



(b)



(c)



(d)

Fig. 5.7: Damping vs. Wavenumber at $R_{DE} = 0.1$, $T_R = 0.3$, (a) $B_0/B_C = 0.1$, (b) $B_0/B_C = 0.7$, (c) $B_0/B_C = 1.0$, and (d) $B_0/B_C = 2.0$.

CHAPTER 6

Conclusions

6.1 Review of the thesis

In this work the nonlinear dynamical properties of ferromagnetic nanowires, as represented by a single line of spins, are investigated. An applied magnetic field is considered to be applied at an arbitrary angle α relative to the symmetry axis of the wire. Except for the case of $\alpha = 0$, the field causes a canting of the spins, which we later find to be important for both the linear and nonlinear SW behaviour.

Starting in Chapter 2 from a spin Hamiltonian representation with the short-range exchange and long-range dipolar interaction terms included, the standard Holstein-Primakoff transformation is applied, relative to the equilibrium orientation of the canted spins, to re-express the Hamiltonian in terms of boson creation and annihilation operators. This transformation is done with a view to utilizing second quantization methods, namely a Green's function perturbation formalism in combination with Feynman diagrammatic techniques. The Hamiltonian is then expanded in such a way that each term in the Hamiltonian expansion corresponds to the number m of boson operators in that product, as in Eq. (2.10), and we consider all terms with $m \leq 4$. The vanishing of the first-order Hamiltonian $H^{(1)}$ provides an equilibrium condition for the canting angle of the spins. The second-order Hamiltonian $H^{(2)}$, which is quadratic in the boson operators and therefore analogous to a harmonic approximation, can be used to deduce the linear (or non-interacting) SW behaviour, and this has been extensively studied already in many magnetic systems (see, e.g., [5, 17, 19]).

Our focus is on the third and four order Hamiltonians, $H^{(3)}$ and $H^{(4)}$, which can be used to deduce the leading-order SW renormalization effects in a wire-like geometry. These nonlinear effects, corresponding to the three-magnon and four-magnon interactions processes respectively, have previously been studied theoretically in bulk materials [9, 17] and in thin films [39, 19], but not in nanowires. For the bulk and thin films materials there are three and two directions of translational symmetry, respectively, and hence three and two wavevector components that will characterize the SW modes. In the wire geometry, however, there is only one direction of translational symmetry and hence just one wavenumber, as introduced in Subsection 2.2.2. In a thin film geometry the formalism must deal with planes of spin (as in [19]), whereas in the wire geometry we are dealing with one or more lines of spins.

Apart from this aspect, the general form of the expressions for the SW damping and energy shift due to the three and four magnon processes are expected to be broadly similar in both the ultrathin film and wire geometries. With this in mind, we have followed a similar theoretical approach to that of [19] for ultrathin films. The most important difference comes in terms of the interaction potentials which encompass the geometry of the system under investigation. One of the achievements of the work presented here is that a more systematic procedure has been developed to classify the Feynman diagrams. This extension of previous theory is presented in Section 3.2, where the modified interaction vertices in the diagrams are represented by dots connected by Green's function lines. These are used, in combination with a permutation technique and careful inclusion of symmetry factors, to find expressions for the proper self energy. Using this new procedure (where we identified some minor corrections to the vertex

terms in [19]) the proper self energy expression for the three-magnon interaction is obtained. This directly leads to the formal expressions for the three-magnon energy shift and damping.

Numerical calculations are then carried out in Chapters 4 and 5 for the three-magnon damping process, while the four-magnon damping process (which is typically expected to be smaller) is discussed qualitatively. The numerical calculations for the single-line wire geometry yield many interesting results, particularly in regards to the dependence on both the magnitude and direction of the applied field. It is especially noteworthy that for a transverse external field, the existence of a critical field B_c can be identified (see Section 4.2), and above this field value (which is related to the strength of the dipolar coupling) the three-magnon damping process vanishes. By contrast, for oblique angles of the applied field (see Chapter 5) the behaviour is found to be quite different with no such critical-field effect occurring.

Since we have considered just one line of spins to form a magnetic nanowire, there is a restriction on the range of applicability for our theoretical model. In the simulation of magnetic materials on the submicron scale it is a well-established procedure to divide up the sample into small regions and then replace the individual spins in a region by one effective spin [40]. The validity criterion (see [28]) for making this replacement is that the dimensions of the small regions must be comparable with (or smaller) than the so-called “exchange length”. This is a characteristic property of any material, but for metals like nickel or Permalloy it is of order 5-7nm. Thus our results apply to ultrathin nanowires with diameters less than this amount.

6.2 Possible extensions

A direct extension to this work can be made by modifying the formulation so that it can be applied to wires with any number N_0 of lines of interacting spins in their cross section, i.e., to wires of greater thickness than the exchange length. The location of any spin in the system must now be designated by two index labels, say $\{i, n\}$, rather than just i . Here i indicates the location of any spin along a chain, while n is the index label of the line of spins (where $n = 1, 2, \dots, N_0$). A wavenumber Fourier transform can again be defined for i along the symmetry direction of the wire, while the transverse spatial quantization effects in the system are due to the index n . Two geometries are illustrated schematically in Fig. 6.1, where one example represents a stripe of finite width and the other represents an approximately circular wire with finite radius. For these geometries with multiple lines of spins a generalized Bogoliubov transformation (replacing that in Chapter 2) must be applied to re-express the second-order Hamiltonian in terms of a new set of operators. By diagonalizing the new expression for $H^{(2)}$ the linear SW dispersion relation can be obtained, e.g., by following the approach in [28]. For N_0 lines of spins there are N_0 branches in the SW dispersion curves.

A motivation for extending this work to striped nanowire geometries is that new experimental data have very recently become available. In Ref. [23] a FMR technique was used to measure the damping of the dipole-exchange SW in Permalloy nanowires with a stripe geometry.

It is interesting to note that for the multiple lines of spins the role of the interwire dipolar terms, will be such that, regardless of the orientation and magnitude of the applied field, there are always three-magnon processes. This contrast with the single line of spins

in a longitudinal field or in a transverse field for $B_0 > B_c$.

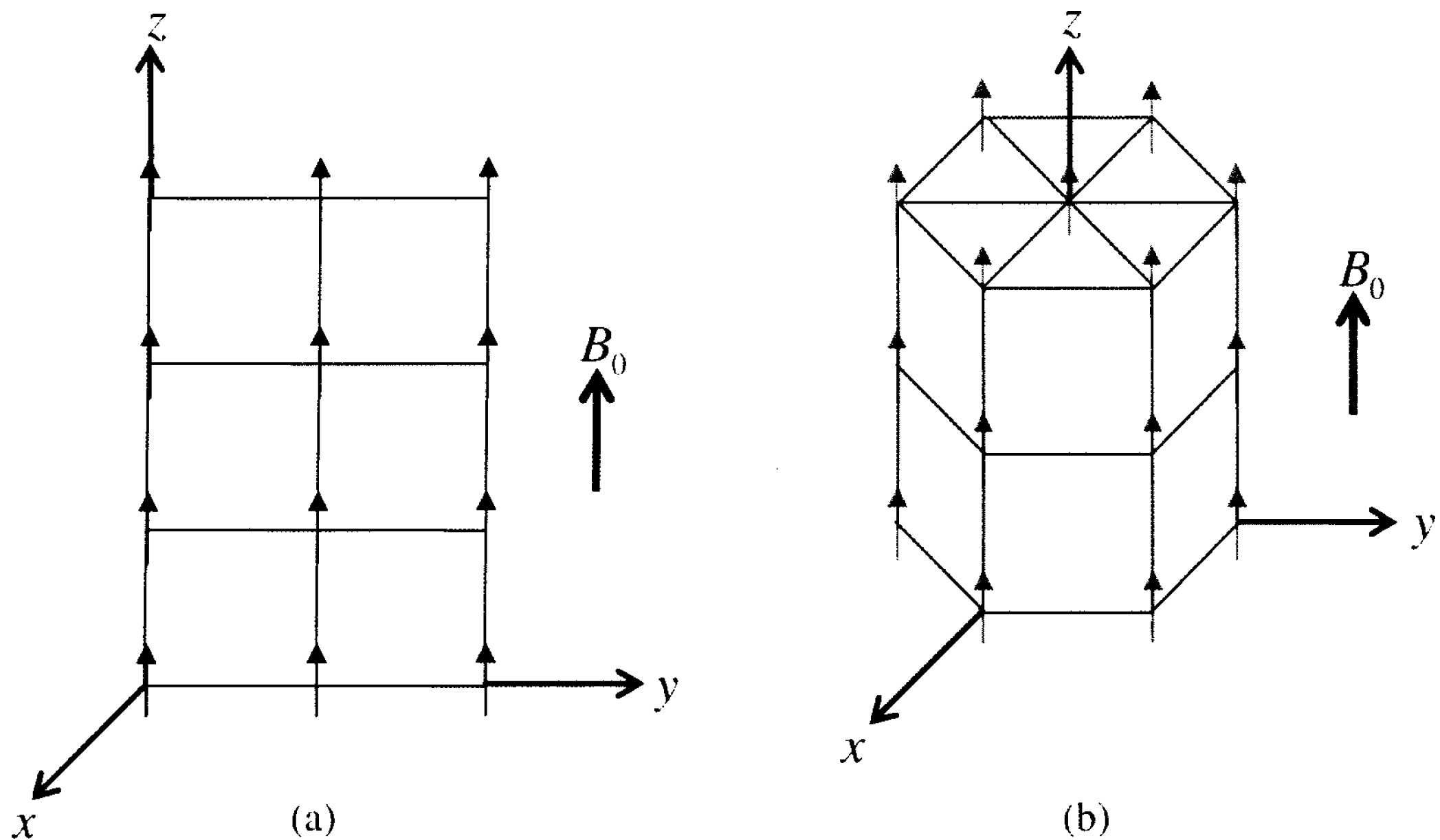


Figure 6.1: Schematic representations of two wire-like geometries with (a) $N_0 = 3$ and (b) $N_0 = 7$. The applied field is taken to be along the symmetry axis (z -direction)

In order to illustrate some of the new phenomena we consider the simple stripe geometry with $N_0 = 3$ in Fig. 6.1(a). We have calculated the linear SW dispersion relation for this case, extending our formalism in Chapter 2, and the results are shown in Fig. 6.2 where the curves are plotted for both positive and negative regions of the Brillouin zone. We consider several examples of the possible three-magnon splitting processes that conserve energy and wavenumber, all of which are expected to occur in the generalized theory for the damping. In the first case, labelled A, we have a SW on the bottom branch splitting into two other SWs on to the same branch. This process is similar to those studied in the previous chapters for the single chain. In the second case (B) we consider a SW at $k = 0$ on the middle branch, which can decay by splitting into two SWs on the bottom branch. In general, the SWs on the upper branches can decay through the

splitting process even at zero wavenumber. In the third scenario (C) we consider a SW on the top branch splitting into two SWs, one on to the bottom branch and one on to the middle branch. In this last case there are three different branches involved in the splitting process.

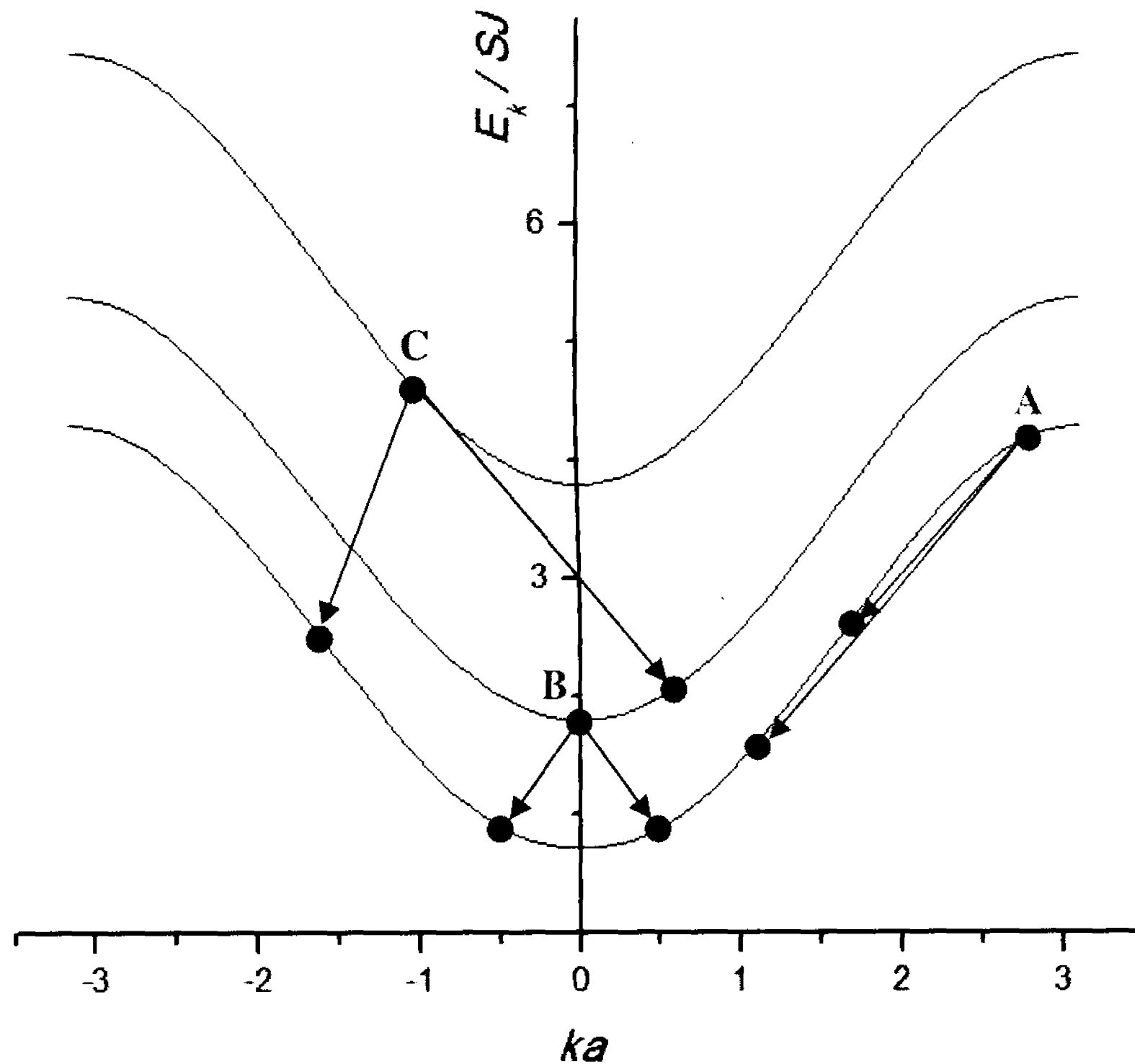


Figure 6.2: Dispersion relation for three lines of spin for $b = 0.1$ and $R_{DE} = 0.1$. The dots and arrow indicate some possible splitting processes.

Another extension of this thesis would be to consider the nonlinear processes for other types of magnetic nanowires, such as those composed of antiferromagnets. The dipole-exchange SWs in the linear approximation have previously been studied theoretically for an antiferromagnetic nanowire geometry [41], and this work can be used as the starting point to extend the nonlinear SW theory for ferromagnetic nanowires in this thesis to the case of antiferromagnetic nanowires.

APPENDIX A

The Weighting Factors for the Fourth-Order Hamiltonian

The expressions for the weighting factors $\Lambda_p(k_1, k_2, k_3, k_4)$, with $p = 1, 2, 3, 4, 5$, appearing in Eq. (2.30) are

$$\begin{aligned} \Lambda_1 = & \mu_1(k_1, k_2, k_3, k_4) s_{k_1} s_{k_2} s_{-k_3} s_{-k_4} + \mu_1(k_1, k_4, k_3, k_2) s_{k_1} t_{k_4} s_{-k_3} t_{-k_2} + \mu_1(k_1, k_3, k_2, k_4) s_{k_1} t_{k_3} t_{-k_2} s_{-k_4} \\ & + \mu_1(k_4, k_2, k_3, k_1) t_{k_4} s_{k_2} s_{-k_3} t_{-k_1} + \mu_1(k_3, k_2, k_1, k_4) t_{k_3} s_{k_2} t_{-k_1} s_{-k_4} + \mu_1(k_3, k_4, k_1, k_2) t_{k_3} t_{k_4} t_{-k_1} t_{-k_2} \\ & + \mu_2(k_1, k_3) s_{k_1} s_{k_2} t_{k_3} s_{-k_4} + \mu_2(k_1, k_2) s_{k_1} t_{k_3} s_{k_2} s_{-k_4} + \mu_2(k_1, k_3) s_{k_1} t_{k_4} t_{k_3} t_{-k_2} \\ & + \mu_2(k_3, k_1) t_{k_3} s_{k_2} s_{k_1} s_{-k_4} + \mu_2(k_4, k_3) t_{k_4} s_{k_2} t_{k_3} t_{-k_1} + \mu_2(k_3, k_1) t_{k_3} t_{k_4} s_{k_1} t_{-k_2} \\ & + \mu_3(k_4, k_2) s_{k_1} s_{-k_4} s_{-k_3} t_{-k_2} + \mu_3(k_3, k_4) s_{k_1} s_{-k_3} t_{-k_2} s_{-k_4} + \mu_3(k_4, k_2) t_{k_3} s_{-k_4} t_{-k_1} t_{-k_2} \\ & + \mu_3(k_2, k_4) s_{k_1} t_{-k_2} s_{-k_3} s_{-k_4} + \mu_3(k_2, k_1) t_{k_4} t_{-k_2} s_{-k_3} t_{-k_1} + \mu_3(k_2, k_4) t_{k_3} t_{-k_2} t_{-k_1} s_{-k_4} \end{aligned}$$

$$\begin{aligned} \Lambda_2 = & \mu_1(k_1, k_2, k_3, k_4) s_{k_1} t_{k_2} s_{-k_3} s_{-k_4} + \mu_1(k_2, k_1, k_3, k_4) t_{k_2} s_{k_1} s_{-k_3} s_{-k_4} + \mu_1(k_4, k_2, k_3, k_1) t_{k_4} t_{k_2} s_{-k_3} t_{-k_1} \\ & + \mu_1(k_3, k_2, k_1, k_4) t_{k_3} t_{k_2} t_{-k_1} s_{-k_4} + \mu_2(k_1, k_3) s_{k_1} t_{k_2} t_{k_3} s_{-k_4} + \mu_2(k_2, k_3) t_{k_2} s_{k_1} t_{k_3} s_{-k_4} \\ & + \mu_2(k_3, k_1) t_{k_3} t_{k_2} s_{k_1} s_{-k_4} + \mu_2(k_4, k_3) t_{k_4} t_{k_2} t_{k_3} t_{-k_1} + \mu_3(k_2, k_4) s_{k_1} s_{-k_2} s_{-k_3} s_{-k_4} \\ & + \mu_3(k_2, k_1) t_{k_4} s_{-k_2} s_{-k_3} t_{-k_1} + \mu_3(k_2, k_4) t_{k_3} s_{-k_2} t_{-k_1} s_{-k_4} + \mu_3(k_1, k_4) t_{k_2} t_{-k_1} s_{-k_3} s_{-k_4} \end{aligned}$$

$$\begin{aligned} \Lambda_3 = & \mu_1(k_1, k_2, k_4, k_3) s_{k_1} s_{k_2} s_{-k_4} t_{-k_3} + \mu_1(k_1, k_2, k_3, k_4) s_{k_1} s_{k_2} t_{-k_3} s_{-k_4} + \mu_1(k_1, k_4, k_3, k_2) s_{k_1} t_{k_4} t_{-k_3} t_{-k_2} \\ & + \mu_1(k_4, k_2, k_3, k_1) t_{k_1} s_{k_2} t_{-k_3} t_{-k_4} + \mu_2(k_1, k_3) s_{k_1} s_{k_2} s_{k_3} s_{-k_4} + \mu_2(k_1, k_4) s_{k_1} s_{k_2} t_{k_4} t_{-k_3} \\ & + \mu_2(k_1, k_3) s_{k_1} t_{k_4} s_{k_3} t_{-k_2} + \mu_2(k_4, k_3) t_{k_4} s_{k_2} s_{k_3} t_{-k_1} + \mu_3(k_4, k_2) s_{k_1} s_{-k_4} t_{-k_3} t_{-k_2} \\ & + \mu_3(k_2, k_3) s_{k_1} t_{-k_2} s_{-k_4} t_{-k_3} + \mu_3(k_2, k_4) s_{k_1} t_{-k_2} t_{-k_3} s_{-k_4} + \mu_3(k_2, k_1) t_{k_4} t_{-k_2} t_{-k_3} t_{-k_1} \end{aligned}$$

$$\Lambda_4 = \mu_1(k_1, k_2, k_3, k_4) s_{k_1} s_{k_2} t_{-k_3} t_{-k_4} + \mu_2(k_1, k_3) s_{k_1} s_{k_2} s_{k_3} t_{-k_4} + \mu_3(k_2, k_4) s_{k_1} t_{-k_2} t_{-k_3} t_{-k_4},$$

$$\Lambda_5 = \mu_1(k_1, k_2, k_3, k_4) t_{k_1} t_{k_2} s_{-k_3} s_{-k_4} + \mu_2(k_1, k_3) t_{k_1} t_{k_2} t_{k_3} s_{-k_4} + \mu_3(k_2, k_4) t_{k_1} s_{-k_2} s_{-k_3} s_{-k_4}.$$

Here s_k and t_k are defined in Eq. (2.24), while $\mu_1(k_1, k_2, k_3, k_4)$, $\mu_2(k_1, k_3)$, and $\mu_3(k_2, k_4)$ are defined in Eq. (2.19).

APPENDIX B

Symmetry Factors Associated with Self Energy Diagrams due to $H^{(3)}$

We provide some additional discussion relating to the second-order proper self-energy diagrams in Figs. 3.9 to 3.11, specifically with regards to the permutations of vertex labels and their symmetry factors. To illustrate what is involved, we consider the diagrams in Fig. 3.10 as an example. The first step is to figure out how many ways one can connect the lines representing creation and annihilation operators in order to obtain these proper self energy diagrams. The alternative colour schemes in Fig. B.1 illustrate the different possible ways of connecting the arrowed lines in order to obtain the proper self energy diagrams of Fig. 3.10.

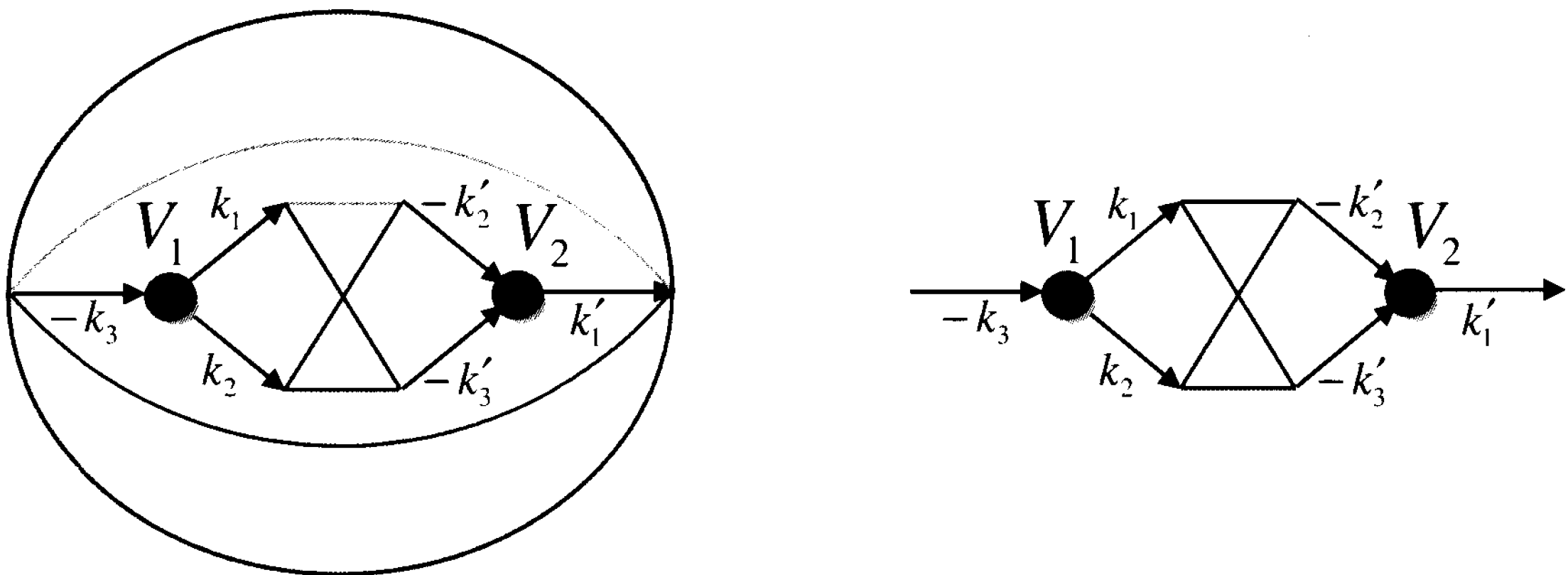


Fig. B.1: Some ways of connecting vertices to obtain the same proper self energy diagrams. Each colour (red, green, purple, orange) corresponds to a different possible permutation.

We see that there are four ways of obtaining the first diagram in Fig. 3.10 and two ways of obtaining the second. If we compare the correspondence between the wavenumber labels in Figs. B.1 and 3.10, we can write the interaction potential for all possible permutations in a factorized form to give a product like

$$[V_1(q, q', -q - q') + V_1(q', q, -q - q')] [V_2(q + q', -q, -q') + V_2(q + q', -q', -q)]$$

for the first diagram, and

$$[V_1(q', q - q', -q) + V_1(q - q', q', -q)] V_2(q, q - q', q')$$

for the second. Although this method seems somewhat cumbersome, it can be implemented straightforwardly by interchanging the wavenumber labels associated with arrows pointing in the same direction with respect to the vertex in the proper self energy diagrammatic representation, and then multiplying by the sum all possible permutations of the interaction potential for the two vertices. One must be careful when applying this method since for some cases there is symmetry between the Green's function lines in terms of the interchange of labels. For example, the labels q' and $q - q'$ for the second diagram in Fig. 3.10 can be arbitrarily interchanged, so if both are considered a factor of 1/2 must be introduced to avoid double counting.

REFERENCES

- [1] N. W. Ashcroft and N. D. Mermin, *Solid State Physics* (Saunders, Fort Worth, 1976).
- [2] C. Kittel, *Introduction to Solid State Physics* (Wiley, New York, 1995).
- [3] R. Skomski and J. M. Coey, *Permanent Magnetism* (Institute of Physics, Bristol, 1999).
- [4] D. C. Mattis, *The Theory of Magnetism I* (Springer, Berlin, 1981).
- [5] R. M. White, *Quantum Theory of Magnetism* (McGraw-Hill, New York, 1970).
- [6] D. J. Griffiths, *Introduction to Electrodynamics* (Prentice Hall, Upper Saddle River, 1999).
- [7] M. A. Heald and J. B. Marion, *Classical Electromagnetic Radiation* (Nelson Thomson, South Melbourne, 1995).
- [8] L. E. Reichl, *A Modern Course in Statistical Physics* (University of Texas Press, Austin, 1980).
- [9] K. Yosida, *Theory of Magnetism* (Springer, Berlin, 1996).
- [10] M. G. Cottam and D. R. Tilley, *Introduction to Surface and Superlattice Excitations* (Institute of Physics, Bristol, 2005).
- [11] H. Goldstein, C. Poole, and J. Safko, *Classical Mechanics* (Pearson, Singapore, 2002).
- [12] R. L. Liboff, *Introductory Quantum Mechanics* (Pearson Education, Singapore, 2003).
- [13] E. N. Economou, *Green's Functions in Quantum Physics* (Springer, Berlin, 2006).
- [14] T. Wolfram and R. E. DeWames, *Prog. Surf. Sci.* 2, 233 (1972).
- [15] M. G. Cottam and A. N. Slavin, *Linear and Nonlinear Spin Waves in Magnetic Films and Superlattices*, ed. by M. G. Cottam, (World Scientific, Singapore, 1994).
- [16] F. J. Dyson, *Phys. Rev.* 102, 1217 (1957)
- [17] F. Keffer, *Encyclopedia of Physics Vol. XVIII/2 Ferromagnetism*, ed. by S. Flügge, (Springer, Berlin, 1966).

- [18] A. N. Slavin, B. A. Kalinikos and N. G. Kovshikov, *Linear and Nonlinear Spin Waves in Magnetic Films and Superlattices*, ed. by M. G. Cottam, (World Scientific, Singapore, 1994).
- [19] R. N. Costa Filho, M. G. Cottam, and G. A. Farias, *Phys. Rev. B* 62, 6545 (2000).
- [20] H. Hopster, R. Raue, and R. Clauberg, *Phys. Rev. Lett.* 91, 147201 (2003).
- [21] Z. K. Wang, M. H. Kuok, S. C. Ng, D. J. Lockwood, M. G. Cottam, K. Nielsch, R. B. Wehrspohn, and U. Gösele, *Phys. Rev. Lett.* 89, 027201 (2002).
- [22] G. Gubbiotti, S. Tacchi, G. Carlotti, P. Vavassori, N. Singh, S. Goolaup, A. O. Adeyeye, A. Stashkevich, and M. Kostylev, *Phys. Rev. B* 72, 224413 (2005).
- [23] C. T. Boone, J. A. Katine, J. R. Childress, V. Tiberkevich, A. Slavin, J. Zhu, X. Cheng, and I. N. Krivorotov, *Phys. Rev. Lett.* 103, 167601 (2009).
- [24] C. Bayer, J. P. Park, H. Wang, M. Yan, C. E. Campbell, and P. A. Crowell, *Phys. Rev. B* 69, 134401 (2004).
- [25] B. Heinrich and J. A. C. Bland, *Ultrathin Magnetic Structures IV* (Springer, Berlin, 2005).
- [26] B. Hillebrands and K. Ounadjela, *Spin Dynamics in Confined Magnetic Structures II* (Springer, Berlin, 2003).
- [27] R. Arias and D. L. Mills, *Phys. Rev. B* 63, 134439 (2001).
- [28] T. M. Nguyen and M. G. Cottam, *Phys. Rev. B* 71, 094406 (2005).
- [29] D. J. Griffiths, *Introduction to Quantum Mechanics* (Pearson, Upper Saddle River, 2005).
- [30] J. J. Sakurai, *Modern Quantum Mechanics* (Addison-Wesley, Massachusetts, 1994).
- [31] C. Kittel, *Quantum Theory of Solids* (Wiley, New York, 1963).
- [32] R.D. Mattuck, *A Guide to Feynman Diagrams in the Many-Body Problem* (McGraw-Hill, New York, 1967).
- [33] G. Rickayzen, *Green's Functions and Condensed Matter* (Academic Press, London, 1984).
- [34] A. A. Abrikosov, L. P. Gorkov, and I. E. Dzyaloshinski, *Methods of Quantum Field Theory in Statistical Physics* (Dover Publications, New York, 1963).

- [18] A. N. Slavin, B. A. Kalinikos and N. G. Kovshikov, *Linear and Nonlinear Spin Waves in Magnetic Films and Superlattices*, ed. by M. G. Cottam, (World Scientific, Singapore, 1994).
- [19] R. N. Costa Filho, M. G. Cottam, and G. A. Farias, *Phys. Rev. B* 62, 6545 (2000).
- [20] H. Hopster, R. Raue, and R. Clauberg, *Phys. Rev. Lett.* 91, 147201 (2003).
- [21] Z. K. Wang, M. H. Kuok, S. C. Ng, D. J. Lockwood, M. G. Cottam, K. Nielsch, R. B. Wehrspohn, and U. Gösele, *Phys. Rev. Lett.* 89, 027201 (2002).
- [22] G. Gubbiotti, S. Tacchi, G. Carlotti, P. Vavassori, N. Singh, S. Goolaup, A. O. Adeyeye, A. Stashkevich, and M. Kostylev, *Phys. Rev. B* 72, 224413 (2005).
- [23] C. T. Boone, J. A. Katine, J. R. Childress, V. Tiberkevich, A. Slavin, J. Zhu, X. Cheng, and I. N. Krivorotov, *Phys. Rev. Lett.* 103, 167601 (2009).
- [24] C. Bayer, J. P. Park, H. Wang, M. Yan, C. E. Campbell, and P. A. Crowell, *Phys. Rev. B* 69, 134401 (2004).
- [25] B. Heinrich and J. A. C. Bland, *Ultrathin Magnetic Structures IV* (Springer, Berlin, 2005).
- [26] B. Hillebrands and K. Ounadjela, *Spin Dynamics in Confined Magnetic Structures II* (Springer, Berlin, 2003).
- [27] R. Arias and D. L. Mills, *Phys. Rev. B* 63, 134439 (2001).
- [28] T. M. Nguyen and M. G. Cottam, *Phys. Rev. B* 71, 094406 (2005).
- [29] D. J. Griffiths, *Introduction to Quantum Mechanics* (Pearson, Upper Saddle River, 2005).
- [30] J. J. Sakurai, *Modern Quantum Mechanics* (Addison-Wesley, Massachusetts, 1994).
- [31] C. Kittel, *Quantum Theory of Solids* (Wiley, New York, 1963).
- [32] R.D. Mattuck, *A Guide to Feynman Diagrams in the Many-Body Problem* (McGraw-Hill, New York, 1967).
- [33] G. Rickayzen, *Green's Functions and Condensed Matter* (Academic Press, London, 1984).
- [34] A. A. Abrikosov, L. P. Gorkov, and I. E. Dzyaloshinski, *Methods of Quantum Field Theory in Statistical Physics* (Dover Publications, New York, 1963).

- [35] W. E. Parry and R. E. Turner, *Many-Body Problems*, ed. by S. F. Edwards, (Benjamin, New York, 1969).
- [36] A. L. Fetter and J. D. Walecka, *Quantum Theory of Many-Particle Systems* (McGraw-Hill, New York, 1971).
- [37] C. Kittel and H. Kroemer, *Thermal Physics* (Freeman, New York, 1980).
- [38] A. D. Wunsch, *Complex Variables With Applications* (Pearson Education, Boston, 2005).
- [39] B. A. Kalinikos, *Linear and Nonlinear Spin Waves in Magnetic Films and Superlattices*, ed. by M. G. Cottam, (World Scientific, Singapore, 1994).
- [40] M. L. Plumer, J. Van Ek, and D. Weller, *The Physics of Ultra-High-Density Magnetic Recording* (Springer, Berlin, 2001).
- [41] M. Nouri and M. G. Cottam, *J. Appl. Phys.* 97, 10J112 (2005).

CURRICULUM VITAE

Name: Arash Akbari-Sharbat

Education and Degrees: York University
Toronto, Ontario, Canada
2002 – 2008 B.Sc. in Physics

Honors and Awards: Dean's Honour Roll
York University
Toronto, Ontario, Canada, 2006 – 2007

The W. J. Megaw Prize in Experimental Physics
York University
Toronto, Ontario, Canada, 2006 – 2007

Graduate Tuition Scholarship
The University of Western Ontario
London, Ontario, Canada, 2008 – 2010

Related Work Experience: Teaching Assistant
The University of Western Ontario
London, Ontario, Canada, 2008 – 2010